USING A REGIONAL CHEMICAL TRANSPORT MODEL FOR THE ANALYSIS OF GASESOUS AND PARTICULATE AIR POLLUTANTS IN THE MEXICO CITY METROPOLITAN AREA

A Thesis

by

SAJJAD GHULAM ALI

Submitted to the Office of Graduate Studies of
Texas A&M University
in partial fulfillment of the requirements for the degree of

MASTER OF SCIENCE

December 2010

Major Subject: Civil Engineering

Using a Regional Chemical Transport Model for the Analysis of Gaseous and Particulate Air Pollutants in the Mexico City Metropolitan Area

USING A REGIONAL CHEMICAL TRANSPORT MODEL FOR THE ANALYSIS OF GASESOUS AND PARTICULATE AIR POLLUTANTS IN THE MEXICO CITY METROPOLITAN AREA

A Thesis

by

SAJJAD GHULAM ALI

Submitted to the Office of Graduate Studies of
Texas A&M University
in partial fulfillment of the requirements for the degree of

MASTER OF SCIENCE

Approved by:

Chair of Committee,	Qi Ying
Committee Members,	Emily M. Zechman
	Sarah D. Brooks
Head of Department,	John M. Niedzwecki

December 2010

Major Subject: Civil Engineering

ABSTRACT

Using a Regional Chemical Transport Model for the Analysis of Gaseous and Particulate Air Pollutants in the Mexico City Metropolitan Area. (December 2010)

Sajjad Ghulam Ali, B.S., Texas A&M University

Chair of Advisory Committee: Dr. Qi Ying

Air quality in the Mexico City Metropolitan Area (MCMA) is the subject of many studies due to concerns from high emissions and their adverse effects on public health and the environment. In this study, a high resolution simulation is performed with the Community Multi-scale Air Quality modeling system (CMAQ) using meteorology generated by the Weather Research Forecasting system (WRF). The boundary conditions for CMAQ are provided by the Goddard Earth Observing System-CHEMistry model (GEOS-Chem). The simulation period was March 2-7, 2006. Hourly species concentrations of O_3, NO_x, CO, SO_2, PM_{10}, and $PM_{2.5}$ for the period were provided by the Automatic Air Quality Monitoring Network (labeled as RAMA). Preliminary evaluation showed GEOS-Chem and CMAQ being in good agreement with their predicted concentrations. In comparison with the base case boundary conditions, the GEOS-Chem case performs better and predicts closer to the observed values of O_3, NO_x, PM_{10}, $PM_{2.5}$, and SO_2. Particle trajectory analysis was performed using the HYbrid Single-Particle Lagrangian Integrated Trajectory model (HYSPLIT) to ascertain the major sources of SO_2 emitters and their impact on the MCMA.

DEDICATION

For my late grandmother and aunt

ACKNOWLEDGEMENTS

I would like to thank my advisor, Dr. Qi Ying, for giving me the opportunity to work with him. This has been a highly rewarding experience and I have learned a lot under his supervision. I have been very fortunate for being given the chance to learn many valuable skills.

I am also grateful to have Dr. Sarah D. Brooks and Dr. Emily M. Zechman on my committee. They have been extremely patient and accommodating to my requests and have provided me with valuable feedback and support throughout the course of this research.

I would like to thank all of my friends, research group colleagues, classmates, as well as the department faculty and staff who I have come to know and appreciate during my time here as an undergraduate and a graduate student. They have been very supportive of my decisions and have always been there for me whenever I needed help.

Finally, I would like to acknowledge the immense love and hope given to me by my mother, my father, my brother, and the rest of my family. No amount of gratitude can account for their unwavering dedication and guidance towards my endeavor. Were it not for their enthusiasm and support, I would not have made it this far.

NOMENCLATURE

AMS	Aerosol Mass Spectrometer
ARL	NOAA Air Resource Laboratory
BC	Black (or Elemental) Carbon
BCON	Boundary Condition
BPCH	Binary PunCH Format
CAMx	Comprehensive Air Quality Model
CMAQ	Community Multi-Scale Air Quality Modeling System
CMB	Chemical Mass Balance Method
CTM	Chemical Transport Model
EC	Elemental (or Black) Carbon
EPA	Environmental Protection Agency
FORTRAN	Formula Translator
GEOS-Chem	Goddard Earth Observing System-CHEMistry
GMAO	NASA Global Modeling Assimilation Office
HYSPLIT	HYbrid Single-Particle Lagrangian Integrated Trajectory
ICON	Initial Condition
IOAPI	Input/Output Applications Programming Interface
J-PROC	J-Values (Photolysis Rate) PROCessor
MCIP	Meteorology-Chemistry Interface Processor
MCMA	Mexico City Metropolitan Area

MILAGRO	Megacity Initiative: Local and Global Research Observations
MM5	5th Generation Mesoscale Modeling System
NASA	National Aeronautics and Space Administration
NCAR	National Center for Atmospheric Research
NEI	National Emission Inventory
netCDF	network Common Data Form
NOAA	National Oceanic and Atmospheric Administration
NO_x	Oxides of Nitrogen
OA	Organic Aerosol
OC	Organic Carbon
OOA	Oxygenated Organic Aerosol
O_x	Odd Oxygen
PM	Particulate Matter
POA	Primary Organic Aerosol
RAMA	Automatic Air Quality Monitoring Network
RAMS	Regional Atmospheric Monitoring System
SAPRC-99	Statewide Air Pollution Research Center Mechanism, 1999
SMOKE	Sparse Matrix Operator Kernel Emissions
SOA	Secondary Organic Aerosol
VOC	Volatile Organic Compound
WRF	Weather Research Forecasting System

TABLE OF CONTENTS

Page

LIST OF FIGURES

FIGURE Page

FIGURE Page

FIGURE Page

LIST OF TABLES

1. INTRODUCTION

1.1 Air Quality in the Mexico City Metropolitan Area

Degradation of air quality in the urban areas of the world can directly harm the health of a large population, adversely affect the built and natural environment of the surrounding regions, and contribute to global climate change. In this aspect, the rapid growth of megacities (urban areas with a population of over 10 million) in the developing world being a major source of atmospheric pollution is a cause for concern. Mexico City is akin to other urban areas around the world in the types of environmental challenges they all experience.

The Mexico City Metropolitan Area (MCMA) shown in Figure 1, latitude 19°N and longitude 99°W, is situated on an elevated basin 2240 m above mean sea level. The basin covers an area of about 7700 km^2 that is constrained by mountain ridges on three sides (east, south, and west). This topography sets unique meteorological conditions in the MCMA. The surrounding mountains during thermal inversion periods tend to trap pollutants within the MCMA basin. The high altitude and temperate climate lead to intense sunlight that aids the photochemical processes of ozone and other oxidants. In this geographical setting, MCMA has a population of around 20 million, around 4 million vehicles, and over 40,000 industries that contribute to atmospheric pollution (Molina and Molina, 2002; 2004).

This thesis follows the style of Atmospheric Environment.

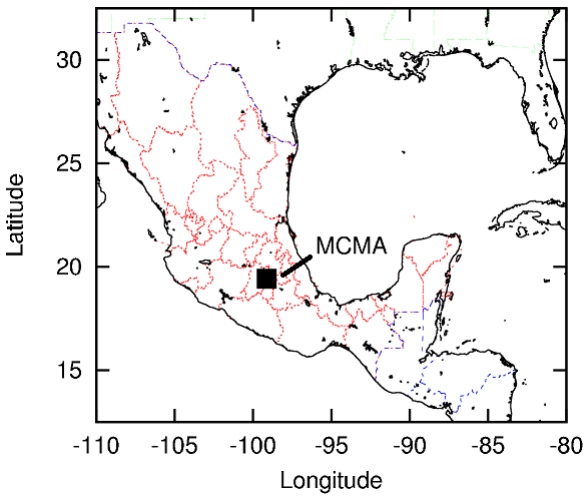

Figure 1 Location of the Mexico City Metropolitan Area.

1.2 Measurements

The RAMA system (also known as the Automatic Air Quality Monitoring Network) has been providing long-term data for carbon monoxide (CO), ozone (O_3), sulfur dioxide (SO_2), nitrogen oxides (NO_x = NO + NO_2), total suspended particles (TSP), and particulate matter with diameter of 10 μm or less (PM_{10}) since 1986. Intensive field campaigns have also provided with additional measurements. The 1991-1994 MARI project and the 1997 IMADA-AVER campaign collected meteorological data and data regarding particulate matter (PM) and volatile organic compounds (VOC) composition (Doran et al., 1998; Edgerton et al., 1999; Molina and Molina, 2002). In addition, the MCMA-2003 and MILAGRO-2006 field campaigns have provided a much deeper understanding of processes within and around MCMA regarding O_3 formation and its sensitivity to VOC and NO_x, PM composition and size distribution, secondary organic aerosol (SOA) mechanisms, effects of meteorology, and source contribution to

pollutants (Molina et al., 2007; 2010). A selection of work conducted with these campaigns has been provided in the literature review that follows.

1.3 Literature Review

Studies on major sources of emissions are necessary to identify prominent polluting entities and to improve the existing emission inventories for future studies. Jaimes and Sandoval (2002) examined VOC emission sources to determine which contribute high concentrations of propane and butane in MCMA. The study had two conclusions: butane was found to be higher in vehicle exhaust and evaporation, and liquefied petroleum gas (LPG) handling may be responsible for most propane contribution. In another VOC study, Sosa et al. (2009) presented a source apportionment study of VOC at three locations in southwestern area of MCMA. The major sources of contribution at the residential and university stations were from working with LPG and vehicular exhaust. Those at the gas refueling station were from vehicle exhaust and evaporation during filling of LPG in tanks.

In considering the sources of suspended particles such as PM, Bravo et al. (2002) looked at wildfires in MCMA during 1992-1999 to assess their impact on air quality. PM was found to be a significant pollutant from this source given that it can transport beyond Mexico towards the north. Additionally, a strong correlation between particulate wildfire emissions and particulate air quality was found in this study. In a study done by Villlasenor et al. (2003), a wind erosion model was utilized to estimate wind-blown dust concentrations in the MCMA during the IMADA-AVER campaign. The study showed how dust from agricultural areas and sparsely vegetated soils are transported by strong

winds to the MCMA. While predicted concentrations based on the wind erosion model showed good correlation with observed PM_{10} concentrations during the observed period, the study concluded that a more advanced algorithm may be more helpful in discerning the sources of origin for wind-blown dust.

de Foy et al. (2007) analyzed the emission inventory for CO and SO_2 to better account for emission sources of these pollutants. The study identified mobile sources for CO across MCMA and two large point sources of emission for SO_2 on the outskirts of MCMA (the Tula industrial complex in the northwest and the Popocatépetl volcano in the southeast). With regards to SO_2, the industrial complex contributed about 20% of the total emissions while the volcano provided with about 5%. The remaining emissions were found to be within the MCMA.

Stone et al. (2010) determined the important sources of organic aerosol during the MILAGRO campaign. Samples were collected from two sites in the MCMA and analyzed. Source apportionment showed that diesel and gasoline motor vehicles were the major source contributors to primary organic carbon (OC) while contribution from biomass burning was significant but varied for each day. The major source contributor for secondary OC at both sites was also anthropogenic.

Lei et al. (2008) analyzed O_3 formation in the MCMA in relation to changes in precursors and other emissions for three distinct meteorological episodes during the MCMA-2003 campaign. O_3 was found to be less dependent on the meteorological conditions and rather more dependent on emission of the precursor pollutants such as NO_x and VOC. Fresh O_3 plume was more VOC-sensitive in comparison with a more

chemically aged plume that was NO_x-sensitive. A similar study done by Song et al. (2010) checked O_3 sensitivity to emission changes during the MILAGRO campaign for three additional meteorological settings. The study concluded that O_3 was entirely VOC-limited in the urban area. These studies indicated to how O_3 production was primarily affected by the presence of VOC and NO_x under the given meteorological conditions.

The study of air flow and wind circulations in the MCMA has been important for understanding the regional movement of the urban plume. Bossert (1997) investigated air flow regimes during a 3-day period in the MARI campaign to understand how regional and synoptic-scale winds interact with plumes in the MCMA. The study found that external winds and terrain-driven circulations were able to shift pollution plumes in MCMA. While the model predictions correlated with the observations, the study concluded that the relationship between air flow patterns pollution concentrations may be more complex.

Fast and Zhong (1998) modeled circulations from the IMADA-AVER campaign data in a mesoscale model RAMS (Regional Atmospheric Monitoring System) to analyze the meteorological parameters affecting inhomogeneous O_3 concentrations in MCMA. Based on the parameters utilized, the study showed that circulations are very complex and may be additionally dependent on factors such as temperature, humidity, advection, diffusion, and wind shears.

Jazcilevich et al. (2003) simulated air pollution scenarios over Central Mexico that showed circular air flow patterns across the vertical plane. Near surface pollutants in one area of the MCMA could be carried to another by the vertical circulation of air.

These air flow patterns and the transport of pollutants across MCMA can have implications for other regions near the MCMA.

Zhang et al. (2009) conducted a study in which the ground-based RAMA measurements were compared with WRF-Chem model predictions of O_3, VOC, and NO_x during the MILAGRO campaign and checked O_3 sensitivity to its precursors. As a part of the sensitivity analysis, the base case results were compared with simulations where VOC and NO_x emissions were reduced by 25% and 50%. The study concluded that VOC reduction was the most effective way to control O_3 production while NO_x reduction only increased O_3 in the MCMA. A 50% reduction in VOC cut peak O_3 concentration by 28% whereas a similar reduction in NO_x led to a 20% increase in O_3.

The differences in weekday and weekend emissions in the MCMA have been investigated by Stephens et al. (2008). The study discerned weekly patterns of emissions in MCMA during 1986-2007 to compare weekday and weekend surface concentrations. The RAMA system data was used to analyze weekday and weekend emissions. While CO, NO_x, and PM_{10} concentrations were found to be lower for weekends, O_3 remained unaffected during weekends. In some instances, weekend concentration for O_3 was even higher than those for weekdays, which was thought to be directly related with decreased NO_x emissions.

The mechanisms of SOA processes in the MCMA are intricate and not adequately represented in the simulation models owing to the various ways in which SOA formation may occur. Dzepina et al. (2009) have evaluated the performance of such models that have been updated with SOA mechanisms. Three SOA models are used

for a case study in MCMA to properly account for SOA formation: (1) a revised traditional 2-product model with improvements in the yields of aromatics, (2) traditional model with additional SOA formation from glyoxal, and (3) model with additional SOA formation from primary semi-volatile and intermediate volatility species (P-S/IVOC). The first model was unable to produce enough SOA to match the observation by approximately a factor of 7. The second model could not account fairly for the missing SOA but improved the timing of SOA formation, O/C ratio, and reduced the gap between observations and predictions. The third model introduced significant concentrations of carbon that was missing from the other models. With varied results, the evaluation gave a somewhat better understanding of SOA contribution and the need to improve current mechanisms further.

Various studies for PM have also been conducted to learn of its sources of origin as well as its overall composition. Edgerton et al. (1999) looked at composition of particulate matter during the IMADA-AVER campaign. Almost half of PM_{10} came from fugitive dust. Particulate matter with diameter of 2.5 μm or less ($PM_{2.5}$) made up for 50% of PM_{10} in fraction which has been shown in later studies as well (Chow et al., 2002; Vega et al., 2002). Organic carbon (OC) and elemental carbon (EC) composed of about half of $PM_{2.5}$. The highest concentrations were found during morning and after sunset that was attributed to rush-hour traffic. Chow et al. (2002) examined chemical characteristics of particulate matter during the IMADA-AVER campaign. For PM_{10}, geological material contributed the most to total mass (48%) followed by OC (23%), EC (8%), sulfate (12%), nitrate (8%), non-crustal elements (2%), and salt (1%). For PM2.5,

the most contribution to total mass was made by OC (31%), followed by EC (14%), sulfate (19%), nitrate (10%), geological material (14%), non-crustal elements (2%), and salt (less than 1%).

Mugica et al. (2009) looked at PM measurements during the MILAGRO campaign for their composition and source contribution. Carbon made up for 52% of $PM_{2.5}$ mass and 30% of PM_{10} mass. Vehicular exhaust, followed by soil, is found to be a major source contributor to $PM_{2.5}$. Weekend concentrations were lower owing to reduced industrial and vehicular emissions. Additionally, a comparison of six meteorological episodes during the campaign showed that meteorological conditions and the climate have an influence on PM size and sources.

The regional impacts of emissions from MCMA have been studied in the past for its effects on regional air quality and atmospheric processes. Mena-Carrasco et al. (2009) conducted a study to investigate the effects of MCMA emissions on regional air quality, photochemistry, and O_3 production during the MILAGRO campaign. Surface level NO_x, CO, O_3 are relatively localized, confined to a radius of less than 200 km. Footprints of actual emissions are more significant at higher elevations. A large amount of reactive nitrogen species can be transported northeast to as far as the Gulf of Mexico and impact regional O_3 formation. The study noted that aerosol concentrations can affect regional O_3 production by hampering photochemical processes.

1.4 Objectives

Various models have been used in the past to help understand the formation of air pollutants in the MCMA, such as the offline CAMx/MM5 (Lei et al., 2008) and

WRF-Chem (Zhang et al., 2009). Horizontal grid resolution of as high as 3 km has been used in these studies. Although those modeling domains typically cover MCMA and surrounding regions, most of the studies do not include anthropogenic emissions of gaseous and PM pollutants from outside sources, the PM emissions due to windblown dust and SO_2 emissions from Popocatépetl, an active volcano 70 km southeast of Mexico City. Several individual studies indicate that these sources could contribute significantly to the observed concentrations in the MCMA. Additionally, the MCMA anthropogenic emissions used in these studies are outdated and could not represent the actual emissions for a recent air quality episode such as the 2006 MILAGRO campaign.

The purpose of this project is to perform three dimensional simulations of major air pollutants in the MCMA with the most recent and complete emission inventory with a fine horizontal spatial resolution of 1 km, three times higher than previous simulations. Figure 2 highlights role of major models used in the simulation and the flow of data between them. The Community Multi-scale Air Quality (CMAQ) Model, which is developed by the Environmental Protection Agency (EPA) as a regulatory/research air quality model, will be used in this study. This study will further enhance our current understanding of the formation of air pollutants in MCMA. It is also the first time the CMAQ model is being applied in the MCMA. The exercise provides further evaluation of the capability of the CMAQ at a very different elevation and emission conditions than these typically meet in the United States.

This project seeks to achieve this goal through the following objectives:

1. Validation of the capability of the global chemistry model GEOS-Chem in generating proper boundary conditions (BCON).

2. Application of the CMAQ regional chemical transport model (CTM) with GEOS-Chem derived BCON to simulate air pollutants in the MCMA during the period of March 2-7, 2006.

3. Evaluation of the model performance of O_3, CO, NO_x, VOC, $PM_{2.5}$ and PM_{10} through time series analysis and statistical model performance analysis.

4. Analysis of the source regions of SO_2 and determine the contributions of different source regions to SO_2 in MCMA.

5. Evaluation of the sensitivity of predictions to select model parameters (BCON, minimal vertical diffusivity, grid resolution and NO_x and VOC emissions).

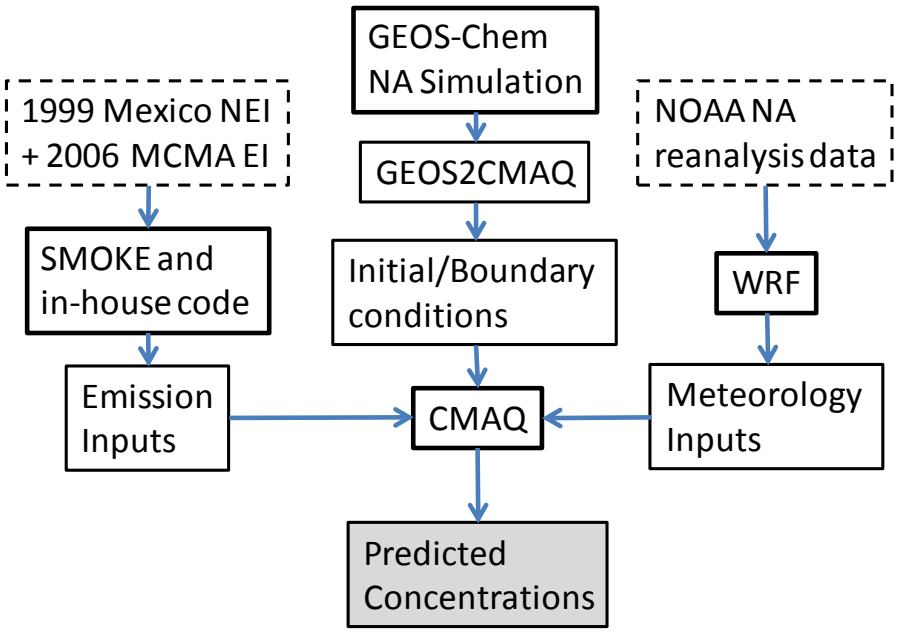

Figure 2 Schematic of the air quality modeling system.

In Section 2, the GEOS-Chem model and the global and nested simulation results are described. The generated boundary condition results are compared with the default boundary conditions (provided by the CMAQ package). Predicted pollutant concentrations in the MCMA are also compared with CMAQ simulations. In Section 3, the CMAQ model is described in greater detail and the CMAQ simulation results using the default boundary condition profiles and the GEOS-Chem generated BCON are extensively compared. The CMAQ predictions are also compared with available observation data for O_3, NO_x, CO, SO_2, $PM_{2.5}$ and PM_{10}.

2. GLOBAL CHEMISTRY MODELING WITH GEOS-CHEM

The first step involves the establishment and evaluation of the global model GEOS-Chem before it can be used to generate BCON for the regional model CMAQ. This section describes the GEOS-Chem model and its specific application to the project. Results have been processed and analyzed to provide an evaluation of the model concluding with the how GEOS-Chem output was used to extract BCON for CMAQ.

2.1 Model Description

GEOS-Chem is a global three dimensional model of atmospheric chemistry that uses assimilated meteorology from the Goddard Earth Observing System (GEOS) of the NASA Global Modeling Assimilation Office (GMAO) (Bey et al., 2001). GEOS-Chem was developed by the Atmospheric Chemistry Modeling Group at Harvard University for the simulations of global atmospheric compositions based on spatially and temporally allocated emissions of anthropogenic and biogenic sources. The emissions from the United States are based on the National Emission Inventory (NEI) prepared by the EPA. Emissions from other parts of the world are collected from various international agencies documented in the GEOS-Chem User's Guide. GEOS-Chem can be applied to evaluate the effects of atmospheric disasters such as volcanic eruptions, wildfires, and dust storms. Additionally, the intercontinental transport of pollutants, biomass burning events, and other air quality phenomenon can also be modeled.

GEOS-Chem can operate with various meteorological data such as GEOS-3 (for the years 1998, 2000-2002), GEOS-4 (1985-2006), and GEOS-5 (2003-present) with a

global horizontal resolution of either 4°x5°, 2°x2.5°, 1° x 1.25°, or 1° x 1° with 30-72 vertical layers. To perform extensive simulations, GEOS-Chem uses TPCORE transport and FAST-J photolysis routines as well as the SMVGEAR II chemistry solver package. GEOS-Chem can also be run across multiple processors on a single machine using OpenMP compiler options. Along with performing global simulations, the model can also run high resolution nested grid simulations for Asia, North America, and Europe.

2.2 Model Application

GEOS-Chem v-8-02-01 was used run simulations for March 2006 using the most recent GEOS-5 meteorological fields. A global simulation was performed with a horizontal resolution of 4°x5° (approximately 445 km by 557 km) with 47 hybrid sigma vertical levels. The NO_x-O_x-VOC simulation contains 43 tracers and 230 reactions. The global resolution scheme was run for 12 months prior to the episode period for proper initialization. In turn, the results from the global simulation were used to run the nested grid simulation of North America (NA). Once again, the nested resolution was also run for one month prior to the episode period for proper initialization.

The NA nested domain has a horizontal resolution of 0.5°x0.667° (approximately 56 km by 74 km) with 40 hybrid sigma levels (up to 25 km). The domain size of 151x121 (lower-left corner of 140°W, 10°N and upper-right corner of 40°W, 70°N) can adequately accommodate the MCMA and the greater Mexico region without difficulty.

Figure 3 shows a plot of the hourly concentration of odd oxygen ($O_x = O_3 + NO_2 + 2NO_3$) in a portion of the regional GEOS-Chem domain. The CMAQ modeling

domain would be located within a region defined by grid cell (60, 17) (lower left) and (63, 22) (upper right) in the GEOS-Chem domain. The MCMA is situated at (61, 19).

2.3 Evaluation of Results

GEOS-Chem writes all output using the sequential binary punch format. Each binary punch file contains a general header followed by the subsequent data blocks where each block consists of a header and the actual data array. Data extraction programs were written in FORTRAN and executed in a Linux cluster along with all the visualization routines used to produce plots for GEOS-Chem species.

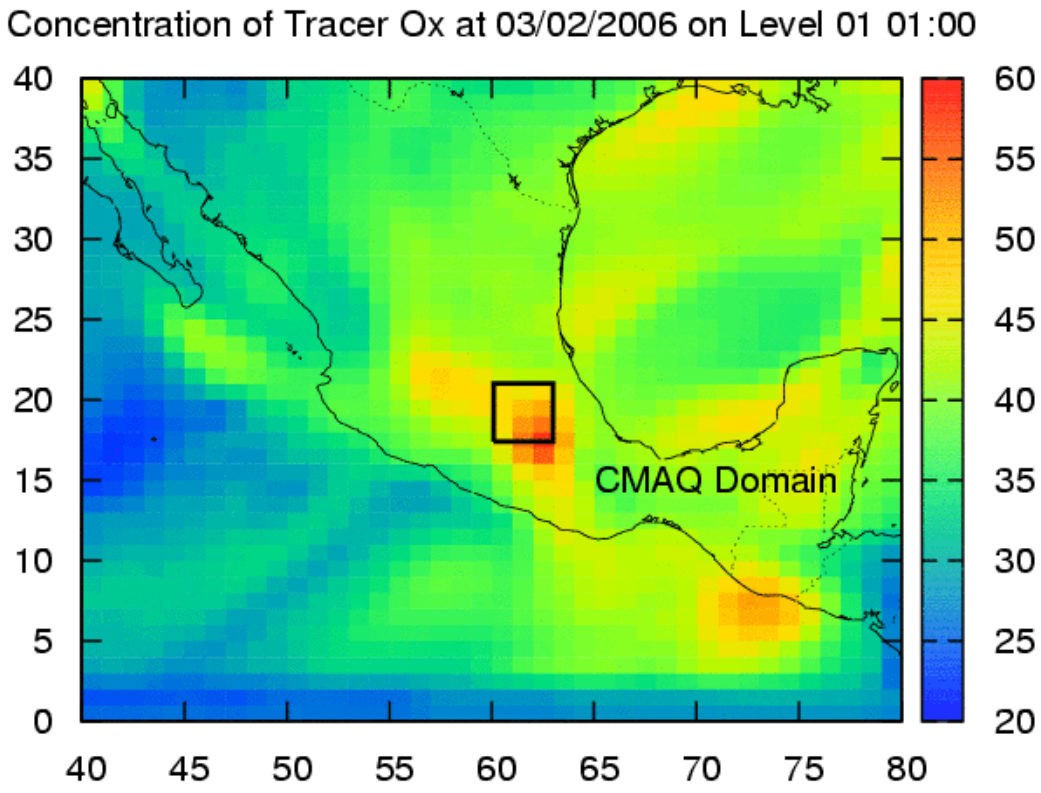

Figure 3 Hourly spatial concentration of O_x at the surface in the GEOS-Chem regional simulation. Box on the plot shows the location of the CMAQ domain. Units are in ppbV.

2.3.1 Hourly Averages of GEOS-Chem Species

Multiple sets of individual plots showing hourly concentrations have been generated for selected GEOS-Chem species. Given the sheer number of plots that became available for the entire modeling episode, hourly plots for the respective species have been lumped as daily concentration sets for a side-by-side comparison for each hour. This comparison is useful in understanding the behavior of the plume and how it may transport to different regions.

Figure 4 shows the hourly spatial concentrations of the GEOS-Chem species O_x for March 3, 2006. The plots represent the starting hour range of 00:00 to 23:00 Greenwich Mean Time (GMT). The concentration in the MCMA and the CMAQ model domain for March 3, 2006 is in the range of 30 to 55 ppb.

According to de Foy et al. (2008), the March 1-7, 2006 period in the MCMA received northwesterly winds with south bound transport at the surface. This period of the meteorological episode, dubbed as a "South-Venting" time, resulted in the transport of the urban plume southwards through the gap in the south east. This pattern of high concentration across the southern boundary of the CMAQ model domain indicates that GEOS-Chem can reasonably predict transport for the given meteorological conditions.

Daily sets of hourly concentration plots have also been generated for NO_x, CO, SO_2, BCPI, BCPO, OCPI, and OCPO but are not be presented in this section. Complete plots for the entire modeling episode are available as a separate attachment.

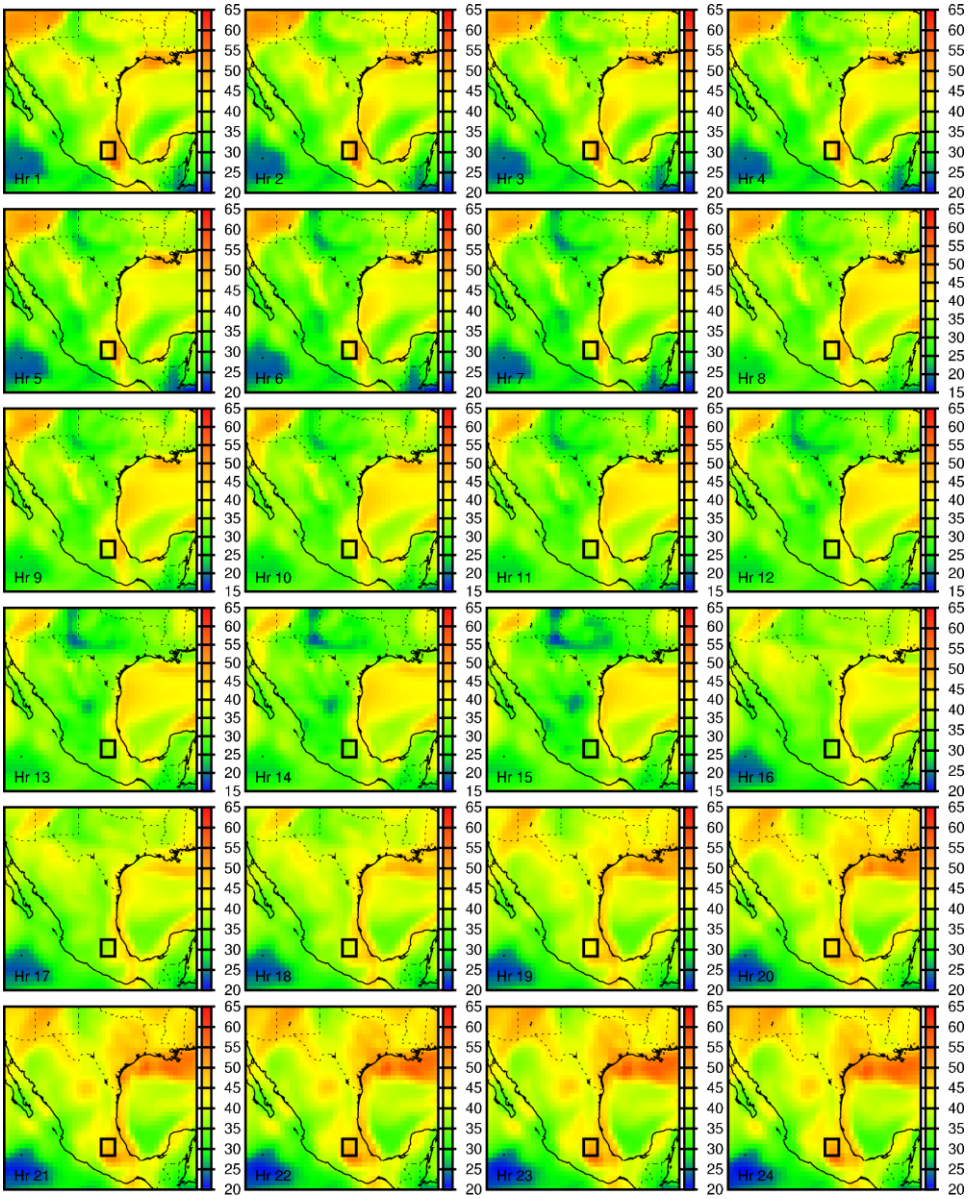

Figure 4 Hourly spatial concentration of O_x in the GEOS-Chem regional simulation for March 3, 2006. The box on the plot shows the location of the CMAQ domain. Units are in ppbV.

2.3.2 Episode Averages for the March 2-7, 2006 Period

All hourly concentrations for the entire modeling period have been averaged to provide the general species concentration for the episode. Figure 5 shows the episode averages of the GEOS-Chem species O_x, NO_x ($NO + NO_2 + NO_3 + HNO_2$ as defined by

GEOS-Chem), CO, and SO_2. GEOS-Chem shows above average concentrations for all species in the MCMA during the modeling episode. Additionally, higher concentrations are also shown in the areas around the CMAQ model domain as well as the greater Mexico region. NO_x is present in the concentration of 9 ppb around the MCMA, O_x at 35 ppb, CO above 160 ppb, and SO_2 over 13 ppb. This indicates the extent of the urban emissions to adjacent regions. Based on the meteorological episode during certain days, the MCMA plume is shown to have been transported to other regions. The NO_x concentration in the MCMA is similar to those at the Greater Houston Metropolitan Area in southeast Texas, while CO, SO_2, and O_x concentrations are even higher.

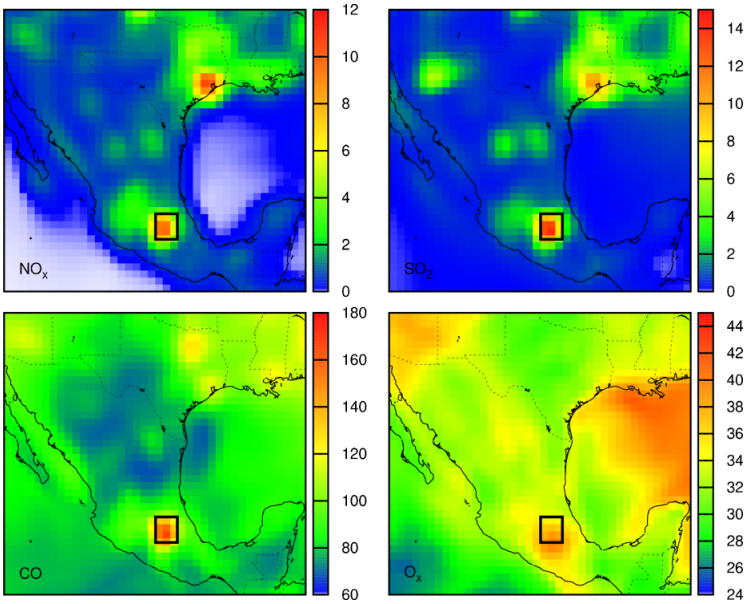

Figure 5 Episode average plot for O_x, NO_x, CO, and SO_2. The box indicates to location of the CMAQ model domain. All units are in ppbV.

Figure 6 shows the episode averages of the GEOS-Chem black carbon (BC) also known as elemental carbon, and primary organic carbon (OC) aerosol species. In the

GEOS-Chem model, BC and OC are separated into two groups. The hydrophobic group (BCPO and OCPO) represents recently emitted primary particles (80% of EC and 50% of OC are assumed to be hydrophobic) while the hydrophilic group (BCPI and OCPI) represents aged particles. The hydrophobic carbon aerosols are converted to hydrophilic aerosols with an e-folding time of 1.15 days (Cooke et al., 1999). GEOS-Chem shows slightly above average concentrations for EC in the MCMA during the modeling episode while OC concentrations are very high for the region. Elemental aerosols BCPI and BCPO are present in the MCMA at concentrations of around 1 and 2 μg/m^3 respectively. Organic aerosols OCPI and OCPO have concentrations of 2 and 1.2 μg/m^3 respectively. Compared to the surrounding areas, the grid cells representing the CMAQ model domain have high concentrations of the carbon aerosol that indicates to significant emission activities in the MCMA for the entire modeling episode.

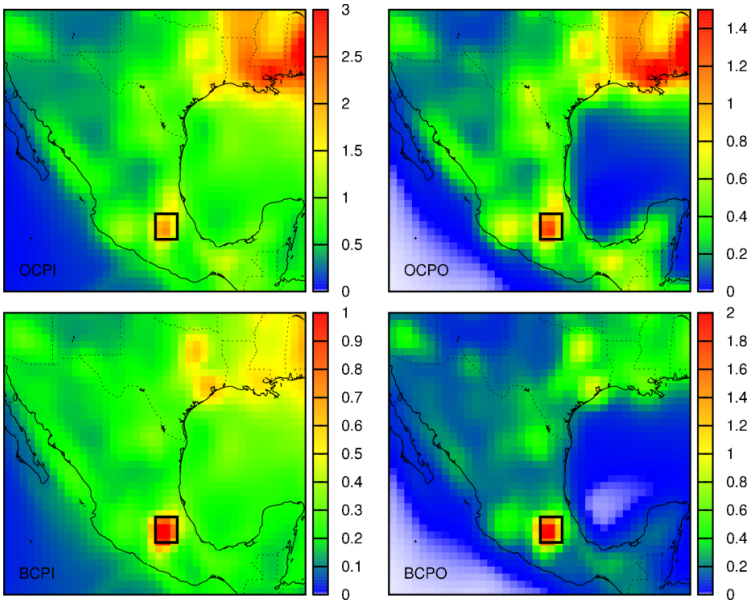

Figure 6 Episode average plot for OCPI, OCPO, BCPI, and BCPO. The box indicates to the location of the CMAQ model domain. All units are in μg/m^3.

Figure 7 shows the episode average plots for various fine PM species as well as total $PM_{2.5}$ predicted by the GEOS-Chem model in the surface layer. Sulfate, nitrate, and ammonium aerosol species (ASO4J, ANO3J, and ANH4J respectively using CMAQ species names) are present in high concentrations (approximately 6, 2.5, and 3 $\mu g/m^3$ respectively) in the MCMA. OC and EC aerosol species (AORGPAJ and AECJ respectively) in the CMAQ model domain is approximately 0.14 and 1.4 $\mu g/m^3$ respectively. Only dust aerosol (A25J) and the sea salt aerosol species (ANAJ and ACLJ) concentration levels are lower in the MCMA. With ANAJ and ACLJ, it is understandable that the location of the megacity is not close to the coastline.

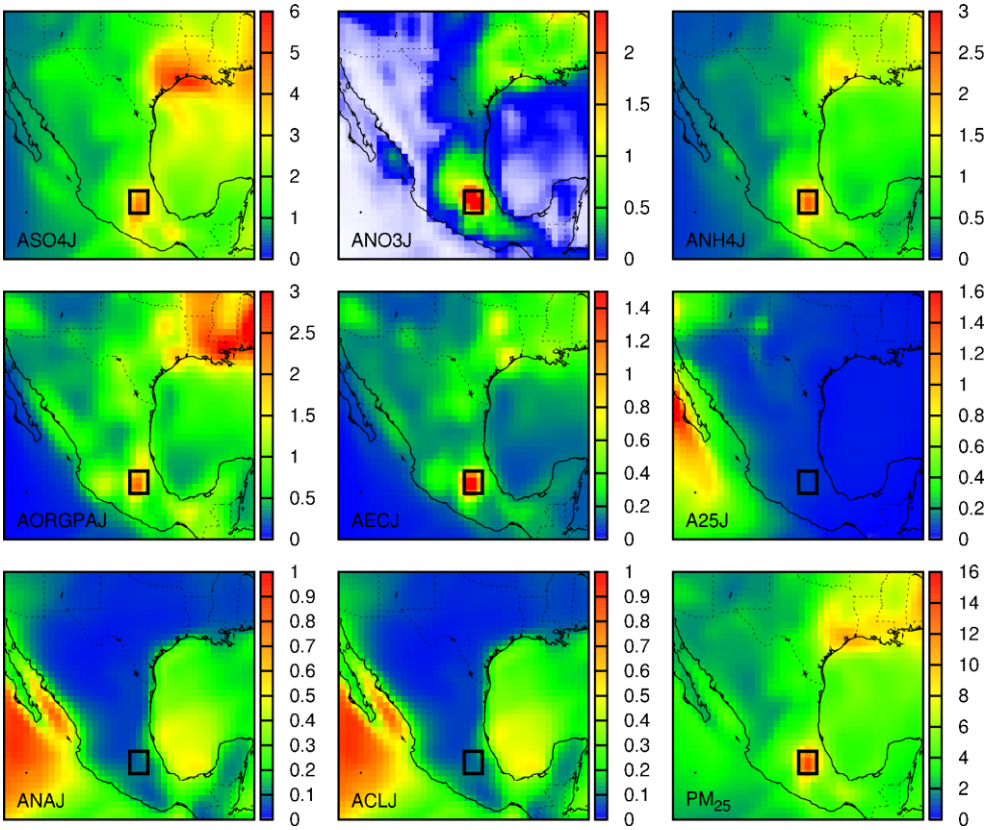

Figure 7 Episode average plot for fine PM species and total $PM_{2.5}$. The box indicates to the location of the CMAQ model domain. All units are in $\mu g/m^3$.

GEOS-Chem emission predicts low A25J concentrations over MCMA which is due to missing windblown dust from agricultural activities in the surrounding regions. The dust emissions in the GEOS-Chem is confined to desert, semi-desert or dust mobilizing areas (areas with significantly reduced vegetation cover) (Duncan Fairlie et al., 2007). The high A25J over the ocean is likely from dust emissions from the semi-desert areas in Southern California and Arizona in the United States and the Baja California peninsula in northwestern Mexico. The last plot is the sum of all fine PM species that makes up $PM_{2.5}$. The fine PM species plotted are presented in a manner so as to represent their counterparts in CMAQ. The list of GEOS-Chem species mapped to these fine PM species is available in Appendix B.

2.3.3 Comparison of GEOS-Chem and CMAQ Vertical Profiles

In addition to providing BCON for the surface layer, the GEOS-Chem model is capable of providing realistic BCON for the CMAQ model as a function of height. Realistic BCON are important in correctly predicting the inflow of pollutants in the CMAQ domain which could potentially affect predictions in MCMA.

For the purpose of this project, vertical profiles of selected species have been shown comparing GEOS-Chem results with the default CMAQ BCON profile across the boundaries of the CMAQ model domain. As such, four plots are shown for each set indicating the average vertical profile of the species along the northern, eastern, southern, and western edge of the CMAQ model domain.

Figure 8 compares the vertical profiles of O_x, NO_x, CO, and SO_2 for GEOS-Chem and CMAQ. The CMAQ default profiles are not direction dependent. Overall,

CMAQ default profiles reasonably agree with GEOS-Chem profiles. The NO_x profiles agree the best, while the differences in CO and SO_2 profiles are also small. The largest difference in these profiles occurs in the south direction where the GEOS-Chem profiles show higher concentrations. The CO profiles also show significant differences over 5000 m. The CMAQ O_x profiles have significantly lower concentrations in higher altitudes than the O_x concentrations predicted by the GEOS-Chem model.

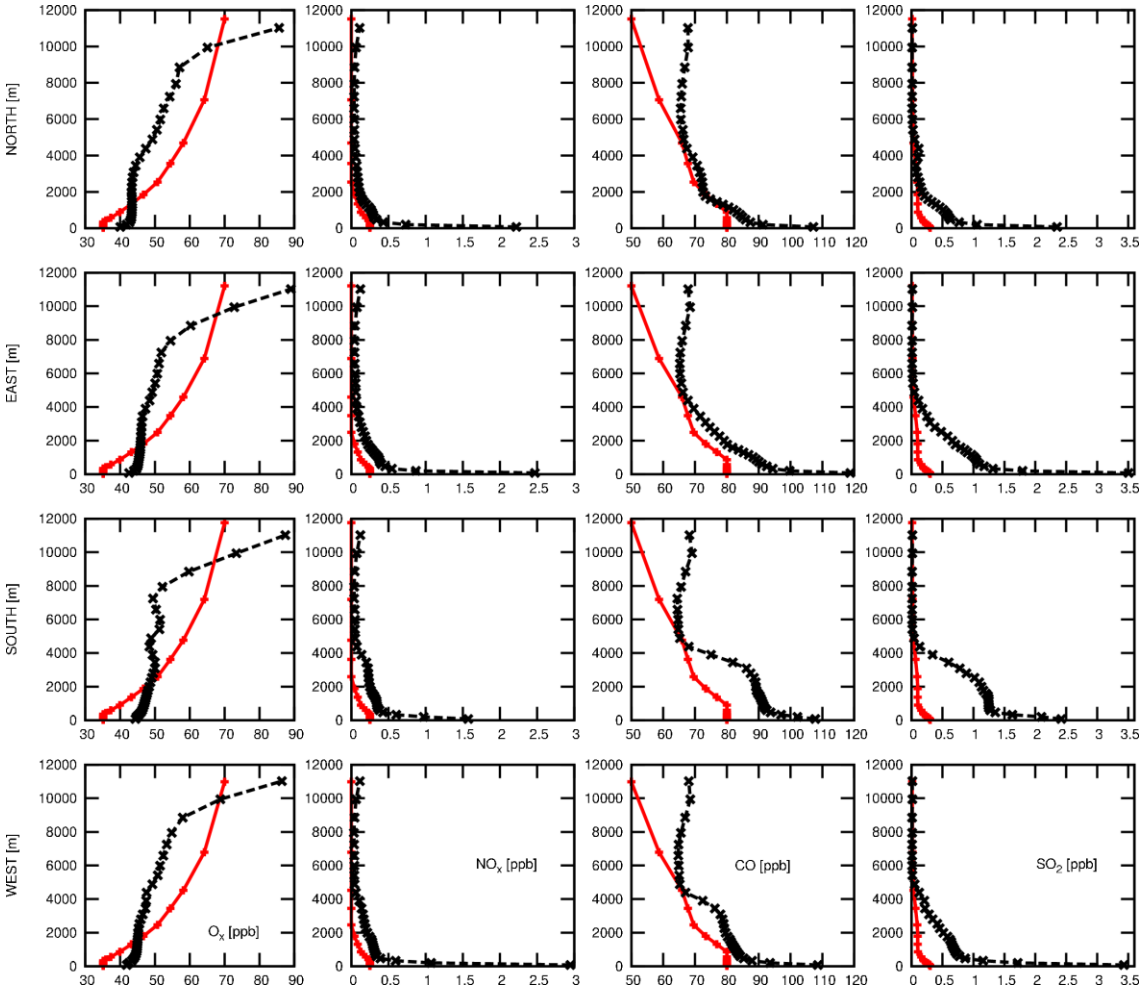

Figure 8 Vertical profile comparison of O_x, NO_x, CO, and SO_2 in GEOS-Chem (black) and CMAQ (red).

Figure 9 compares the vertical profiles of the primary organic carbon aerosol (AORG = OCPI + OCPO) for GEOS-Chem and CMAQ. The AORG profile follows a trend similar to that of NO_x and SO_2 in Figure 8 above showing decreasing concentrations at increasing altitudes. The higher concentrations predicted by the GEOS-Chem model shows influence from MCMA emissions to regional carbon aerosol loading, which implies that using the CMAQ default boundary conditions (representative for clean boundary layer) may lead to under-predictions in the CMAQ simulations.

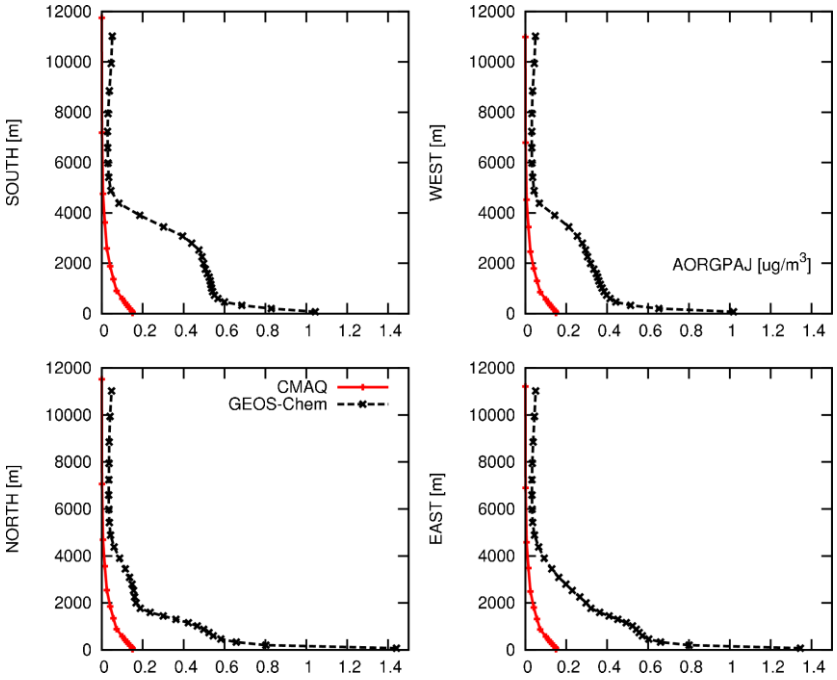

Figure 9 Vertical profile comparison of AORG in GEOS-Chem and CMAQ.

2.3.4 Time Series Comparison of GEOS-Chem and CMAQ

Direct validation of the GEOS-Chem results with measured concentrations at receptor locations is not practical due to the large grid size used in the GEOS-Chem simulation. The concentration at each grid represents the averaged concentration in the

grid, while the receptor concentrations are more influenced by local and nearby emission sources. In this study, the GEOS-Chem model predictions are compared with CMAQ results as an alternative model validation. Since the GEOS-Chem and CMAQ are based on entirely different treatment of emissions, meteorology, and atmospheric chemistry, the agreement between the models will provide confidence in the GEOS-Chem results.

The GEOS-Chem results are evaluated against CMAQ simulations through a time series comparison for selected species. The CMAQ simulation is performed using default BCON. More details of the CMAQ model and simulations are presented later on. All grid cells in the CMAQ model domain were averaged for each hour to get hourly averaged values. The appropriate grid cells in the NA GEOS-Chem simulation representing the CMAQ model domain were also averaged for a direct comparison.

Figure 10 shows a time series plot comparing O_x, NO_x, CO, and SO_2 for GEOS-Chem and CMAQ. In the instance of O_x and CO, GEOS-Chem results reasonably agree with the CMAQ results. In the instance of NO_x and SO_2, GEOS-Chem reports higher concentrations for the later days in the modeling period.

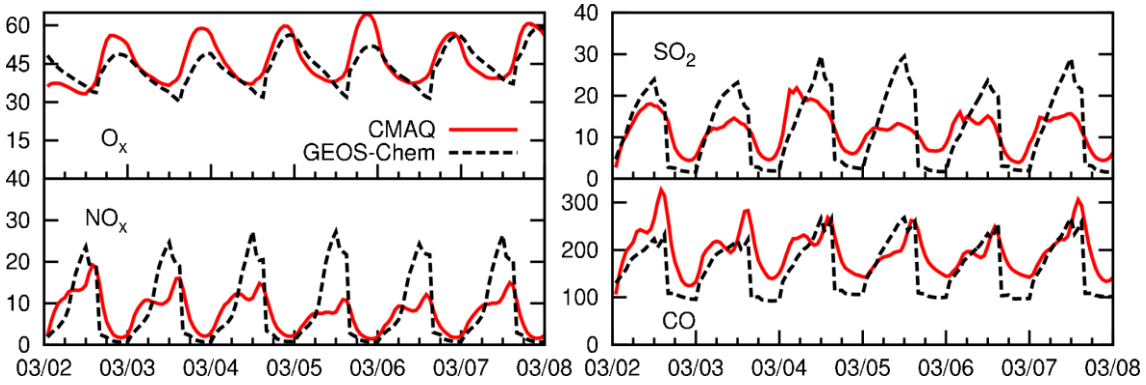

Figure 10 Time series comparison plots of O_x, NO_x, CO, and SO_2 for GEOS-Chem and CMAQ. All units are in ppbV.

The anthropogenic emissions for the MCMA region in the GEOS-Chem model is based on the 1999 Mexico NEI, which is generally higher in the emission rates than the updated emission inventory for 2006 used in the CMAQ simulation. The difference in the emissions could be one of the factors that lead to higher predictions. However, differences in meteorology, model chemistry, and transport cannot be easily ruled out.

2.4 Linking GEOS-Chem with CMAQ

From the GEOS-Chem output, hourly BCON for the regional model CMAQ are prepared using the GEOS2CMAQ intermediate program developed by Dr. Daewon Byun of the University of Houston. Aside from differing tracers and chemical schemes, GEOS-Chem output is written in sequential binary punch format while CMAQ uses the Input/Output Applications Programming Interface (IOAPI) libraries to generate output in network Common Data Form (netCDF format). Conversion of GEOS-Chem output to CMAQ BCON required temporal and spatial interpolation, chemical species mapping, and unit conversion. A summary of the linkage between GEOS-Chem and CMAQ with important components and processes is shown in Figure 11.

As the GEOS-Chem output was generated for every hour for the modeling period of March 2-7, 2006, the hourly CMAQ BCON was generated without the need for time-step interpolation. Spatial interpolation of the GEOS-Chem output was performed in conjunction with one of the Meteorology-Chemistry Interface Processor (MCIP) meteorology files that contain the relevant grid information such as map projection, horizontal domain resolution and center, latitude/longitude, as well as vertical resolution.

With the given information, the spatial interpolation is able to map GEOS-Chem data to the appropriate CMAQ domain while providing with estimated species concentration.

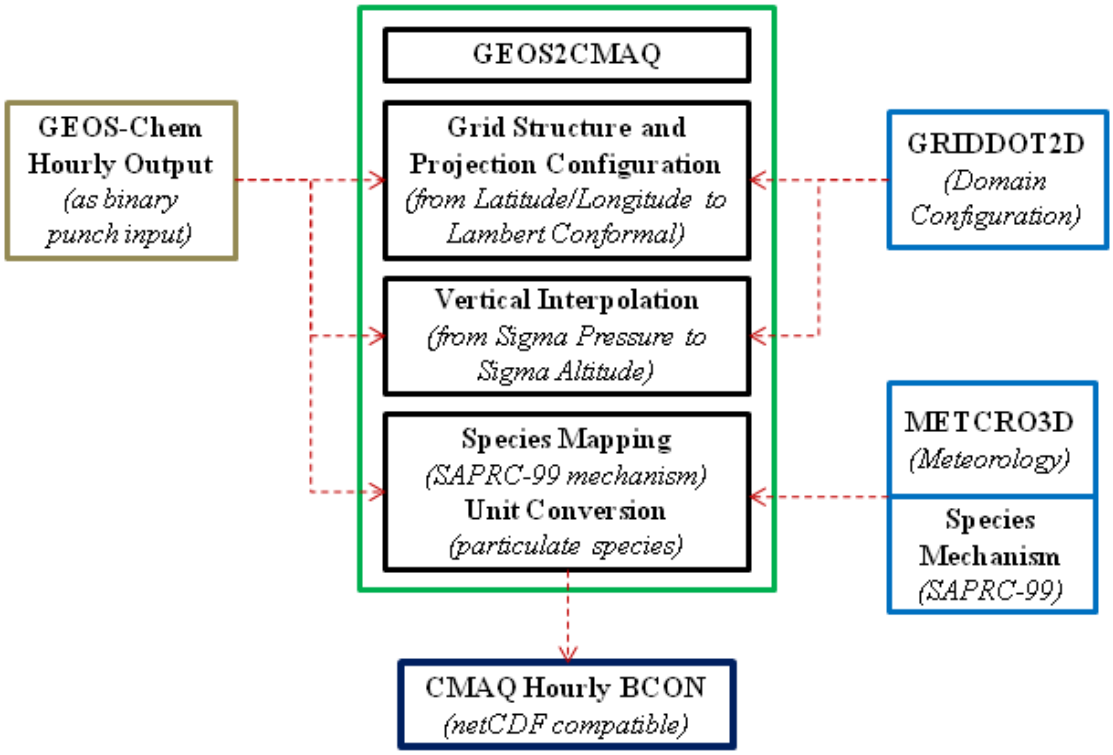

Figure 11 Linkage methodology of global to regional downscaling.

After spatial interpolation, the original GEOS-Chem tracers were mapped to match the SAPRCC-99 mechanism species so that they are properly represented in the regional simulations. Only a limited number of species were mapped while the remaining species were assigned default values by CMAQ. The list of GEOS-Chem species mapped to the SAPRC-99 mechanism is available in Appendix B. GEOS-Chem saves its tracer concentrations in volume ratio with dry air. Gaseous species are converted to ppm while particulate species are converted to $\mu g/m^3$ for CMAQ.

3. REGIONAL AIR QUALITY SIMULATIONS WITH CMAQ

With GEOS-Chem derived BCON, the next phase of the project moved towards the CMAQ simulations and a thorough analysis of the generated results. This section begins with a description of the CMAQ model system, its components and processes, and in what context are they applied to the project. The results have been processed and analyzed as a part of model evaluation followed by a statistical analysis scheme to measure model performance against observations. The section concludes with a particle trajectory analysis for selected species to identify the sources and transport of plume.

3.1 Model Description

CMAQ is a multi-pollutant, multi-resolution air quality model that can simulate regional atmospheric and terrestrial processes that affect transport, transformation, and deposition of atmospheric pollutants (Byun and Schere, 2006; Byun and Ching, 1999). Traditionally, air quality models are designed to work on a specific spatial scale (global, regional or urban) or for specific pollutants (photochemical ozone models, air toxics models, particulate models, visibility models, etc.). CMAQ is designed to manage regional air quality with a "one atmosphere" approach that treats air quality problems as a whole through the incorporation of up-to-date capabilities to work with tropospheric O_3 formation, fine particles, toxics, acid deposition, and visibility impairment. With CMAQ, one may better understand the physiochemical interactions of pollutants in the atmosphere to improve upon the region's existing air quality management practices. Figure 12 outlines the core components and processes of the CMAQ model system.

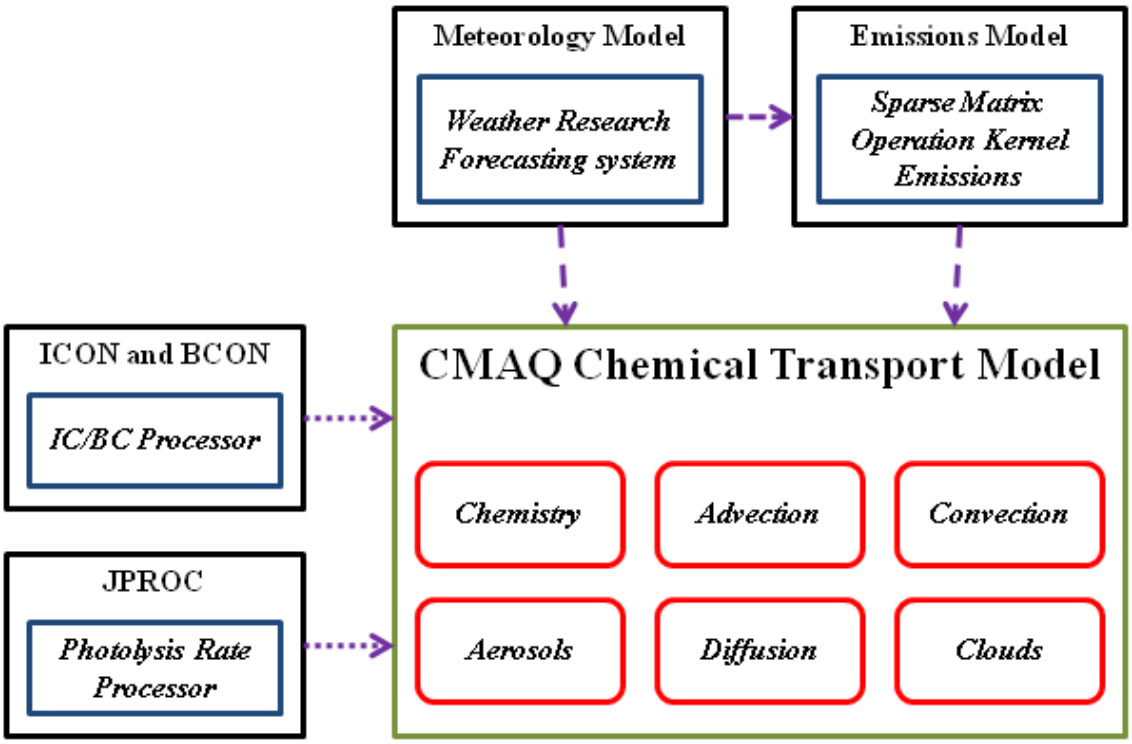

Figure 12 Schematic of the CMAQ model system.

CMAQ is made up of three primary components (meteorology, emissions, and a chemical transport model) and several interface processors (i.e., meteorology preprocessor MCIP, initial/boundary conditions preprocessors ICON/BCON, and photolysis rate preprocessor JPROC). The common meteorological modeling systems used for CMAQ are the Weather Research Forecasting system (WRF) and the 5th generation Mesoscale Modeling system (MM5). For this project, WRF-based meteorology fields are generated to be used in CMAQ. For the emission rate calculation of the biogenic component, the Sparse Matrix Operator Kernel Emissions (SMOKE) is the model used. CMAQ uses interface processors to incorporate the output data from these two components into the CTM, along with input information of initial/boundary

conditions (ICON/BCON) and photolysis rates generated by other processors. The emission models (SMOKE, for example) distributes the emissions of primary pollutants spatially and temporally and split emissions of total VOC into model VOC species used in the gas-phase chemical mechanisms (in this case, SAPRC-99) in the CMAQ model. Additionally, emissions of $PM_{2.5}$ and PM_{10} are split into aerosol chemical components for CMAQ simulations. The processes considered in CMAQ are emissions from sources, horizontal advection and diffusion, vertical advection and diffusion, chemical transformation and deposition.

The WRF meteorological fields are converted by the Meteorology-Chemistry Interface Processor (MCIP) for the CTM to use. MCIP can interpolate data, if needed, convert between coordinate systems, and compute cloud parameters as well as surface and planetary boundary layer parameters for the CTM.

The ICON/BCON programs are initial/boundary condition preprocessors that provide initial concentrations of the chemical species in the model domain and the concentrations of the species on the borders of the model domain, respectively. The ICON/BCON preprocessors can take previous CMAQ results from a coarse domain or use a set of default concentration profiles as inputs. As an alternative to the ICON/BCON programs, results from other CTMs, such as the GEOS-Chem model, can be processed to generate initial and boundary condition files for the CMAQ model.

The photolysis processor (JPROC) computes temporal photolysis rates for the CTM tabulating the results into a lookup table of photo-dissociation reaction rates.

3.1.1 Emissions Overview

Details on the emission processing for the CMAQ simulation are documented elsewhere (Ali et al., 2010) and a brief summary is provided below. Emissions of gaseous and particulate matter for MCMA used in this study are provided by Mexico City's Secretary of Environment based on the most recent update of the 2006 emission inventory. Emissions from point sources are based on the work-hours of the different industries which generally operate eight hours or more per day. The emissions generated by area sources are collected using emission factors based on population and census information. The emissions from mobile sources of major fuel types (i.e. gasoline, diesel, LPG, and natural gas) are calculated using the emission factors generated by the MOBILE5-Mexico model and the kilometers traveled in a day for the vehicle.

The speciation profiles used to split the total VOCs emissions into individual SAPRC-99 model species, and $PM_{2.5}$ emissions into elemental carbon (EC), organic compounds (OC), nitrate, sulfate and other components are from the SPECIATE 3.2 database. The raw emissions provided were processed using in-house programs to generate CMAQ ready inputs. Table 1 lists the emission rate of gas and particulate pollutants for area, mobile, and point sources in the MCMA for a typical day based on averaged emissions during March 2-7, 2006.

In addition to anthropogenic emissions from MCMA, this study also includes emissions of gaseous species from biogenic sources, windblown dust emissions of particulate matter from soil as well as emissions from other point sources outside the MCMA. Details of this part of the emissions can also be found in Ali et al. (2010).

Table 1 List of daily emissions of selected species in the MCMA. Gaseous species are saved in the units of kmole/day. Particulate species are saved in the units of ton/day

SPECIES	ANTHROPOGENIC			BIOGENIC
	AREA	MOBILE	POINT	
CO [kmole/day]	139,036	9,204,957	28,385	93,225
NOx	25,264	442,029	56,906	
SO2	523	5,033	6,122	
ETHENE	8,573	54,508	47,253	14,041
ALK1	9,238	13,914	6,459	3,107
ALK2	11,279	12,128	9,518	1,903
ALK3	25,701	60,427	12,359	14,041
ALK4	24,263	65,524	12,261	
ALK5	96,579	36,796	22,244	
ARO1	20,354	20,830	31,922	
ARO2	11,374	33,859	4,450	
BENZENE	7,243	4,922	2,496	
OLE1	5,765	20,941	22,041	25,416
OLE2	3,889	26,647	3,969	4,305
ISOPRENE	226	286	330	41,291
TRP1	494	651	280	17,844
SESQ				789
PM10 [ton/day]	377	726	487	
PMC	54.9	318	407	
PM2_5	322	407	80.8	
PMFINE	22.2	48.6	69.1	
PEC	51.7	173	1.03	
PNO3	0.67	0.43	0.02	
PSO4	8.84	6.49	0.48	
POA	239	179	10.2	

3.1.2 Meteorology Simulation Results

The meteorology input data was provided using the WRF model. WRF model simulations and analysis were conducted by Hongliang Zhang of our research group. For completeness of the thesis, the results of the WRF simulations are summarized below by

comparing with observations. A detailed list of the meteorology observation stations can be found in Appendix C.

Figure 13 shows that the WRF model generally captures the diurnal variation of the wind speed in the MCMA. Wind speed is highest in the later afternoon and lower at night and early morning hours. The WRF predictions are slightly higher than the observations. The predicted wind directions agree better with observations when wind speed is higher but there are larger differences when the wind speed is low. The differences in the wind directions are not likely to significantly affect air quality model results because of the slower wind speed.

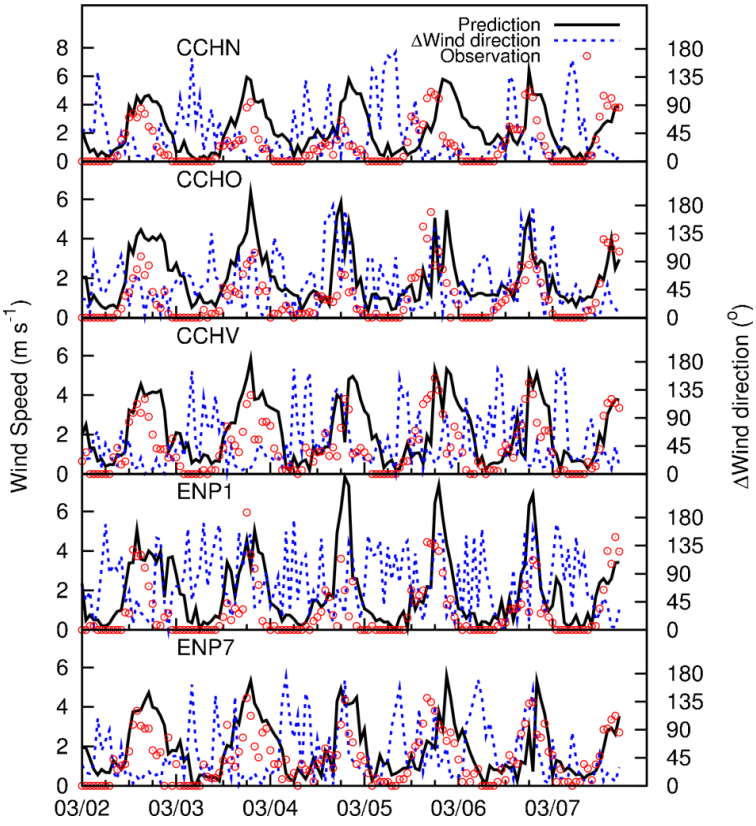

Figure 13 Predicted and observed surface wind speed and the difference between the observed and predicted wind direction.

Figure 14 shows that the predicted temperature and relative humidity agrees well with observations. The WRF model seems to over-predict relative humidity at all stations on the morning of March 5th and 7th by approximately 20% but otherwise the predictions are reasonably well.

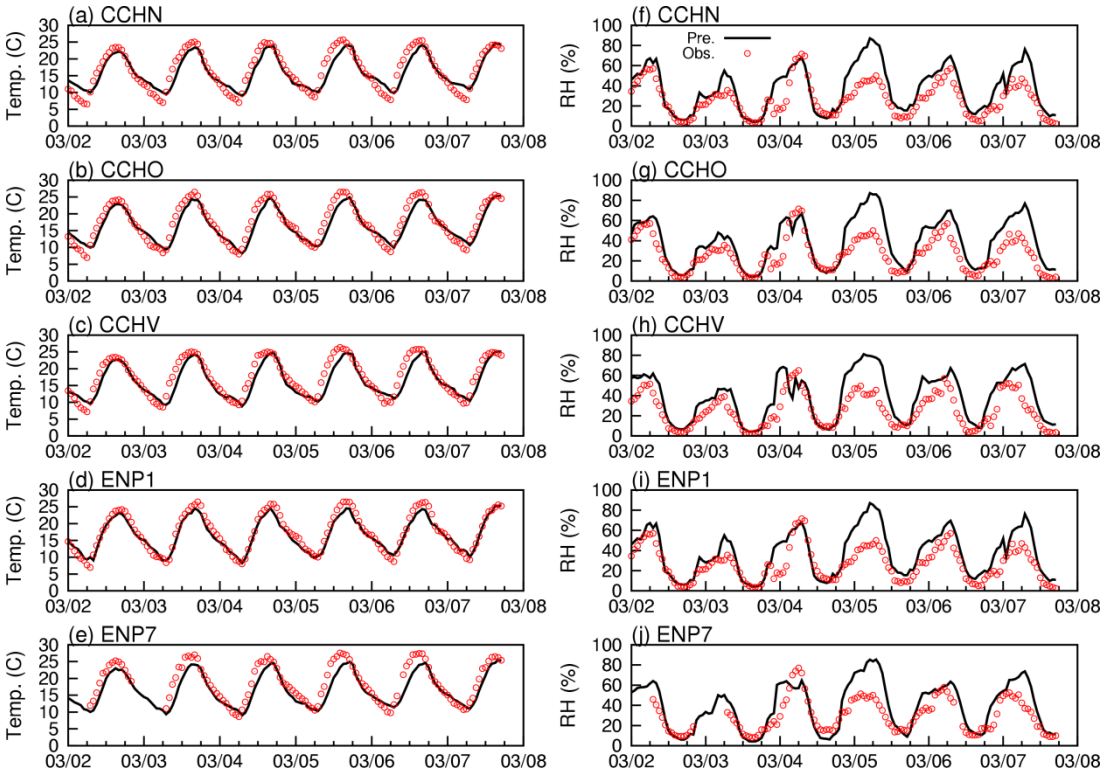

Figure 14 Predicted and observed surface temperature and relative humidity.

3.2 Model Application

The model simulation is conducted for the period of March 2-7, 2006. CMAQ v4.7 performs simulations in the 200x200 model domain which has a fine horizontal resolution of 1 km. The fine horizontal resolution was chosen to ensure that steep concentration gradients near emission sources can be better captured and more emissions

that have potentials to affect air quality in MCMA are included. The vertical domain is divided into 16 vertical layers with a model top of 12 km above surface.

Two main sets of simulations have been performed: the base case run and the GEOS-Chem BCON case run. In addition to that set, secondary runs with GEOS-Chem BCON were performed as a part of the sensitivity analysis run with a range of vertical diffusivity values. Vertical diffusivity impacts pollutant mixing in the atmosphere and may determine how high or low the pollutant plume can spread across the column.

Figure 15 shows the CMAQ model domain and the landmarks that are relevant to the project. The Tula industrial complex is an important source region with a number of large point sources of emissions that contribute with NO_x, SO_2, and PM to the MCMA air pollution (Molina and Molina, 2002). The Popocatépetl volcano is an active volcano that emits significant amounts of SO_2 (de Foy et al., 2007).

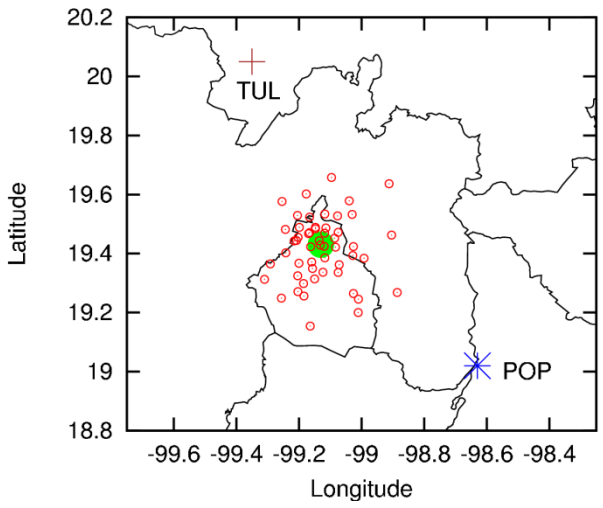

Figure 15 Map of the CMAQ model domain showing the monitoring stations (red), Mexico City Center (circle), Tula industrial complex (brown), and the Popocatépetl volcano (blue).

3.3 Evaluation of Results

Predictions have been compared with observations at various monitoring stations in the MCMA. During post-processing, the locations of the monitoring stations were mapped to the 200x200 domain to get the appropriate predictions for comparison with observations. The complete list of the monitoring stations with hourly measurements can be found in Appendix C. Not all of the monitoring stations listed here have complete data. The monitoring stations that have no data available for the modeling episode have been excluded from post-processing and further analysis.

3.3.1 Time Series Plots

Appendix C contains the list of monitoring stations in the MCMA that are gathering hourly species concentrations for O_3, CO, NO_x, SO_2, PM_{10}, and $PM_{2.5}$ species during 2006. Figure 15 shows the location of these monitoring stations spread throughout the MCMA which can also be confirmed with the coordinates provided in Appendix C. Time series plots of each species are shown and explained in this section.

Figure 16 shows the time series plot comparing observation of O_3 concentration with the base case predictions and GEOS-Chem BCON. Both cases reasonably predict the observation trends found throughout the episode for each station. The cases not quite able capture some of the peak periods as shown in EAC, HAN, and PED. Still, the essential diurnal variations have not been missed. The GEOS-Chem case, in comparison with the base case, predicts slightly higher concentration at all stations. The differences in O_3 concentrations are likely due to higher O_3 BCON produced by the GEOS-Chem at higher elevations.

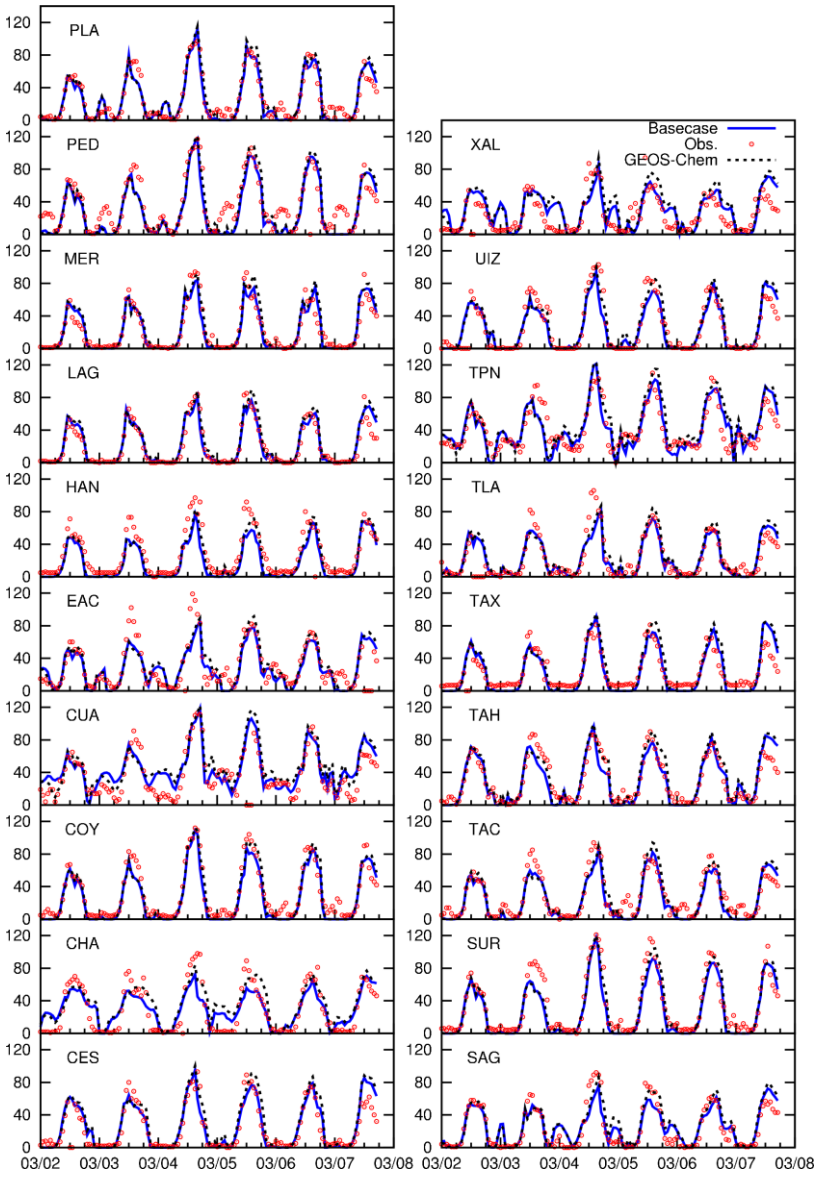

Figure 16 Time series plot comparing O_3 observations against the base case and GEOS-Chem BCON case. All units are in ppb.

Figure 17 compares NO_x observations with both cases. Both cases are able to predict most of the peak trends with some under prediction at CES, TAX, TLA, and XAL. Concentrations are over-predicted at PLA, MER, and LAG, which are all located near the urban center. This suggests that emission or vertical mixing of NO_x might be

under-predicted in the CMAQ model. Both cases are close in comparison with the GEOS-Chem case predicting slightly higher concentrations.

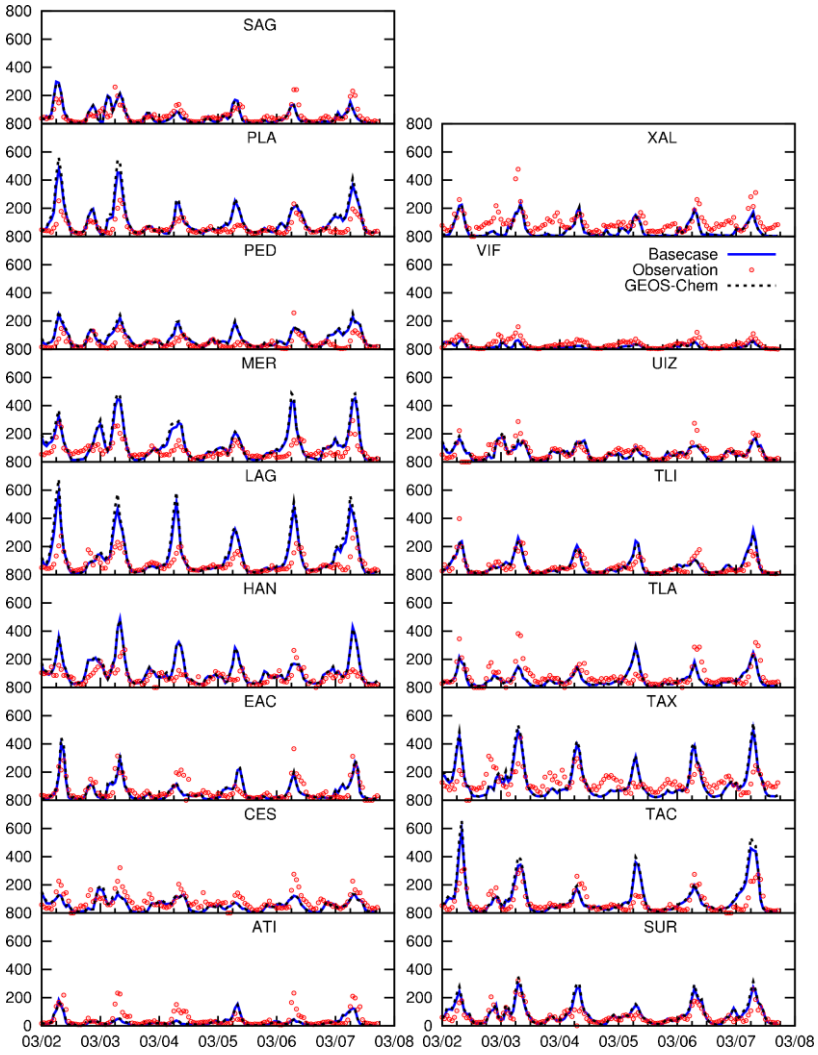

Figure 17 Time series plot comparing NO_x observations against the base case and GEOS-Chem BCON case. All units are in ppb.

Figure 18 shows CO observations being compared against the two cases. With the exception of some stations (namely EAC, HAN, and UIZ), both cases do not correctly predict the concentrations. In some cases, even the base case shows higher

levels than the GEOS-Chem case. While both cases are seeking to follow the peak trends, the peaks are either too high (LAG, MIN.PED) or too low (TLI, VIF, XAL).

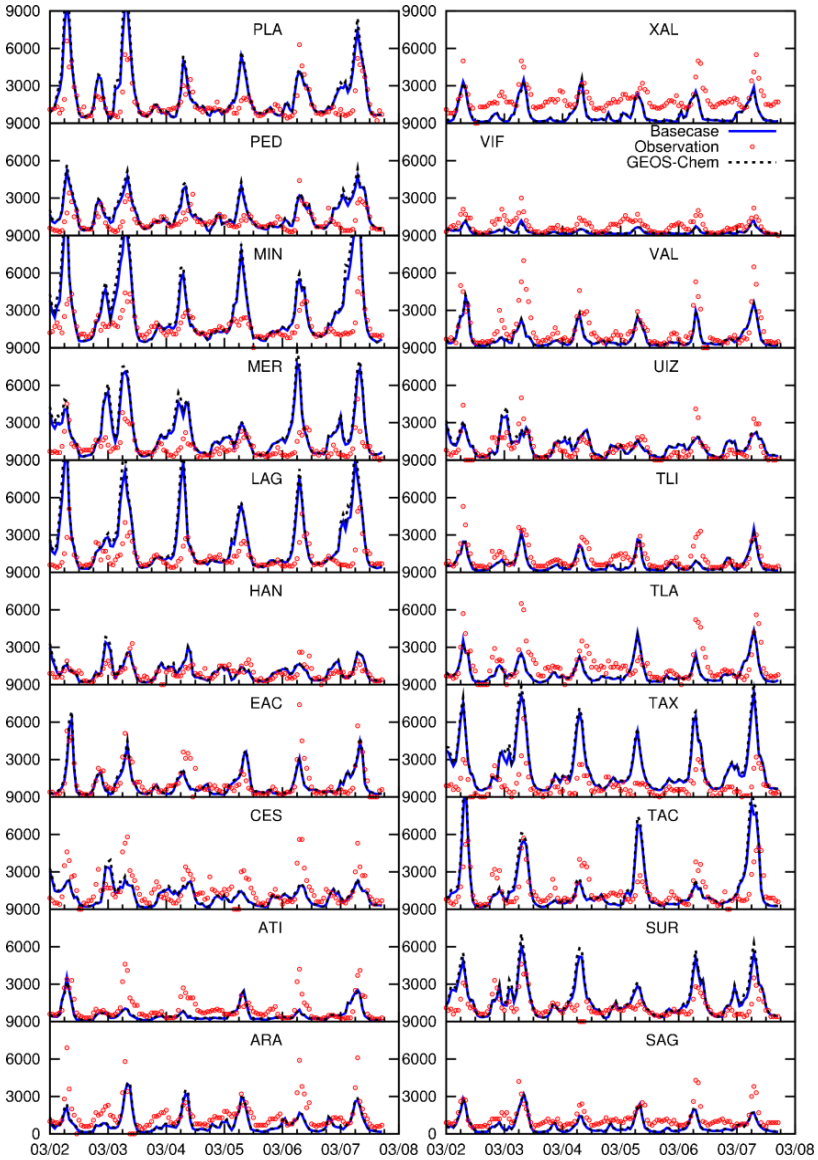

Figure 18 Time series plot comparing CO observations against the base case and GEOS-Chem BCON case. All units are in ppb.

Figure 19 shows the comparison of SO_2 observations against the two cases. The performance for both cases is adequate at all stations as they match the peak trends on

most days. However, the highest SO_2 peak that occurs on March 4 at most stations is not captured in either case. This may point to an oversight in emissions processing and the exclusion of some major sources, such as a major volcano plume event. The particle trajectory analysis discussed towards the end of this section shall focus solely on SO_2, its possible sources of emissions, and its path of transport across the MCMA.

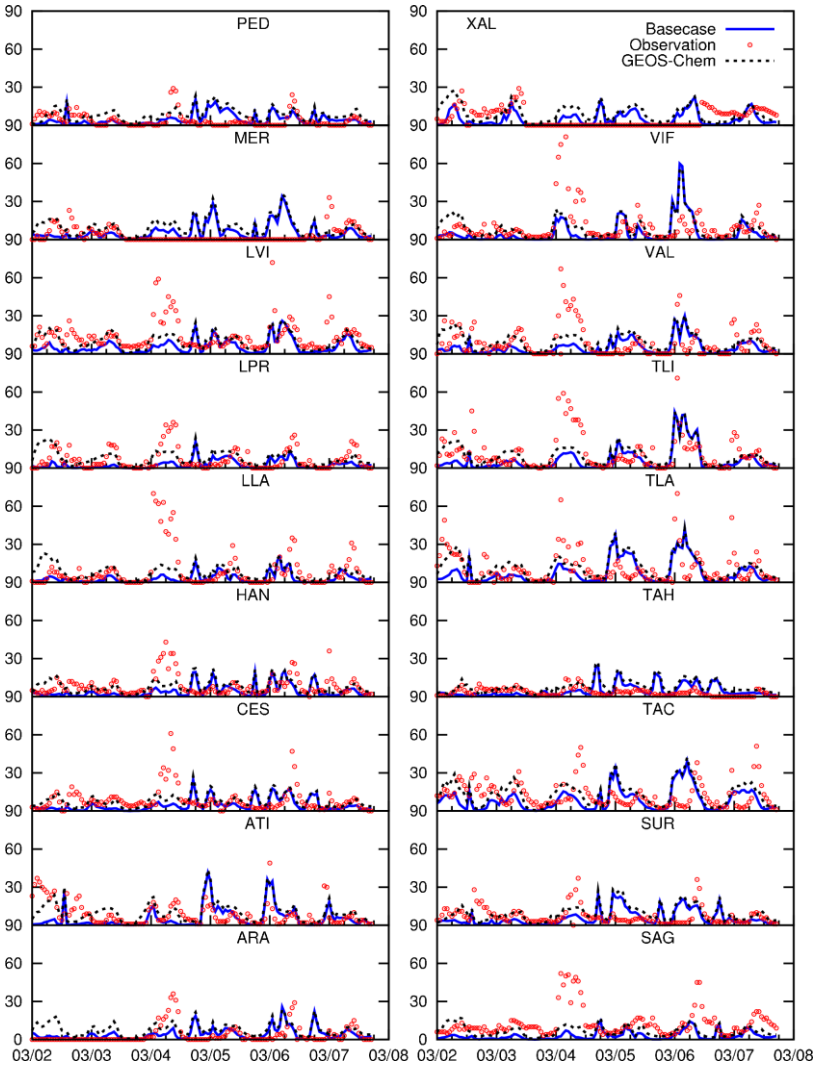

Figure 19 Time series plot comparing SO_2 observations against the base case and GEOS-Chem BCON case. All units are in ppb.

Figure 20 shows PM_{10} observations compared with the two cases. Both cases are almost congruent in predicting reasonably the scattered observation trends. For some stations such as CES, HAN, SAG, TAH, VIF, and XAL, both cases miss the observed peaks. Both cases, however, do show high PM_{10} concentration days at March 5, 6, and 7. Overall both cases have fairly predicted the concentration trends at each station.

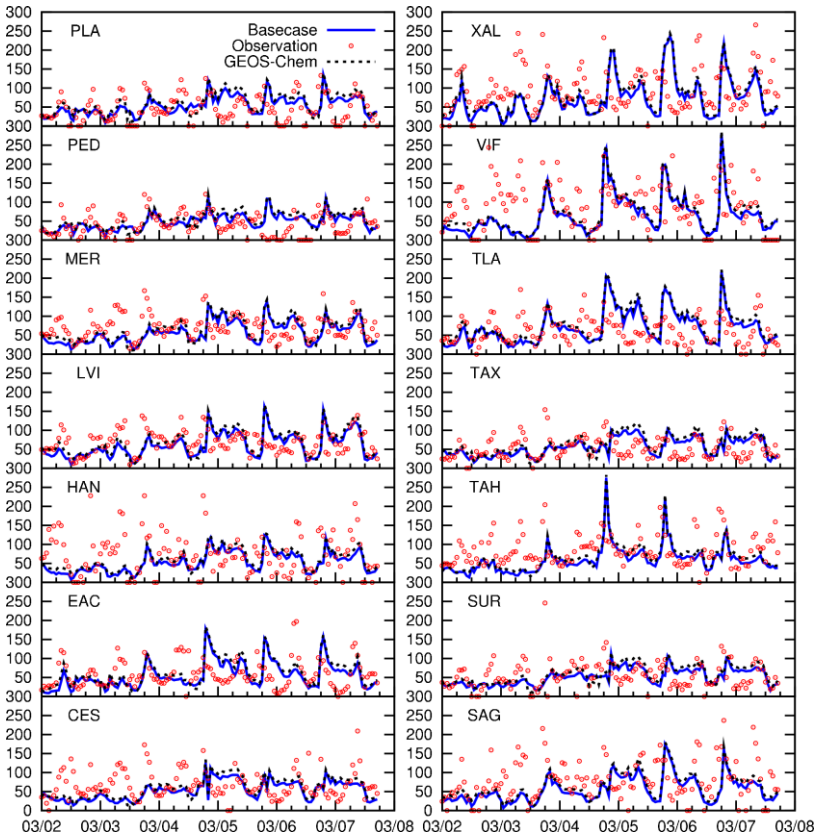

Figure 20 Time series plot comparing PM_{10} observations against the base case and GEOS-Chem BCON case. All units are in $\mu g/m^3$.

Figure 21 shows $PM_{2.5}$ observations compared with both cases at eight monitoring stations. Both cases can match the observation levels at CAM, COY, MER, and UIZ. Early and latter peaks have been missed in MER, PER, and SJA. The observed

peaks at these stations generally occur at noon (local time) suggesting that most of the PM is secondary in origin. It is likely that the current CMAQ model misses some of the secondary formation pathways. The GEOS-Chem case shows higher levels of $PM_{2.5}$ than the original base case.

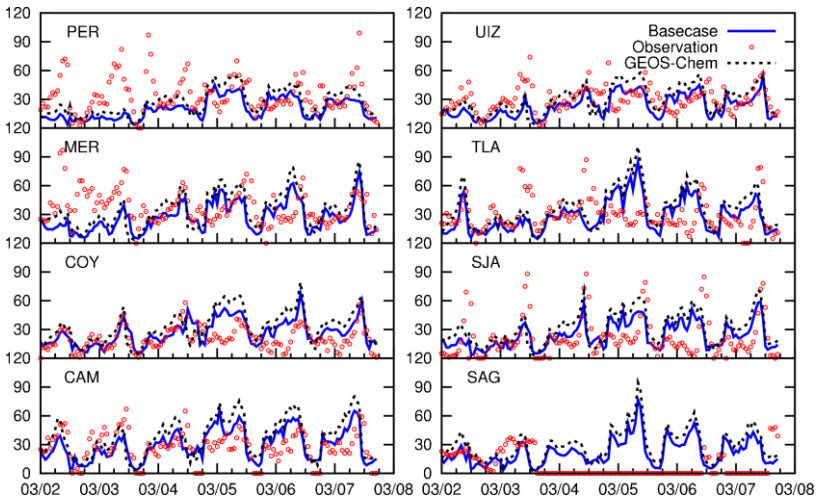

Figure 21 Time series plot comparing $PM_{2.5}$ observations against the base case and GEOS-Chem BCON case. All units are in $\mu g/m^3$.

3.3.2 Statistical Performance Analysis

Statistical measures are used to evaluate the performance of the CMAQ model on hourly O_3, NO_x, CO, PM_{10}, and $PM_{2.5}$ at all available monitoring stations during the modeling period of March 2-7, 2006. The list of statistical parameters used and their definition is given in Table 2. The statistical parameters are dimensionless and can be applied to any dataset with observation and prediction numbers. The peak measures are applied to O_3 only.

Table 2 Statistical performance parameters and their definitions.

STATISTICAL PARAMETER	EQUATION
Mean Fractional Bias	$MFB = \frac{2}{N}\sum_{i=1}^{N}\frac{(C_{pred,i} - C_{obs,i})}{(C_{pred,i} + C_{obs,i})}$
Mean Fractional Error	$MFE = \frac{2}{N}\sum_{i=1}^{N}\frac{\lvert C_{pred,i} - C_{obs,i}\rvert}{(C_{pred,i} + C_{obs,i})}$
Accuracy of Paired Peak	$APP = \frac{1}{N}\sum_{i=1}^{N}\frac{\left(C_{pred}(pk\_obs) - C_{obs}(pk\_obs)\right)}{C_{obs}(pk\_obs)}$
Accuracy of Unpaired Peak	$AUP = \frac{1}{N}\sum_{i=1}^{N}\frac{\left(C_{pred}(pk\_pred) - C_{obs}(pk\_obs)\right)}{C_{obs}(pk\_obs)}$
Absolute Accuracy of Paired Peak	$AAPP = \frac{1}{N}\sum_{i=1}^{N}\frac{\lvert C_{pred}(pk\_obs) - C_{obs}(pk\_obs)\rvert}{C_{obs}(pk\_obs)}$
Absolute Accuracy of Unpaired Peak	$AAUP = \frac{1}{N}\sum_{i=1}^{N}\frac{\lvert C_{pred}(pk\_pred) - C_{obs}(pk\_obs)\rvert}{C_{obs}(pk\_obs)}$

For O_3 performance, an observation-based threshold concentration of 60 ppb was set to exclude lower values from the statistical analysis (Ying et al., 2007). This threshold value was applied to exclude the effects of low observation points on the overall species statistics. The threshold value also removes any points that have no observation data for comparison with the predictions.

Table 3 and Table 4 show the calculated performance statistics for O_3 at various monitoring stations. Almost all of the monitoring stations are under-predicting O_3 concentrations as shown by MFB (average value of around -0.2). The GEOS-Chem case predictions are better in comparison with the base case as shown by the lower MFE

values. The GEOS-Chem case also performs reasonably better than the base case in matching peak observations even though the overall dataset still reveals some under-prediction.

Table 3 O_3 performance statistics for the CMAQ modeling episode.

STN	BASECASE		GEOS-Chem		POINTS
	MFB	MFE	MFB	MFE	
CES	-0.09	0.18	0.02	0.19	21
CHA	-0.32	0.32	-0.16	0.20	29
COY	-0.17	0.19	-0.10	0.15	33
CUA	-0.03	0.18	0.02	0.20	28
EAC	-0.24	0.24	-0.18	0.24	21
HAN	-0.38	0.39	-0.26	0.29	24
LAG	-0.14	0.16	-0.04	0.13	13
MER	-0.15	0.20	-0.06	0.17	16
PED	-0.15	0.18	-0.09	0.17	31
PLA	-0.07	0.15	-0.02	0.16	23
SAG	-0.34	0.34	-0.20	0.20	14
SUR	-0.23	0.24	-0.15	0.20	36
TAC	-0.15	0.20	-0.10	0.20	21
TAH	-0.13	0.18	-0.01	0.13	25
TAX	-0.05	0.15	0.03	0.18	16
TLA	-0.24	0.25	-0.15	0.26	14
TPN	-0.04	0.22	0.02	0.21	34
UIZ	-0.18	0.25	-0.09	0.21	28
XAL	-0.35	0.38	-0.21	0.27	8
Overall	-0.18	0.23	-0.09	0.20	435

Table 4 Peak O_3 performance statistics for the CMAQ modeling episode.

STN	BASECASE				GEOS-Chem				POINTS
	APP	AAPP	AUP	AAUP	APP	AAPP	AUP	AAUP	
CES	-0.20	0.22	-0.06	0.11	-0.12	0.18	0.01	0.13	4
CHA	-0.39	0.39	-0.27	0.27	-0.29	0.29	-0.17	0.17	5
COY	-0.14	0.14	-0.08	0.08	-0.11	0.11	-0.05	0.07	5
CUA	-0.11	0.17	0.01	0.10	-0.05	0.16	0.05	0.13	5
EAC	-0.26	0.26	-0.21	0.21	-0.19	0.22	-0.13	0.18	5
HAN	-0.39	0.39	-0.29	0.29	-0.35	0.35	-0.22	0.22	5
LAG	-0.14	0.14	-0.03	0.04	-0.08	0.10	0.06	0.06	4
MER	-0.23	0.23	-0.08	0.11	-0.18	0.18	-0.01	0.09	4
PED	-0.13	0.13	-0.05	0.06	-0.10	0.11	-0.01	0.07	5
PLA	0.01	0.13	0.07	0.11	0.05	0.12	0.11	0.11	4
SAG	-0.28	0.28	-0.16	0.16	-0.22	0.22	-0.07	0.14	4
SUR	-0.20	0.20	-0.15	0.15	-0.17	0.17	-0.11	0.11	5
TAC	-0.26	0.26	-0.13	0.16	-0.23	0.23	-0.06	0.17	4
TAH	-0.09	0.11	-0.01	0.11	-0.03	0.09	0.04	0.13	5
TAX	-0.12	0.18	-0.01	0.15	-0.07	0.15	0.06	0.19	4
TLA	-0.28	0.28	-0.20	0.20	-0.21	0.29	-0.13	0.22	3
TPN	-0.15	0.16	-0.03	0.12	-0.09	0.11	0.01	0.11	5
UIZ	-0.26	0.26	-0.11	0.13	-0.19	0.19	-0.05	0.11	5
XAL	-0.47	0.47	-0.17	0.17	-0.41	0.41	-0.05	0.13	2
Overall	-0.22	0.23	-0.10	0.14	-0.16	0.19	-0.04	0.13	83

For NO_x performance, an observation-based threshold concentration of 100 ppb was set to exclude lower values from the statistical analysis. Table 5 show the calculated performance statistics for NO_x at various monitoring stations. NO_x cases reveal deeper values for both MFB and MFE. There is both over-prediction and under-prediction of NO_x taking place at the monitoring stations. Both cases perform similarly under MFB and MFE (average values of -0.2 and 0.6 respectively).

Table 5 NO_x performance statistics for the CMAQ modeling episode.

STN	BASECASE		GEOS-Chem		POINTS
	MFB	MFE	MFB	MFE	
ATI	-0.96	0.97	-0.94	0.94	21
CES	-0.55	0.62	-0.52	0.61	38
EAC	-0.46	0.57	-0.41	0.55	28
HAN	0.18	0.40	0.21	0.40	37
LAG	0.35	0.53	0.41	0.57	34
MER	0.35	0.49	0.40	0.53	33
PED	0.18	0.30	0.24	0.34	14
PLA	0.39	0.43	0.46	0.48	27
SAG	-0.31	0.61	-0.32	0.60	24
SUR	0.15	0.32	0.24	0.35	27
TAC	-0.06	0.54	0.02	0.56	36
TAX	-0.31	0.61	-0.28	0.62	87
TLA	-0.63	0.67	-0.63	0.66	33
TLI	-0.11	0.39	-0.13	0.37	25
VAL	-0.27	0.34	-0.23	0.33	28
VIF	-0.86	0.86	-0.96	0.96	6
XAL	-0.81	0.86	-0.81	0.86	46
Overall	-0.22	0.56	-0.19	0.57	544

For CO performance, an observation-based threshold concentration of 2000 ppb was set to exclude lower values from the statistical analysis. Table 6 show the calculated performance statistics for CO at various monitoring stations. The results show that almost all of the monitoring stations are under-predicting CO (the exception being PED, PLA, SUR, and TAX). MFB performance of the GEOS-Chem case is much lower (average of -0.25) in comparison to that of the base case (-0.8). The MFE performance of CO shows a slightly better performance by the GEOS-Chem case (averaging around 0.5) in comparison with the base case (0.9) which may be in part due to base case under-predictions.

Table 6 CO performance statistics for the CMAQ modeling episode.

STN	BASECASE		GEOS-Chem		POINTS
	MFB	MFE	MFB	MFE	
ARA	-1.42	1.42	-0.52	0.61	23
ATI	-1.23	1.23	-0.73	0.73	17
CES	-1.01	1.01	-0.72	0.72	33
EAC	-1.22	1.22	-0.43	0.51	27
HAN	-0.38	0.50	-0.46	0.49	6
IMP	-1.56	1.56	0.07	0.41	12
LAG	-1.12	1.12	0.42	0.55	24
MER	-0.13	0.43	0.37	0.51	18
MIN	-0.74	0.78	0.39	0.52	35
PED	0.23	0.57	0.09	0.32	20
PLA	-0.10	0.49	0.24	0.38	30
SAG	-1.08	1.08	-0.49	0.53	19
SUR	0.59	0.61	0.23	0.38	16
TAC	-0.70	0.75	-0.17	0.66	33
TAX	0.38	0.48	0.58	0.64	16
TLA	-1.09	1.09	-0.72	0.77	30
TLI	-1.37	1.37	-0.56	0.58	23
UIZ	-0.32	0.41	-0.28	0.42	13
VAL	-1.13	1.13	-0.66	0.69	28
VIF	-1.55	1.55	-0.99	0.99	4
XAL	-1.34	1.34	-0.83	0.85	41
Overall	-0.78	0.96	-0.25	0.58	468

For PM_{10} performance, an observation-based threshold concentration of 25 $\mu g/m^3$ was set to exclude lower values from the statistical analysis. Table 7 show the calculated performance statistics for PM_{10} at various monitoring stations. Both cases have under-predicted to the observed values at all monitoring stations, except for TAX and TLA for the GEOS-Chem case. The GEOS-Chem case has statistically performed better with overall MFB (average of -0.15) than the base case (-0.25). The MFE for both cases is very close (average value of 0.5) indicating some effects of over-predicting hours.

Table 7 PM_{10} performance statistics for the CMAQ modeling episode.

STN	BASECASE		GEOS-Chem		POINTS
	MFB	MFE	MFB	MFE	
CES	-0.31	0.56	-0.20	0.52	133
EAC	-0.21	0.56	-0.07	0.51	127
HAN	-0.44	0.62	-0.31	0.55	116
LVI	-0.17	0.45	-0.05	0.42	134
MER	-0.29	0.51	-0.17	0.45	138
PED	-0.18	0.41	-0.06	0.40	97
PLA	-0.14	0.42	-0.03	0.39	99
SAG	-0.45	0.61	-0.32	0.53	127
SUR	-0.15	0.45	-0.05	0.43	121
TAH	-0.39	0.54	-0.28	0.49	141
TAX	-0.03	0.45	0.07	0.47	124
TLA	-0.04	0.52	0.09	0.49	129
VIF	-0.47	0.66	-0.35	0.58	118
XAL	-0.38	0.65	-0.26	0.58	137
Overall	-0.26	0.53	-0.14	0.49	1741

For $PM_{2.5}$ performance, an observation-based threshold concentration of 5 $\mu g/m^3$ was set to exclude lower values from the statistical analysis. Table 8 show the calculated performance statistics for $PM_{2.5}$ at various monitoring stations. For both cases, about half of the receptor locations are under-predicting the observed values. CAM, COY, SJA, and TLA stand out with one or both of the cases displaying over-predicted values. While the GEOS-Chem case reports a lower MFB than the base case (average at -0.02 to -0.2), the MFE remains quite close (0.5 for both) owing to some fraction of points that are over-predicting $PM_{2.5}$ concentrations.

Table 8 $PM_{2.5}$ performance statistics for the CMAQ modeling episode.

STN	BASECASE		GEOS-Chem		POINTS
	MFB	MFE	MFB	MFE	
CAM	-0.06	0.45	0.16	0.49	119
COY	0.17	0.42	0.35	0.51	129
MER	-0.38	0.59	-0.17	0.54	141
PER	-0.53	0.64	-0.27	0.53	138
SAG	-0.54	0.61	-0.20	0.46	49
SJA	0.05	0.59	0.29	0.67	111
TLA	-0.14	0.54	0.08	0.52	138
UIZ	-0.28	0.48	-0.05	0.44	138
Overall	-0.21	0.54	0.02	0.52	963

With the exception of O_3, both NO_x and CO presented similar performance statistics for both cases. In the case of NO_x, the base case generally performs slightly better than the GEOS-Chem case while some monitoring stations in CO appear to be affecting the GEOS-Chem case more intensely. In the case of O_3, the GEOS-Chem case performs favorably to match the observations.

3.3.3 Sensitivity Analysis with Vertical Diffusivity

The vertical diffusivity (k_{zz}) in the current CMAQ model is based on boundary layer similarity theory. It is a known issue that the predicted k_{zz} could not appropriately account for the observed mixing at night or during inversion when the predicted k_{zz} is too small near the surface. As an empirical fix to this problem, a minimal k_{zz} is used in the CMAQ model so that when the predicted k_{zz} is lower, the minimal diffusivity will be used instead. A set of simulations were performed where the k_{zz} parameter was set to 0.1, 1.0 (base case), and 2.0 m^2/s using GEOS-Chem BCON.

Figure 22 shows the comparison of O_3 observation against various k_{zz} cases. No major differences can be identified among the three cases especially for peak trends. The GEOS-Chem base case (k_{zz}=1.0) still shows higher O_3 levels than 0.1 and 2.0 cases.

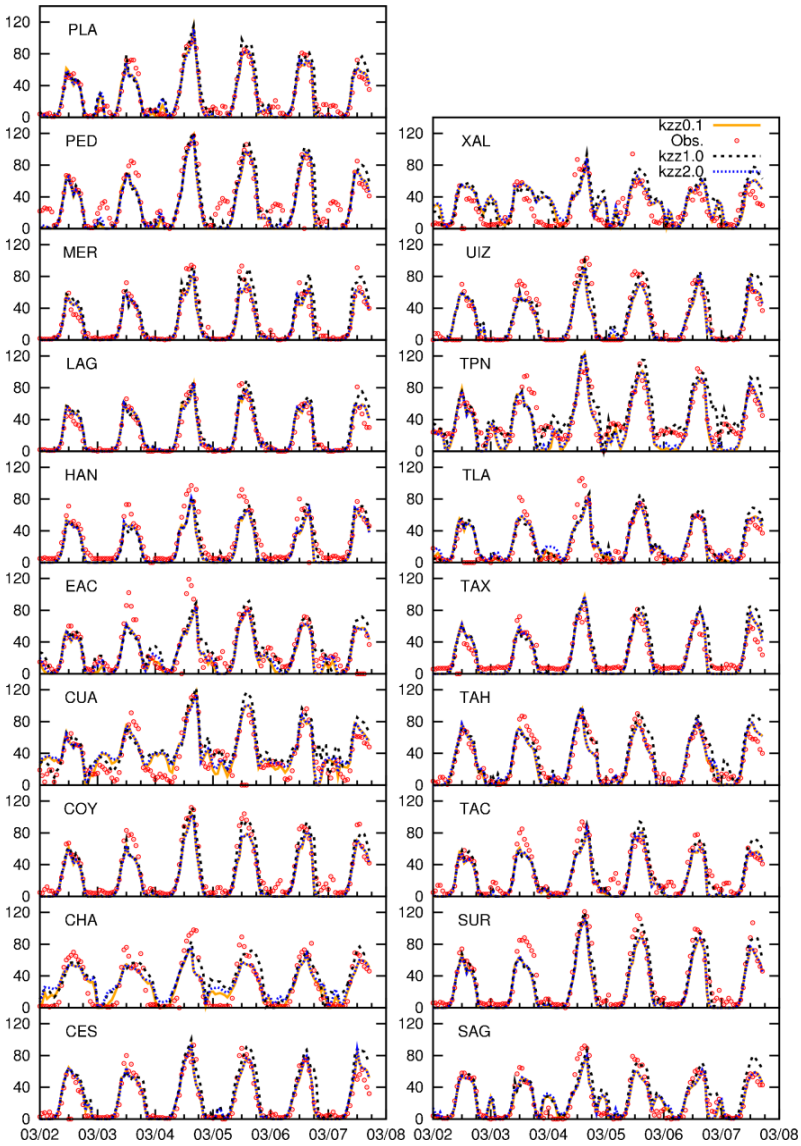

Figure 22 Sensitivity analysis of O_3 using k_{zz} at 0.1, 1.0, and 2.0. All units are in ppb.

Figure 23 shows NO_x observations with the k_{zz} cases. This time, the 0.1 case predicts the higher concentrations at most stations followed by the 1.0 case and then the

2.0 case. It may be inferred from this analysis that the 2.0 case was the closest to observation numbers where the other two cases were over predicting.

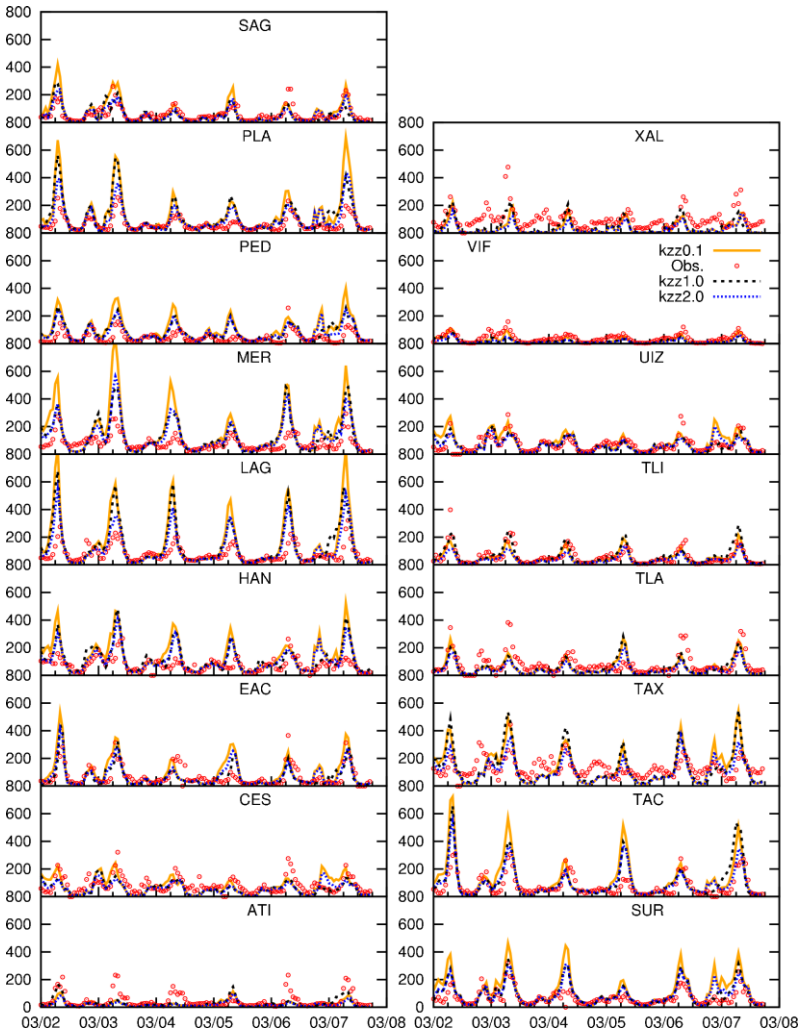

Figure 23 Sensitivity analysis of NO_x using k_{zz} at 0.1, 1.0, and 2.0. All units are in ppb.

Figure 24 shows the CO observations compared with the k_{zz} cases. Similar to NO_x, the 0.1 case shows the highest predictions at most stations with the 2.0 case being much closer to observation. Similar to the CO time series plot, the scaling of k_{zz}

parameter could not reduce the under prediction at the stations ATI, SAG, TLA, and XAL. Further scaling of the parameter may be seriously considered for CO.

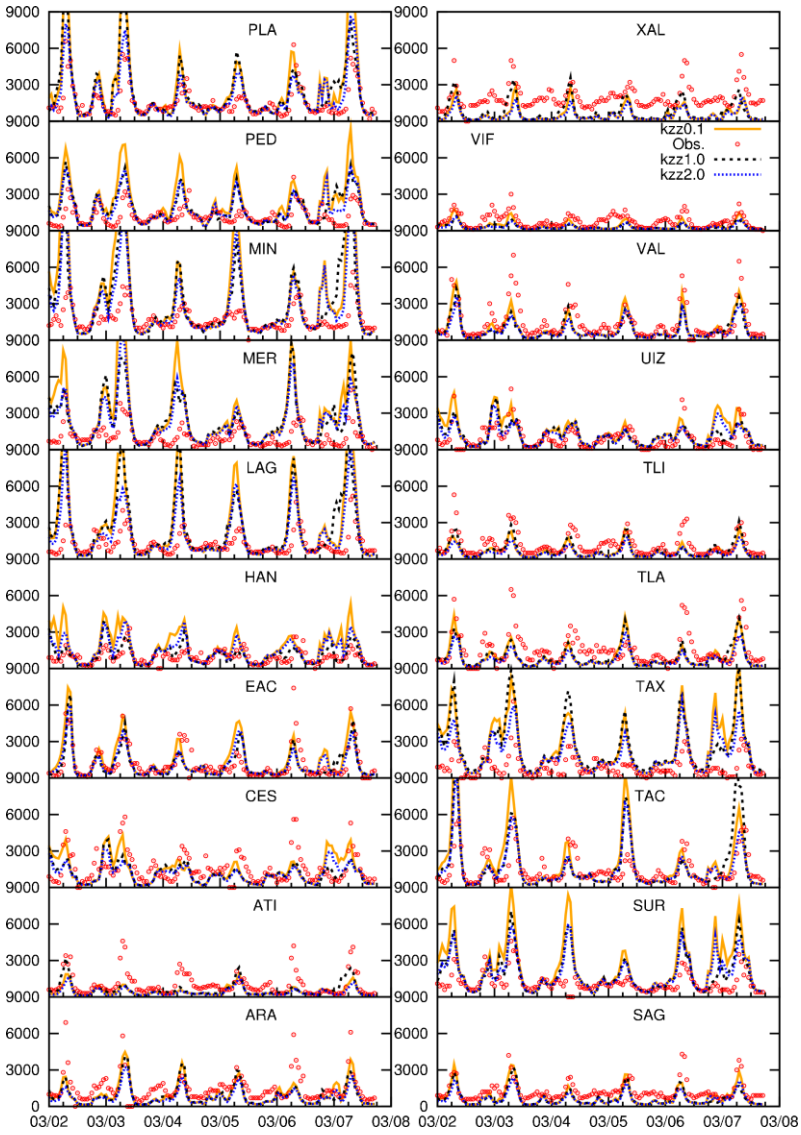

Figure 24 Sensitivity analysis of CO using k_{zz} at 0.1, 1.0, and 2.0. All units are in ppb.

Figure 25 shows the comparison of SO_2 observation with the k_{zz} cases. The k_{zz} cases are not significantly unique. The 1.0 case is still showing high concentrations with the 0.1 case having smaller peaks at ATI, LLA, TLA, TLI, and VIF. More importantly,

the SO_2 peak of March 4 is still not that well captured by the k_{zz} cases indicating that the missing SO_2 on that day is not likely caused by improper vertical mixing.

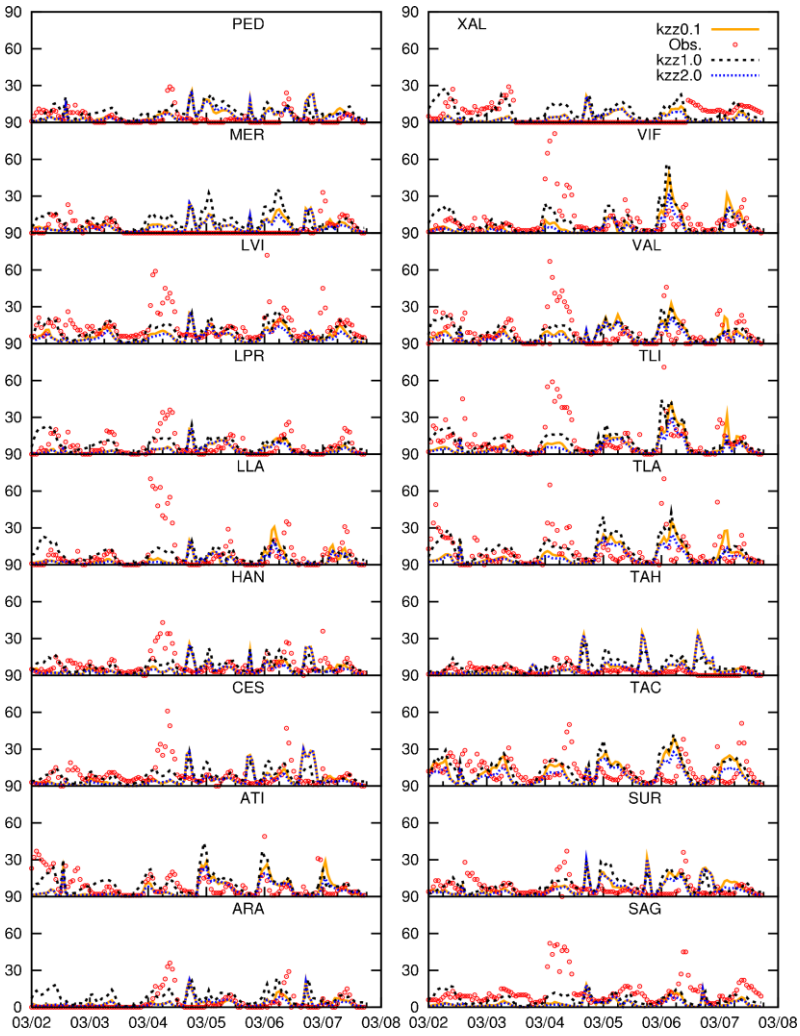

Figure 25 Sensitivity analysis of SO_2 using k_{zz} at 0.1, 1.0, and 2.0. All units are in ppb.

Figure 26 shows the PM_{10} observations compared against the k_{zz} cases. Overall, the three cases follow the same trends as those in the PM_{10} time series comparison plot. However, for the monitoring stations CES, EAC, PED, SAG, TAH, TLA, and VIF, the k_{zz} cases of 0.1 and 2.0 have both surpassed the 1.0 case. This is especially the case for

March 5, 6, and 7 during which very high PM_{10} concentrations were observed. In this instance, the sensitivity analysis has managed to scale concentrations to match some of the observation peaks.

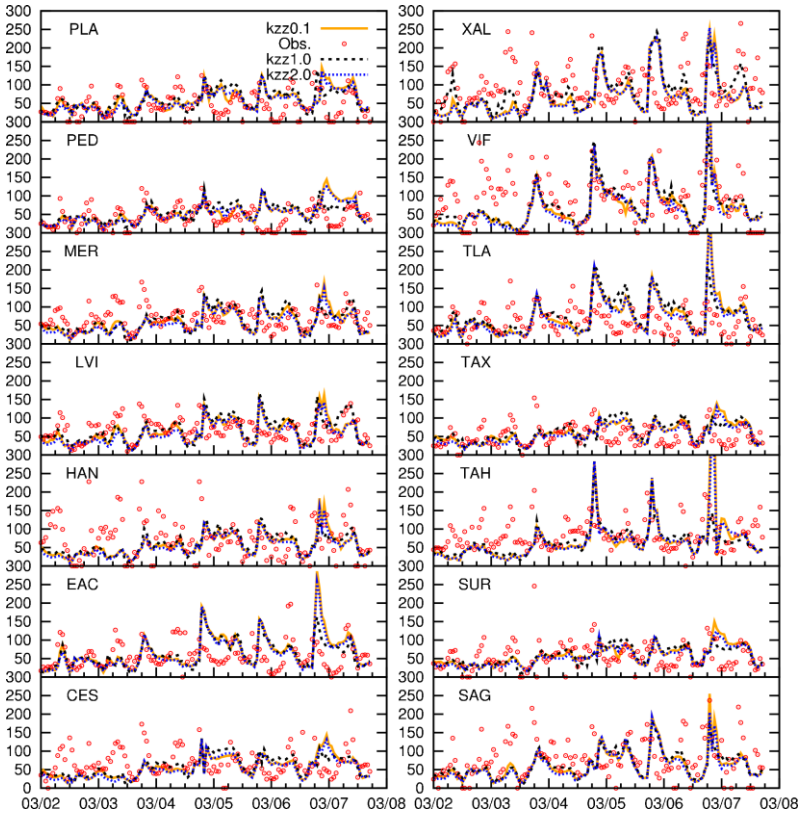

Figure 26 Sensitivity analysis of PM_{10} using k_{zz} at 0.1, 1.0, and 2.0. All units are in $\mu g/m^3$.

Figure 27 shows the observations of $PM_{2.5}$ compared with the three k_{zz} cases. With the exception of SAG, the 2.0 case was the closest to match observation numbers at all the monitoring stations. That is more often the case CAM, COY, and UIZ where the 0.1 and 1.0 case both are over predicting.

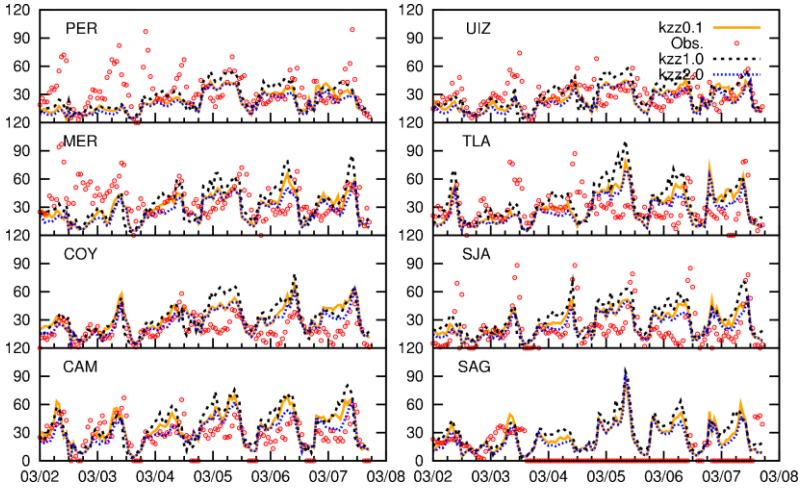

Figure 27 Sensitivity analysis of $PM_{2.5}$ using k_{zz} at 0.1, 1.0, and 2.0. All units are in $\mu g/m^3$.

To summarize, the k_{zz} sensitivity analysis was meant to scale concentrations to better match observations. Physically, lower k_{zz} value restricts the vertical mixing to near surface levels leading to greater pollutant levels near the surface. A higher k_{zz} value, in turn, should promote vertical mixing at greater altitudes resulting in a spread out pollutant plume and lower concentrations near the surface. However, this analysis only applies for primary pollutants whose emission sources are near surface. Secondary pollutants such as O_3 and secondary particulate matter are formed in the atmosphere from primary precursors during photochemical reactions. These reactions are highly non-linear that do not show a simple trend as k_{zz} varies.

3.4 Regional Distributions

For the regional distribution plot, hourly spatial concentrations for the entire modeling episode were lumped and averaged for a single plot showing selected species in the CMAQ model domain. Both the base case and the GEOS-Chem case have been shown and discussed.

3.4.1 Regional Distribution of Gas Phase Species

Figure 28 is the base case regional distribution plot showing O_3, NO_x, CO, and SO_2. Similarly, Figure 29 shows the same species for the GEOS-Chem case.

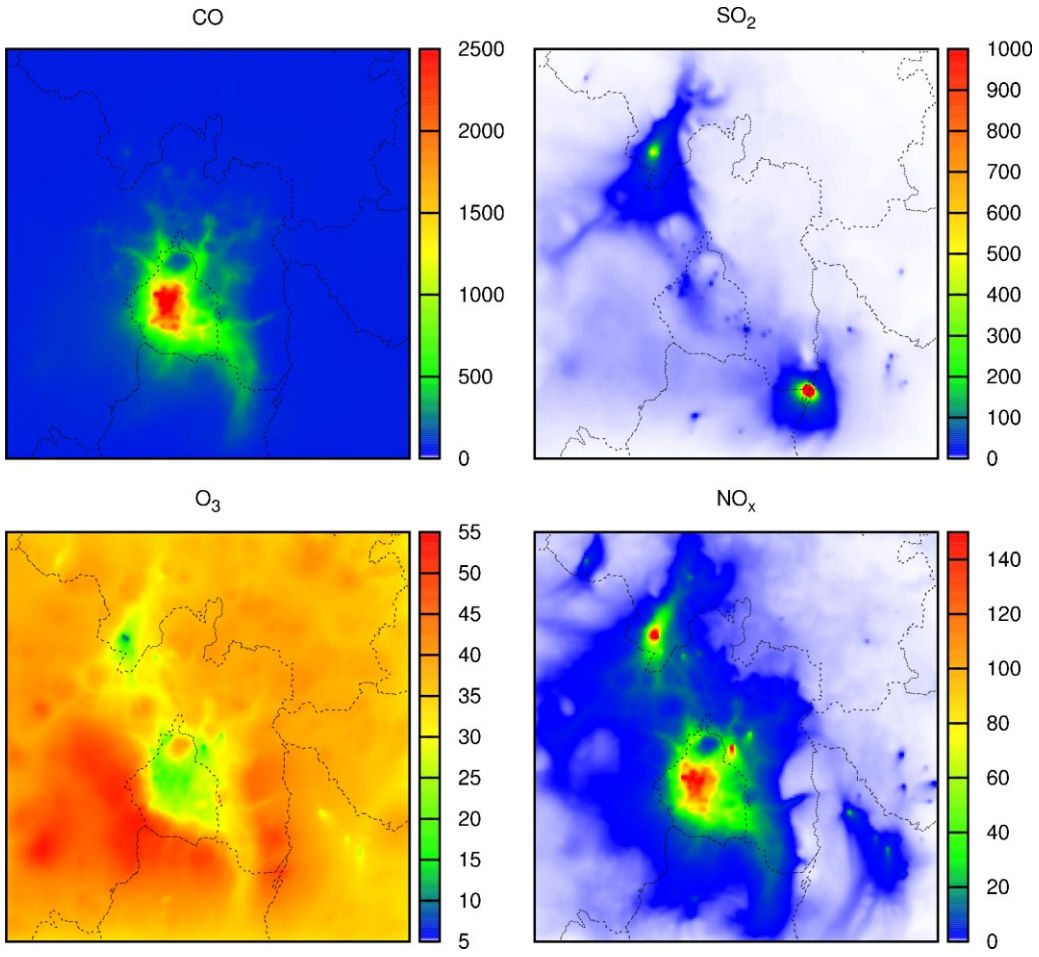

Figure 28 Regional distributions of O_3, NO_x, CO, and SO_2 for the base case simulation. All units are in ppb. O_3 is shown as an eight-hour average plot.

For both cases the O_3 distribution is quite similar with the 8-hour average concentration in the MCMA is at around 20 ppb. The biggest difference in O_3 concentration occurs near the north boundary where the GEOS-Chem results are slightly lower. For NO_x, both cases predict average concentrations over 100 ppb at both the

MCMA and the Tula site. The GEOS-Chem simulation shows more NO_x near the boundary. Both cases also show similar distribution of CO in the CMAQ model domain with average concentration in the MCMA of over 2.0 ppm. As for SO_2 distribution, both cases identify the two major sources of emissions outside the MCMA. Only the GEOS-Chem case presents greater ambient concentration in the other regions of the CMAQ model domain. While both cases are quite similar, only the GEOS-Chem case shows more background concentration for certain species.

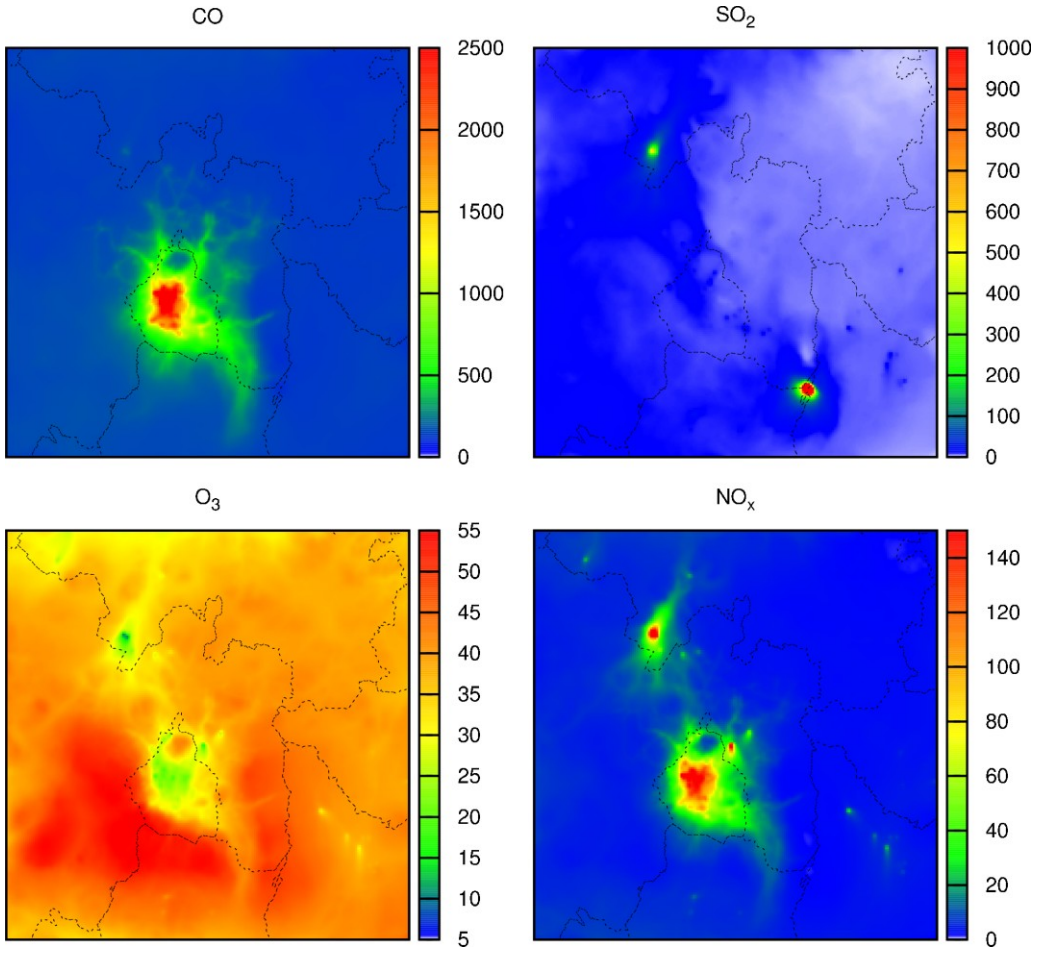

Figure 29 Regional distributions of O_3, NO_x, CO, and SO_2 for the GEOS-Chem case simulation. All units are in ppb. O_3 is shown as an eight-hour average plot.

3.4.2 Regional Distribution of SOA from Precursor Species

Once again, predicted hourly concentrations during the modeling episode were averaged to get the regional distribution of each species. Along with SOA, chemical components that make up SOA will also be shown and discussed for the base case and GEOS-Chem simulation.

Table 9 gives an overview of the SOA species and how CMAQ defines them. Total SOA is the sum of these component species (not including POA).

Table 9 List of precursor species and their composition as defined by CMAQ.

CMAQ SPECIES	SPECIES COMPOSITION	NOTES
[POA]	[AORGPAJ]+[AORGPAI]	Primary Organic Aerosol
[AALK]	[AALKJ]	SOA from Alkanes
[AXYL]	[AXYL1J]+[AXYL2J]+[AXYL3J]	SOA from low-yield Aromatics
[ATOL]	[ATOL1J]+[ATOL2J]+[ATOL3J]	SOA from high-yield Aromatics
[ABNZ]	[ABNZIJ]+[ABNZ2J]+[ABNZ3J]	SOA from Benzene
[ATRP1]	[ATRP1J]+[ATRP2J]	SOA from Monoterpenes
[AISOP]	[AISO1J]+[AISO2J]+[AISO3J]	SOA from Isoprene
[ASESQ]	[ASQTJ]	SOA from Sesquiterpene
[AOLGA]	[AOLGAJ]	Oligomers from anthropogenic SOA
[AOLGB]	[AOLGBJ]	Oligomers from biogenic SOA
[SOA1]	[AXYL3J]+[ABNZ3J]+[ATOL3J]+[AISO3J]	Non-volatile SOA

Figure 30 shows the regional distribution of SOA components in the base case run. Figure 31 shows those regional distributions in the GEOS-Chem case. Total SOA predicted by the base case is higher near the boundary than that compared by the GEOS-Chem case. The higher distribution near the boundary also occurs for SOA1, AALK,

AXYL, ATOL, ASESQ, ATRP1, AOLGA, and POA. The base case predicts higher concentration in the MCMA for ABNZ (0.01 μg/m^3), AISOP (0.03 μg/m^3), and AOLGB (0.25 μg/m^3) in comparison with the GEOS-Chem case (0.006, 0.02, and 0.04 μg/m^3 respectively). In this case, the base case results are greater than those of GEOS-Chem case near the boundary because the GEOS-Chem derived BCON does not include aromatic compounds.

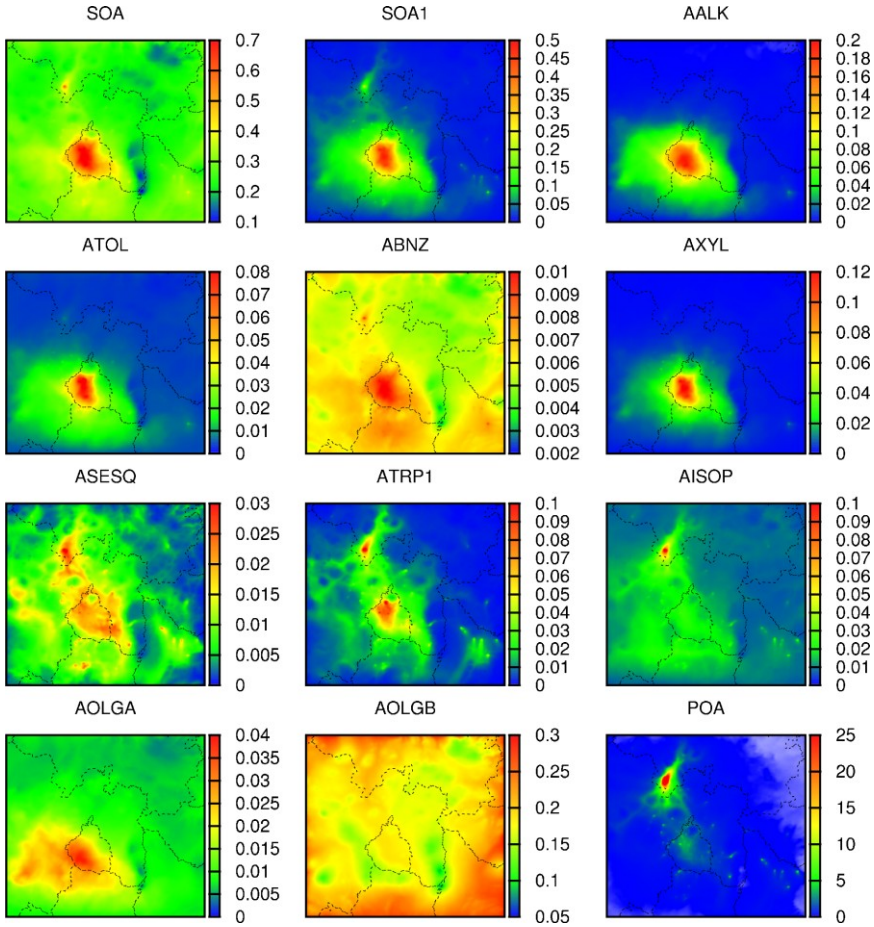

Figure 30 Regional distributions of SOA and its precursors for the base case simulation. All units are in μg/m^3.

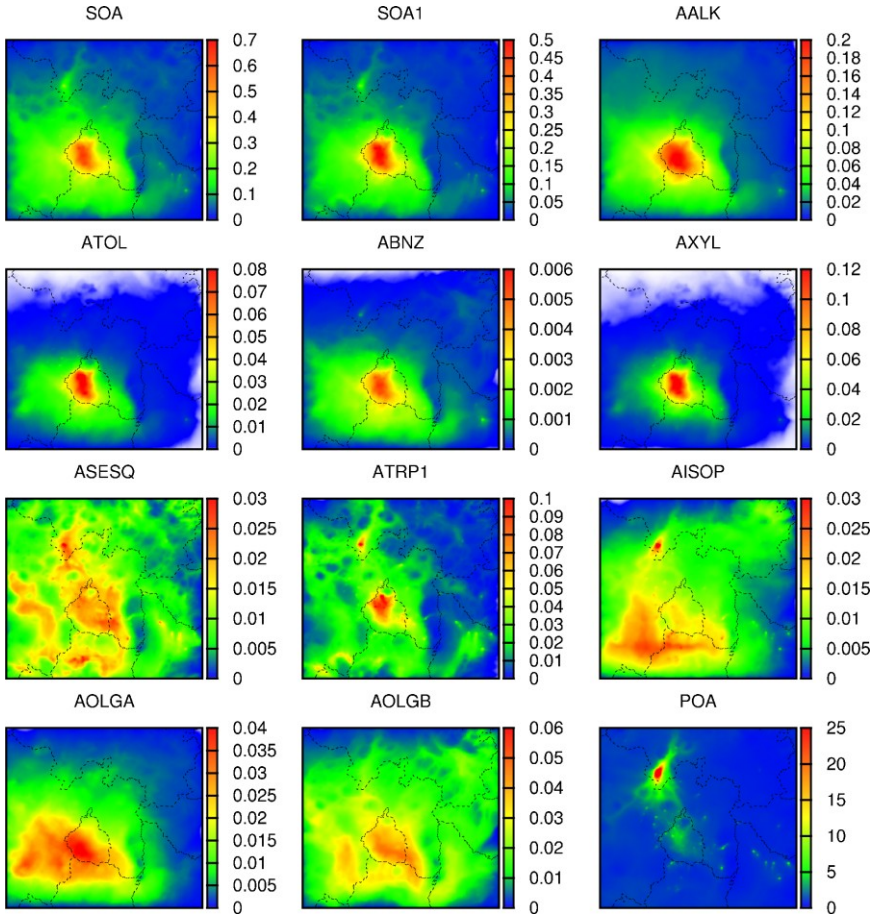

Figure 31 Regional distributions of SOA and its precursors for the GEOS-Chem case simulation. All units are in μg/m^3.

3.4.3 Semi-Volatile Organic Compounds in the MCMA

The concentrations of SOA are indirectly determined during the MILAGRO campaign using a tracer-based Chemical Mass Balance Method (CMB) and through analysis of the Aerosol Mass Spectrometer (AMS). The CMB analysis shows that the daily average SOA concentrations are on the order of 1-5 μg/m^3 (Stone et al., 2010; 2008) and the AMS OOA (oxygenated SOA, regarded as surrogate of SOA) concentrations can be as high as 30 μg/m^3 during day time peak SOA hours (Aiken et al., 2009). The predicted SOA concentrations are on the order of 0.5 μg/m^3, which is

approximately an order of magnitude lower than the derived SOA concentrations from these experiments. The under-prediction in the CMAQ model can be caused by missing precursor emissions or SOA formation pathways. It is also possible that temperature dependent SOA partitioning is not appropriately modeled. There are enough semi-volatile products produced through gas-phase oxidation processes, but the semi-volatile organic compounds (SVOC) are not partitioned to the particle phase.

In order to examine the total amount of SVOC, episode averaged regional distribution plots are generated for both base case and GEOS-Chem case. Figure 32 shows the regional distribution of SVOC species with the base case. Figure 33 shows them for the GEOS-Chem case.

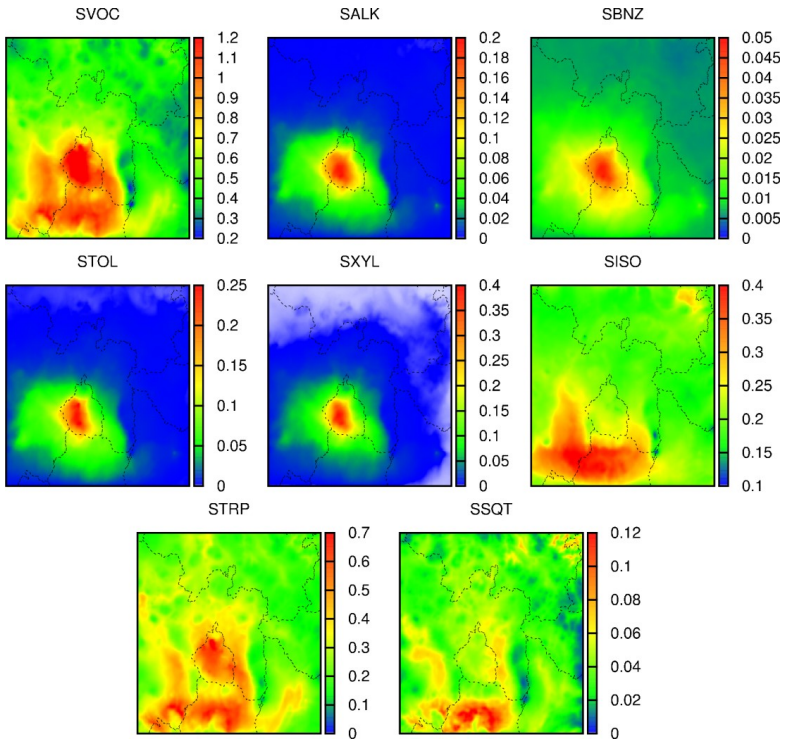

Figure 32 Regional distributions of SVOC species for the base case simulation. All units are in $\mu g/m^3$.

The first plot in both cases, SVOC, is the sum of SALK (SVOC from alkane), SBNZ (SVOC from benzene), SISO (SVOC from isoprene), SSQT (SVOC from sesquiterpene), STOL (SVOC from high-yield aromatics), STRP (SVOC from monoterpene), and SXYL (SVOC from low-yield aromatics).

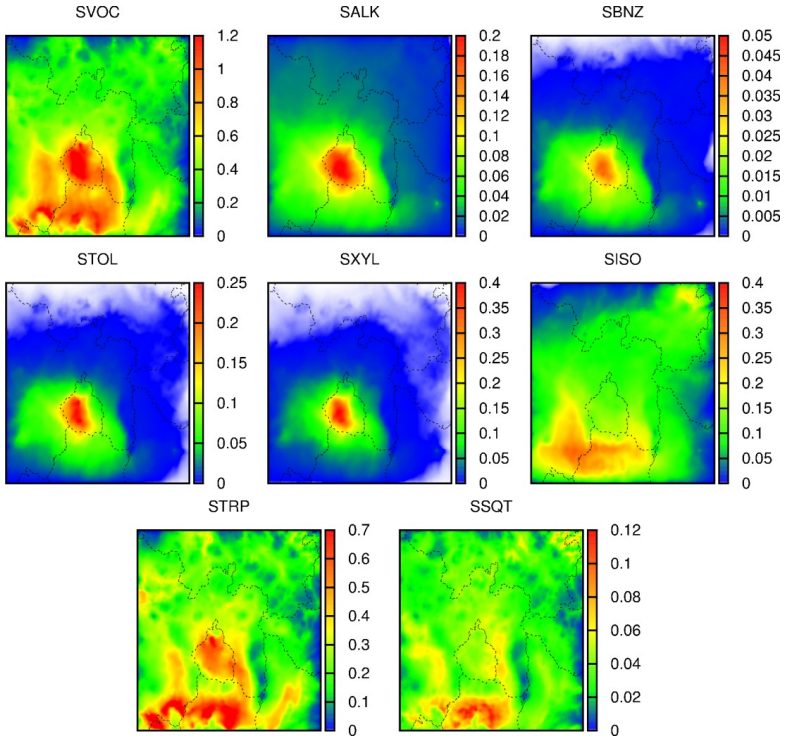

Figure 33 Regional distributions of SVOC species for the GEOS-Chem simulation. All units are in μg/m^3.

There are some differences and similarities in both cases. The base case shows higher ambient concentrations of SBNZ, SISO, STOL, and STRP than the GEOS-Chem case. Both cases also show near to the same levels of SSQT and SXYL in the CMAQ model domain. The GEOS-Chem case shows a higher concentration of SALK in the MCMA as well as the adjacent regions. Total SVOC is about the same (1.2 μg/m^3) in the

MCMA for both cases. The amount of SVOC is approximately a factor of two than the predicted SOA. However, even if all the SVOCs are partitioned into the particle phase, the predicted SOA concentrations are still significantly lower than those observed (Dzepina et al., 2009). Thus, it is very likely that emissions of SOA precursors or problems in the current CMAQ SOA mechanism cause the SOA production.

3.4.4 Breakdown of PM Species in the MCMA

Total PM (10 and 2.5 μm), coarse PM ($PM_C = PM_{10} - PM_{2.5}$) and individual PM species concentrations have been averaged for the modeling episode to produce regional distribution plots in the CMAQ model domain. The plot sets of the base case run and the GEOS-Chem case run will be compared and discussed.

Figure 34 shows the regional distribution of total PM species PM_{10}, PM_C (coarse PM), and $PM_{2.5}$ for the base case set. Figure 35 shows the regional distribution for the GEOS-Chem case set.

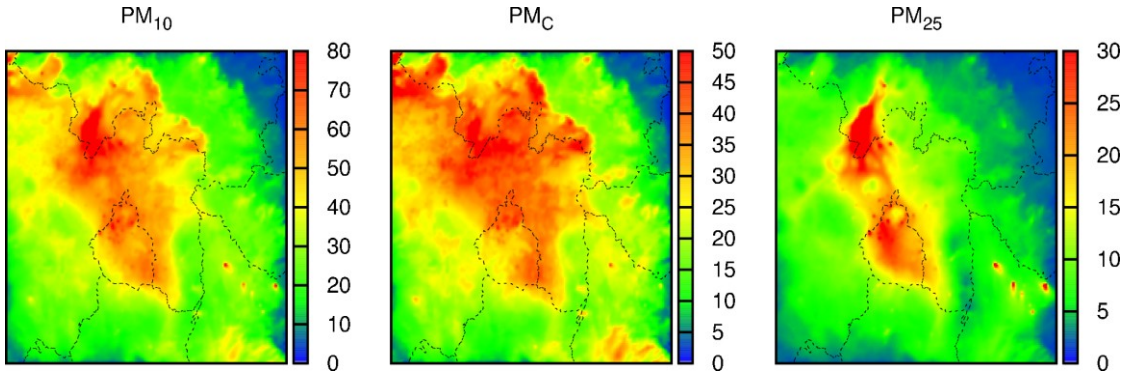

Figure 34 Regional distributions of PM_{10}, PM_C, and $PM_{2.5}$ for the base case simulation. All units are in $\mu g/m^3$.

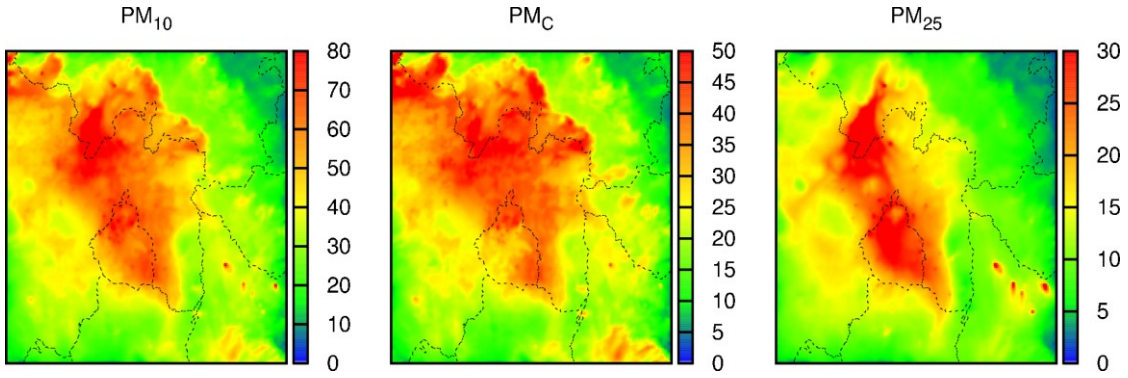

Figure 35 Regional distributions of PM_{10}, PM_C, and $PM_{2.5}$ for the GEOS-Chem case simulation. All units are in $\mu g/m^3$.

Both cases have the regional distribution within a reasonable range of each other. The GEOS-Chem case exhibits a higher PM concentration in and around the MCMA. The specific differences shall be made clear in the next part where PM_{10} and $PM_{2.5}$ species will be individually broken down to its components.

Figure 36 shows the regional distribution of PM_C components for the base case run. Figure 37 shows the regional distribution for the GEOS-Chem case run. The GEOS-Chem case shows higher concentrations for sea salt (Na^+, Cl^-), ammonium (NH_4^+), nitrate (NO_3^-), and sulfate (SO_4^{2-}) species whereas the base case species concentrations are below 1 $\mu g/m^3$. The dust (OTHER) component is the most dominant of the species and the concentration predicted by the GEOS-Chem case and the base case are very similar, which suggests that the majority of the dust is generated locally by the windblown dust emission model.

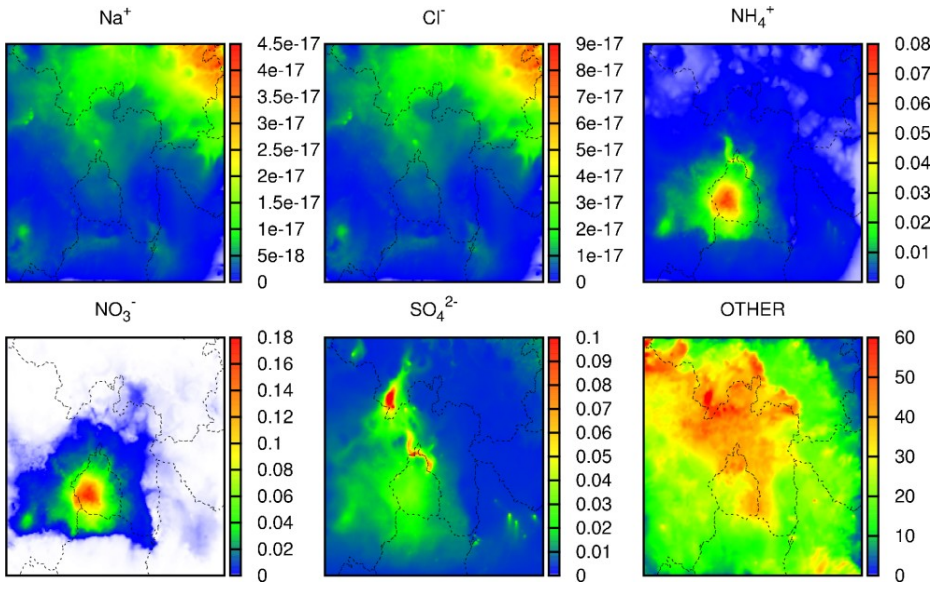

Figure 36 Regional distributions of PM_C species for the base case simulation. All units are in $\mu g/m^3$.

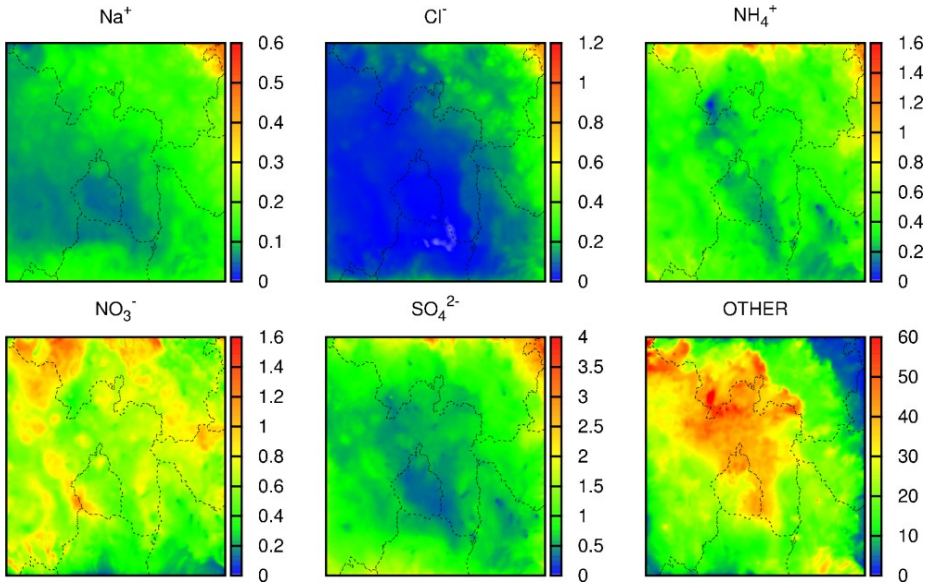

Figure 37 Regional distributions of PM_C species for the GEOS-Chem case simulation. All units are in $\mu g/m^3$.

Figure 38 shows the regional distribution of the individual $PM_{2.5}$ species for the base case run. Figure 39 shows the regional distribution for the GEOS-Chem case run.

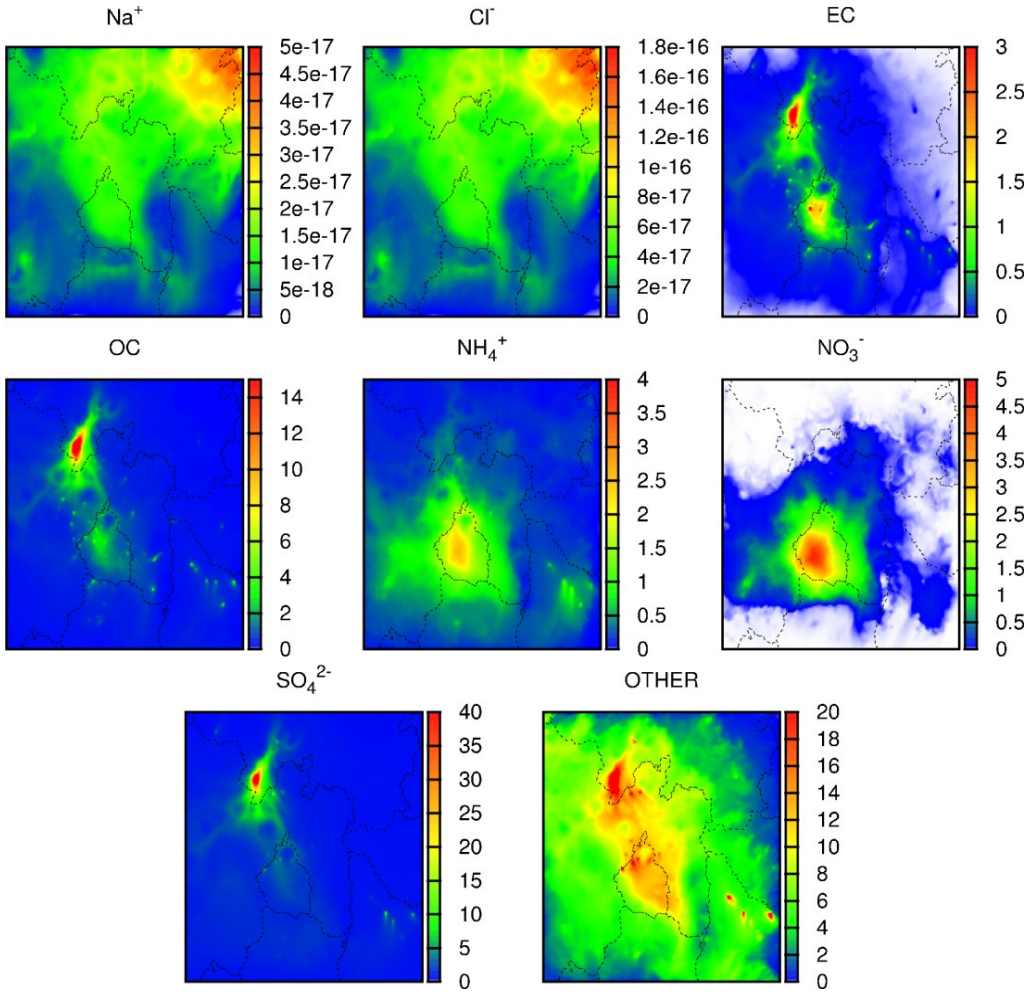

Figure 38 Regional distribution plot of $PM_{2.5}$ species for the base case simulation. All units are in $\mu g/m^3$.

In comparison with the base case concentrations, the GEOS-Chem case has produced slightly higher concentrations for sodium chloride (Na^+, Cl^-), EC/OC, ammonium (NH_4^+), nitrate (NO_3^-), and sulfate (SO_4^{2-}). The concentrations "OTHER" are similar for both cases. The higher concentrations predicted by the GEOS-Chem case is again due to higher boundary conditions. The GEOS-Chem results appear to be more realistic for NaCl, as it is expected that some amount of NaCl will exist in the atmosphere due to long range transport of sea salt particles.

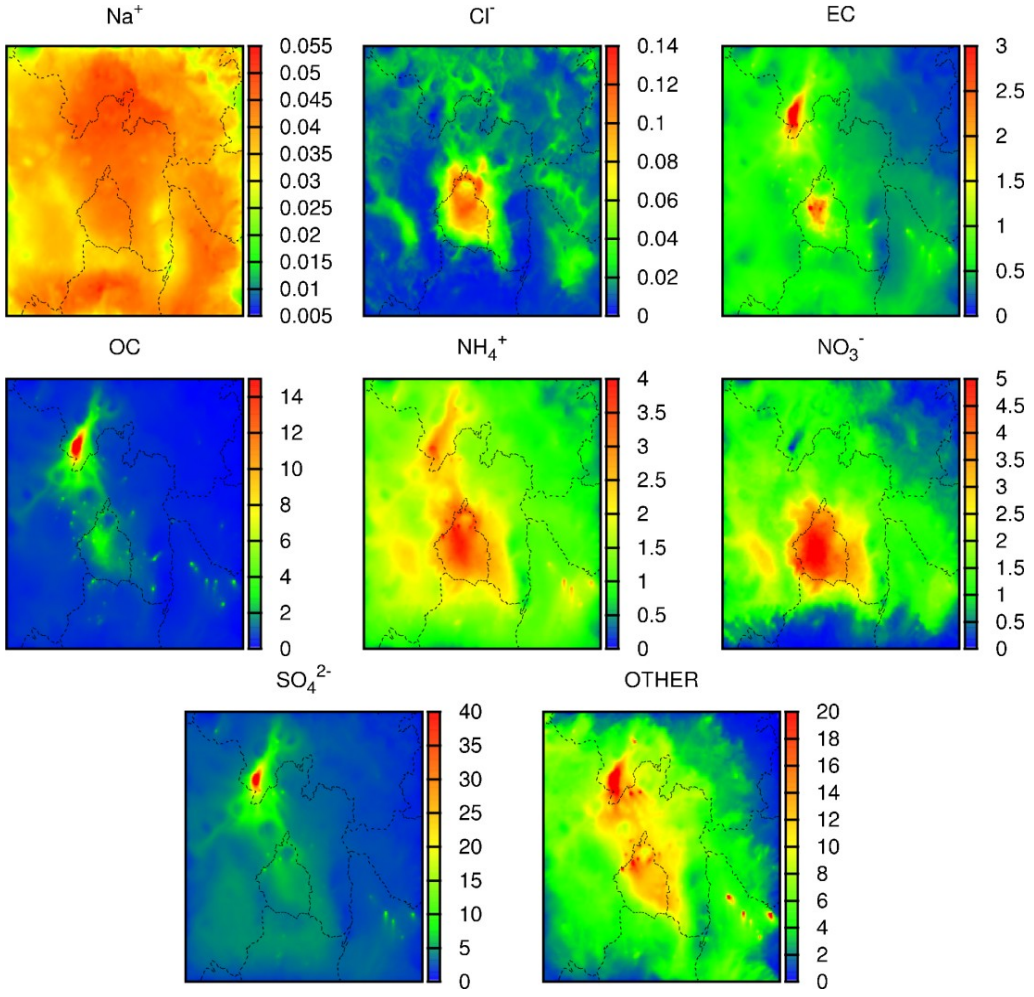

Figure 39 Regional distributions of $PM_{2.5}$ species for the GEOS-Chem case simulation. All units are in $\mu g/m^3$.

Species concentrations at some locations in the MCMA were examined for their contribution to total PM. One of the stations selected for PM was the La Merced (MER) monitoring station located in downtown Mexico City. MER is one of the few monitoring stations in the MCMA that saves both PM_{10} and $PM_{2.5}$ hourly concentrations.

Figure 40 compares $PM_{2.5}$ composition at MER for the base case and the GEOS-Chem case. The GEOS-Chem case shows higher contributions from sulfate, nitrate, and ammonium than the base case. The carbonaceous particles (EC + OC) account for 12-

13% of the $PM_{2.5}$ for both cases. The base case predicts a higher contribution of dust (marked as "PM25_OTHR") at MER than the GEOS-Chem case (60% to 44%). PM contribution at different locations in the MCMA has also been analyzed particularly for dust emissions from PM25_OTHR. The station CES, southeast, showed average dust contribution of 59% in the base case and 44% in the GEOS-Chem case to $PM_{2.5}$ mass. PED in the southwest showed 48% at base case and 39% at GEOS-Chem case. TLA in the northwest showed 60% at base case and 44% at GEOS-Chem case. In comparison to a study done by Vega et al. (2010), where the average dust contribution to the $PM_{2.5}$ mass was in the range of 8-16%, the CMAQ predictions are generally higher. This may be attributed to the over-estimation of dust in CMAQ.

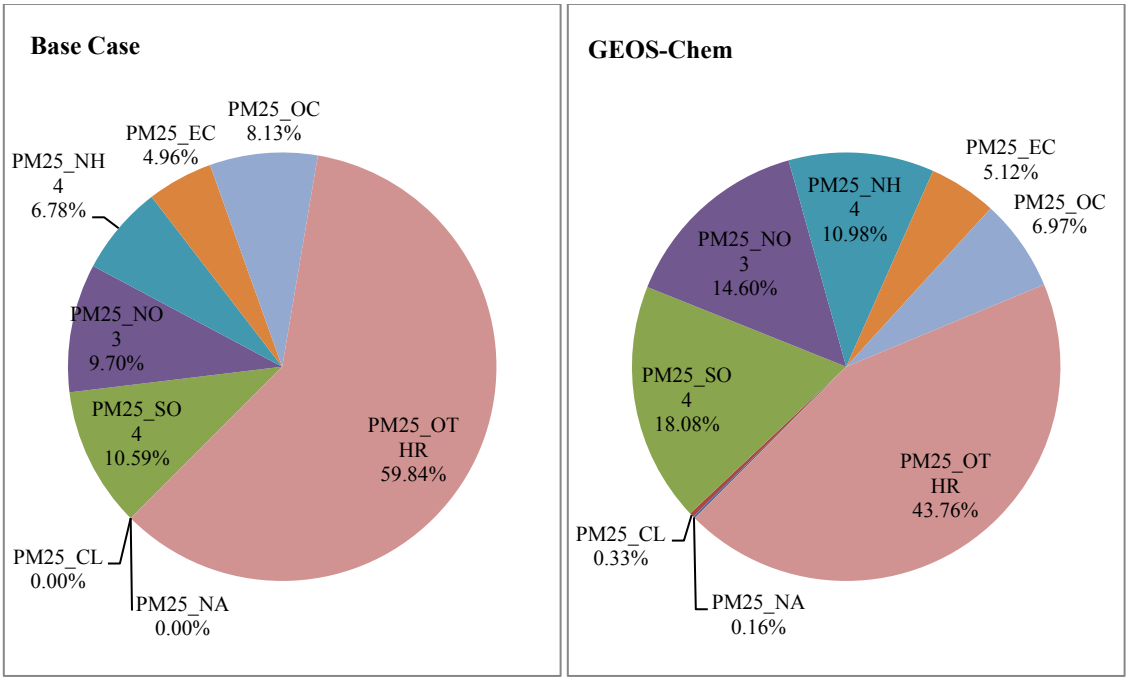

Figure 40 Contribution of $PM_{2.5}$ species at La Merced (MER) monitoring station for the base case and GEOS-Chem case.

Figure 41 shows the total PM composition (PM_{10} = PM_C + $PM_{2.5}$) at MER comparing the base case and GEOS-Chem case. Dust (labeled as PMC_OTHR) is also the dominant species for both cases. For the base case, the contribution of nitrate, sulfate, ammonium, and sea salt species to total PM are almost negligent (less than 1%).

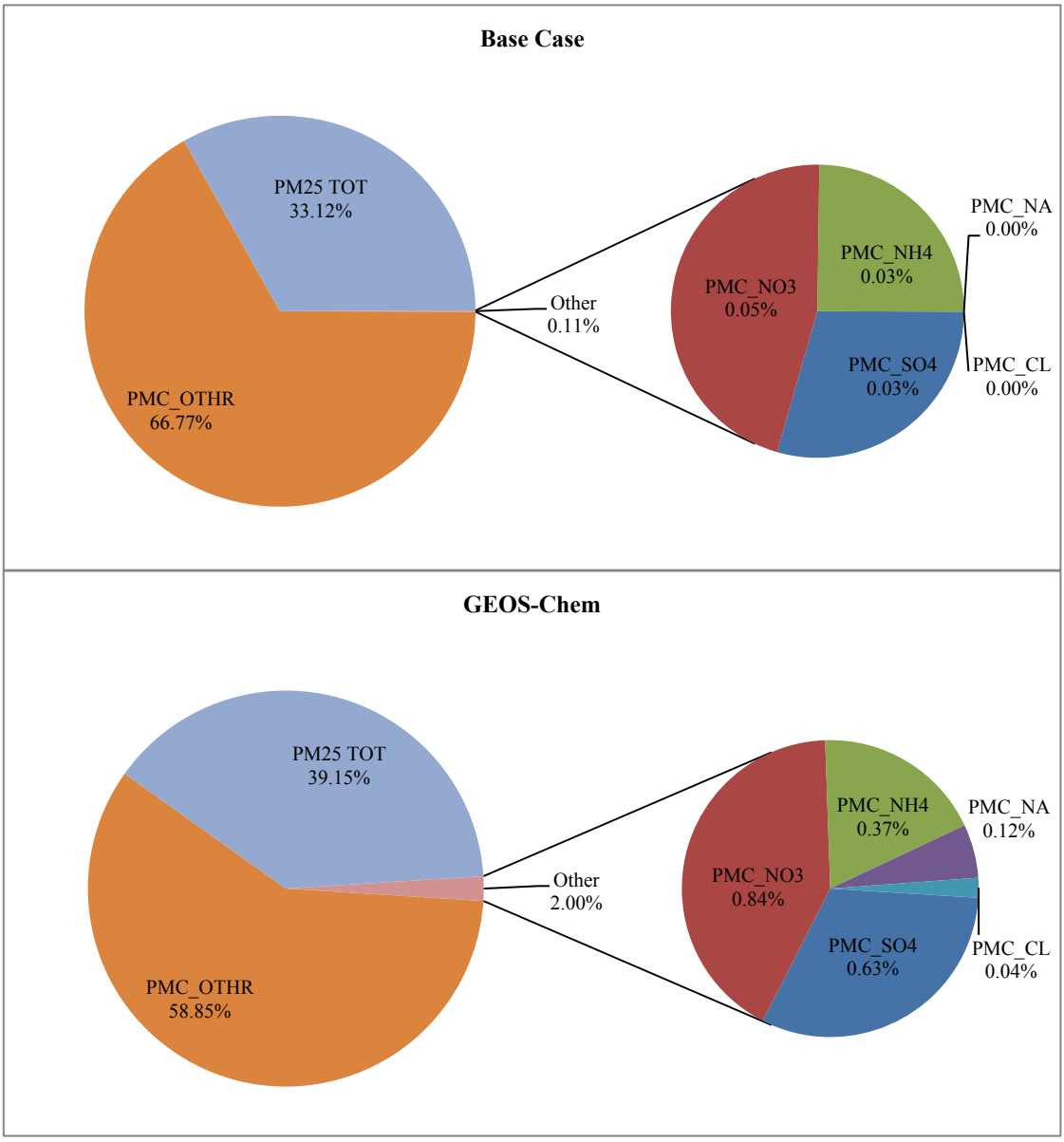

Figure 41 Contribution of total PM at La Merced (MER) monitoring station for the base case and GEOS-Chem case.

In comparison with previous studies done by Vega et al. (2001; 2002) and Chow et al. (2002) conducted during the 1997 IMADA-AVER campaign, the PM composition for this modeling episode have some differences. By mass, $PM_{2.5}$ makes up for 33% of total PM in the base case and 40% in the GEOS-Chem case while the previous studies report the mass composition of more than 50%. This may be due to the over-estimation of dust emissions in the CMAQ simulations.

3.5 Effects of Grid Resolution on the Predicted Concentrations

The motivation to perform fine horizontal resolution simulation in this project was to get accurate locations of potential emission sources in the MCMA and to better capture any flux in concentration gradients near existing emission sources. However, any studies comparing fine horizontal resolutions of up to 1 km to coarser resolutions are generally nonexistent. As another part of this project, CMAQ was simulated for the same modeling episode in the MCMA using the horizontal resolution of 3 km over a 70x70 domain. 3 km resolution predictions are compared with the 1 km resolution predictions to analyze behavior. Both predictions are from base case results.

Figure 42 shows the O_3 predictions comparing 1 km and 3 km results. The majority of the time series trends remain the same, and this especially the case for the daily peaks. In between the peak periods, more variations can be observed. Still, both cases remain the same for most part.

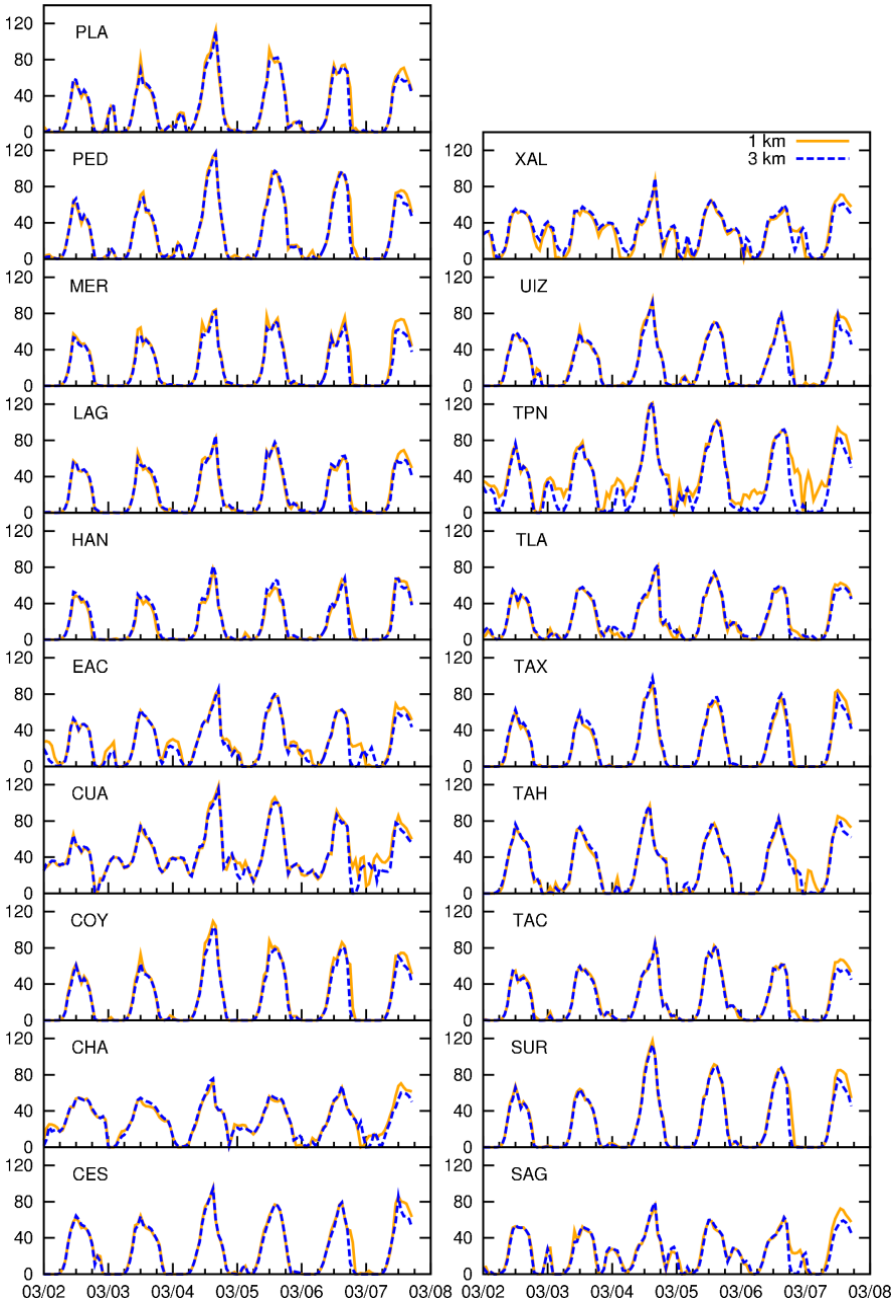

Figure 42 Comparison of O_3 concentrations for 1 km and 3 km CMAQ resolution.

Figure 43 shows the NO_x predictions comparing 1 km and 3 km results. The 1 km case shows higher peaks than the 3 km case for some monitoring stations (LAG, PLA, TAC, TLI, and XAL).

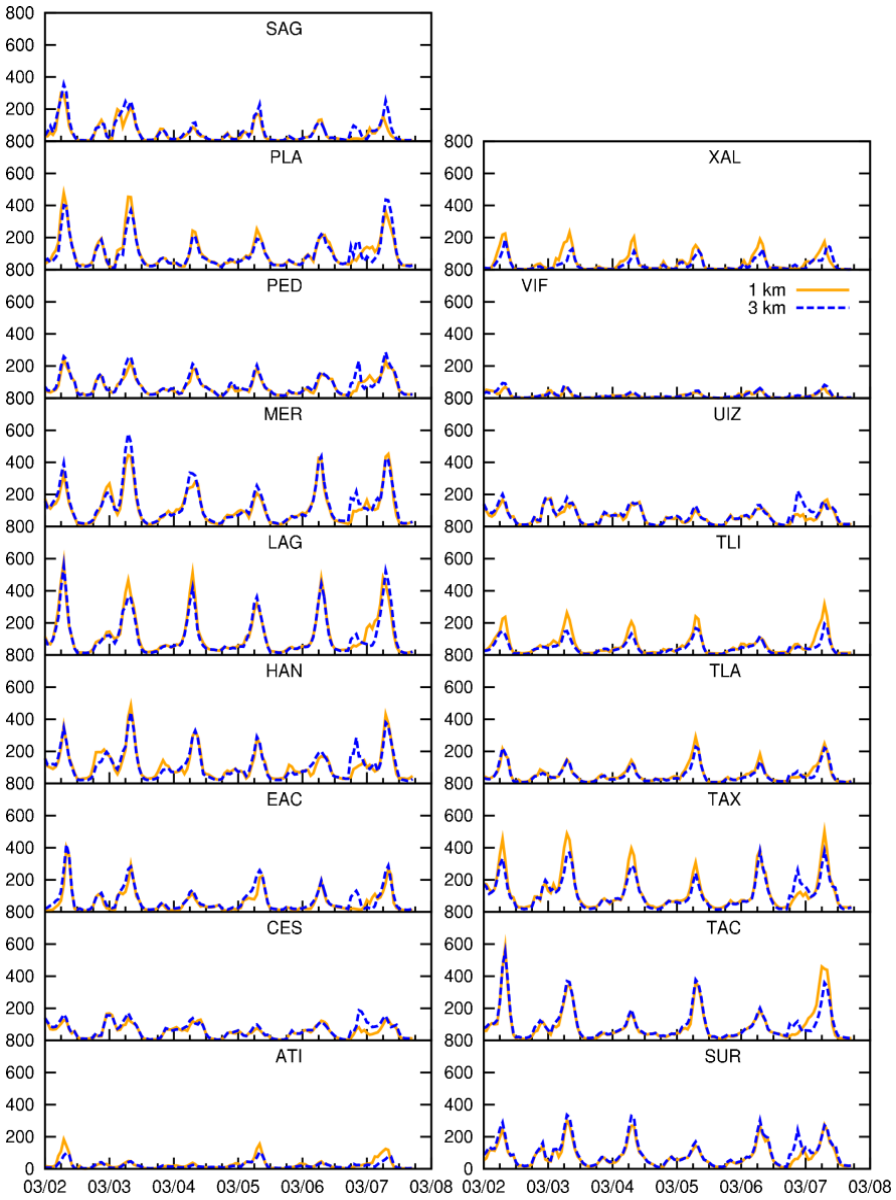

Figure 43 Comparison of NO_x concentrations for 1 km and 3 km CMAQ resolution.

Figure 44 shows the CO predictions comparing 1 km and 3 km results. Similar to NO_x, the CO 1 km predictions are higher than 3 km predictions for most of the monitoring stations. The higher peaks of 1 km predictions may be an indicator of refined concentration gradients near emission sources.

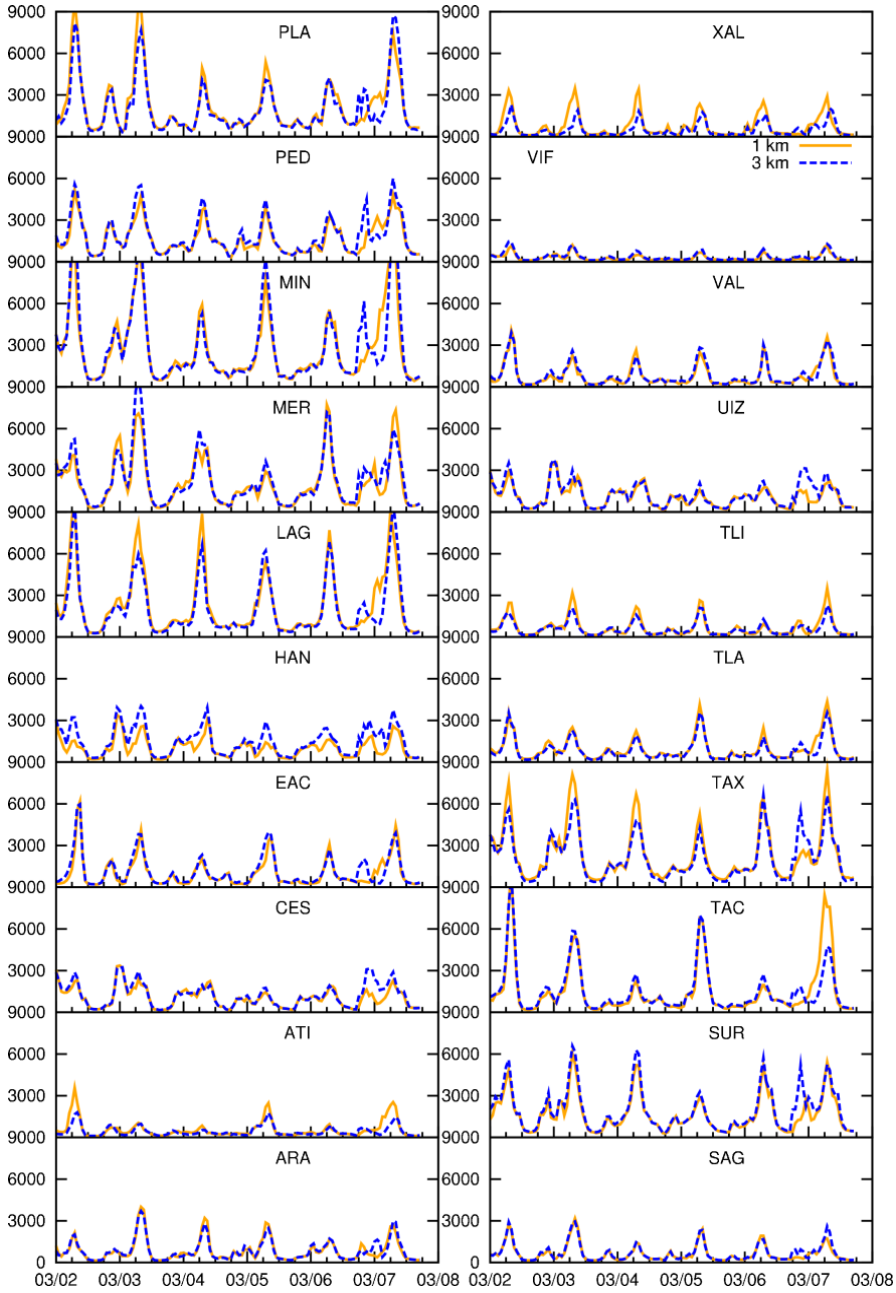

Figure 44 Comparison of CO concentrations for 1 km and 3 km CMAQ resolution.

Figure 45 shows the SO_2 predictions comparing 1 km and 3 km results. The 1 km predictions are generally higher for most of the monitoring stations showing the better capability of the high resolution model in resolving the spatial gradient of pollutants.

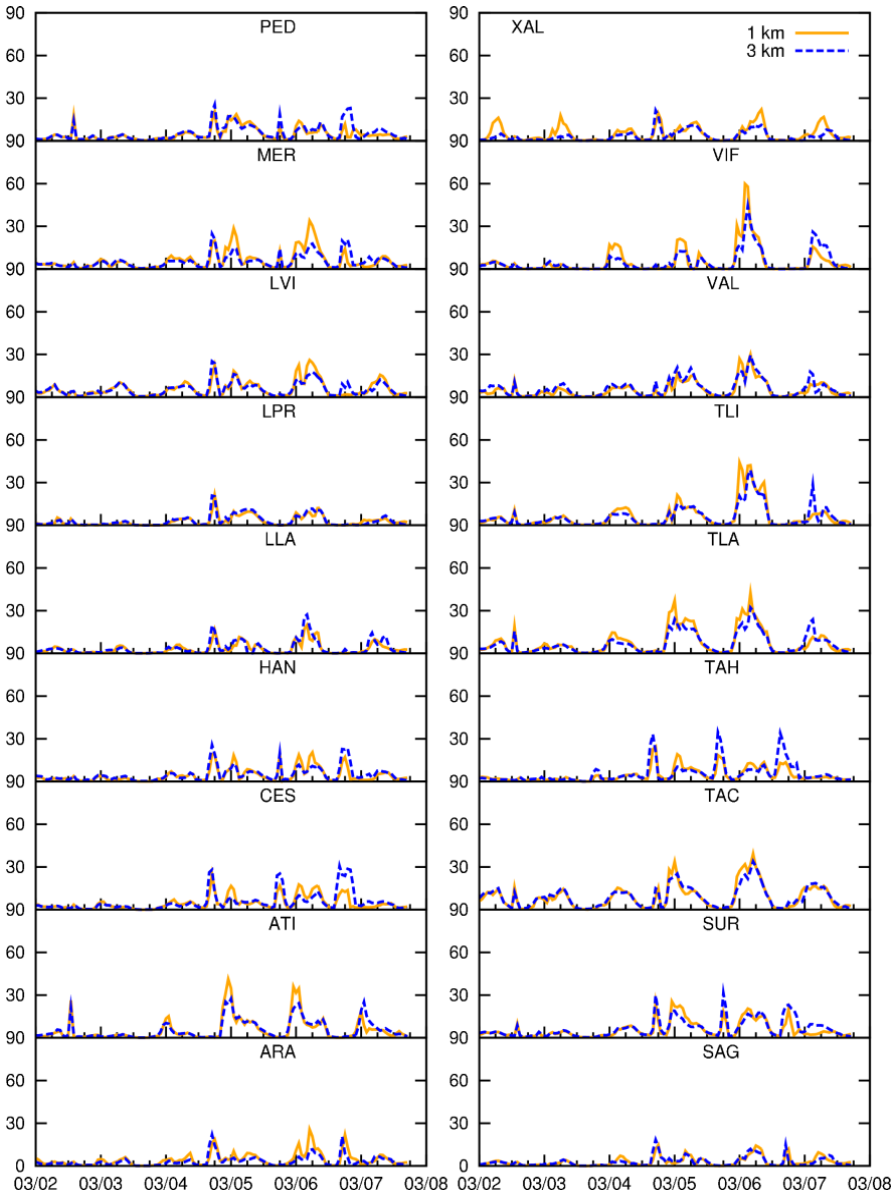

Figure 45 Comparison of SO_2 concentrations for 1 km and 3 km CMAQ resolution.

Figure 46 shows the PM_{10} predictions comparing 1 km and 3 km results. The prediction values for both cases remain the same for most of the modeling period. The 3 km predictions are shown to be higher for most of the monitoring stations on March 7, 2006. This may likely be from the affect of nearby emission sources in the 3 km

resolution that have higher concentrations. The same emission sources would be much further away in terms of grid cells to affect levels at that monitoring station.

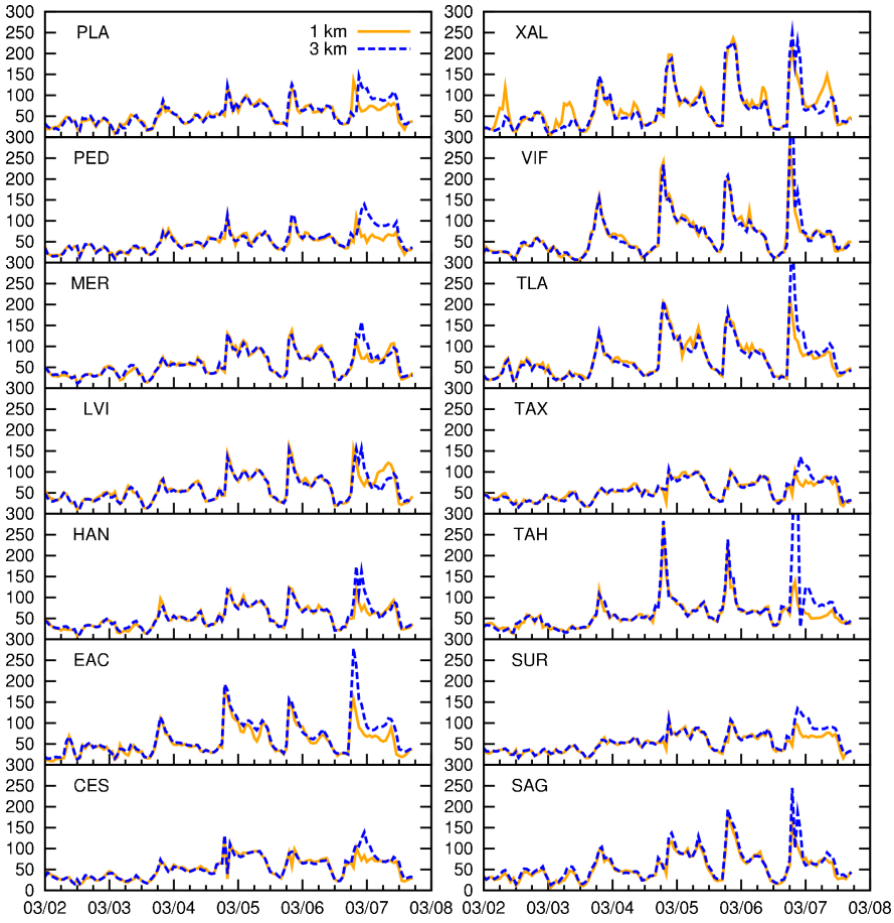

Figure 46 Comparison of PM_{10} concentrations for 1 km and 3 km CMAQ resolution.

Figure 47 shows the $PM_{2.5}$ predictions comparing 1 km and 3 km results. The predictions for both cases vary for all of the monitoring stations indicating towards no specific trend whatsoever. As mentioned previously, the varying predictions may likely have been due to the horizontal grid resolution and the coverage of emission sources in the 1 km and 3 km resolution domains.

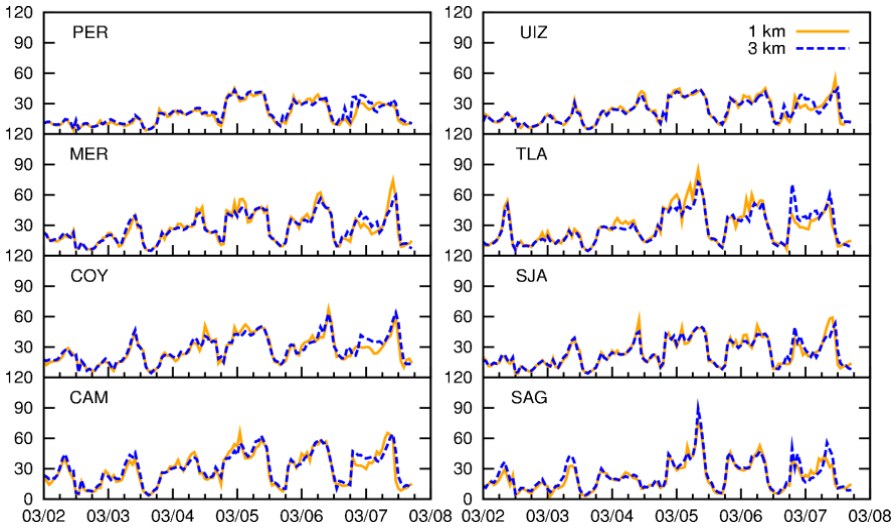

Figure 47 Comparison of $PM_{2.5}$ concentrations for 1 km and 3 km CMAQ resolution.

When compared with observations, the 3 km resolution predictions perform slightly better than that of 1 km resolution. Table 10 summarized the statistical analysis comparison of 1 km and 3 km values with observations using the same threshold values as used earlier in the section. The overall performance of CO is improved in the 3 km resolution in the context of matching the observation values while it remains almost similar for O_3, NO_x, PM_{10}, and $PM_{2.5}$.

Table 10 Comparison of statistical performance parameters between 1 km and 3 km resolution.

SPECIES	1 km		3 km		POINTS
	MFB	MFE	MFB	MFE	
O_3	-0.18	0.23	-0.19	0.23	435
NO_x	-0.22	0.56	-0.21	0.56	544
CO	-0.78	0.96	-0.26	0.59	468
PM_{10}	-0.26	0.53	-0.23	0.53	1741
PM_{25}	-0.21	0.54	-0.17	0.52	963

3.6 Back Trajectory Analysis with HYSPLIT

de Foy et al., (2007) concluded that two prominent sources of SO_2 emission outside of MCMA could contribute significantly to SO_2 concentrations in MCMA: the Tula industrial complex in the northwest and the Popocatépetl volcano in the southeast. However, emissions from the Tula region were based on 2003 remote sensing information. The performance of the MM5 simulation used in that study has not been validated. In this project, the most recent emissions for 2006 based on actual reported fuel consumptions, along with a fully evaluated WRF meteorology simulation, are used to study the influence of the SO_2 emissions from the Tula region (TUL) and the Popocatépetl volcano (POP) on SO_2 concentrations in the MCMA.

3.6.1 Model Description

To verify the sources regions of SO_2, 24-hour back trajectories were calculated with the HYbrid Single-Particle Lagrangian Integrated Trajectory (HYSPLIT) model developed at NOAA Air Resource Laboratory. The HYSPLIT (HYbrid Single-Particle Lagrangian Integrated Trajectory) model is capable of computing particle trajectories as well as dispersion and deposition simulations for the given meteorological conditions (Draxler and Hess, 1997, 1998). The transport of a pollutant across the meteorological grid can be calculated either with puff or particle approach that tracks the path and growth of the trajectory.

For the purpose of this project, HYSPLIT v4.9 is used to perform back trajectories during peak SO_2 concentration periods to determine their potential sources at receptor sites. The meteorological data came from the MCIP files that were used to run

the MCMA simulations in CMAQ. MCIP2ARL, an intermediate program distributed as an auxiliary program written with CMAQ, converts the MCIP files to generate a packed-binary ARL format file to be used in HYSPLIT as initial input.

Figure 48 shows the input files needed by the MCIP2ARL program to generate HYSPLIT-compatible files. The files are composed of direct-access records written ARL packed data format. Each record consists of a header describing the meteorological parameter stored followed by the data packed by the difference in value to previous point. Once the files were generated, 24-hour trajectories for every hour were run for March 2-7, 2006. The starting points of the back trajectories were located at the SO_2 monitoring stations.

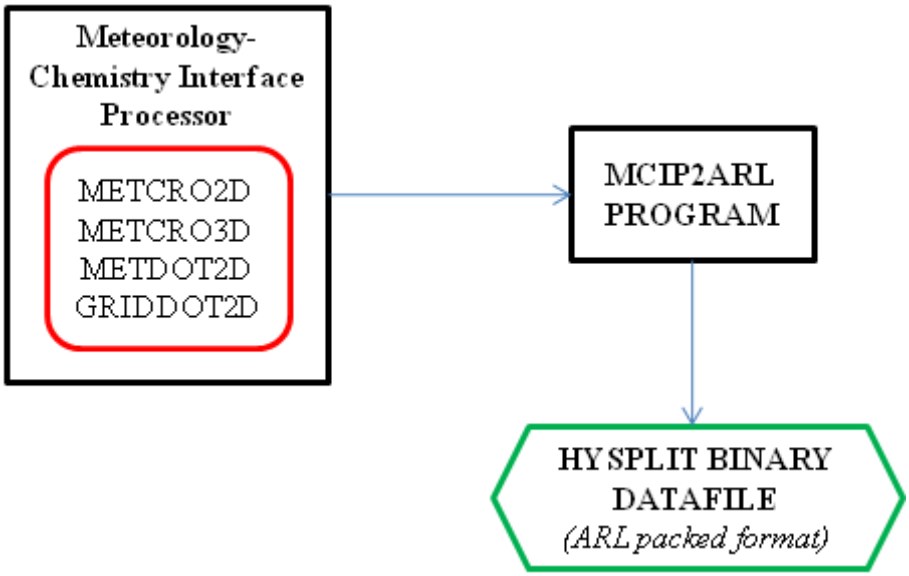

Figure 48 Processing methodology of the MCIP2ARL program.

3.6.2 Back Trajectory

19 SO_2 monitoring stations were used as starting points for the back trajectory analysis so as to ascertain the transport path taken by the pollutant. Back trajectories have been calculated using six different settings for vertical motion methods. By default, HYSPLIT uses the predicted velocity by the meteorological model (0-W_{pred}). The other options allow the vertical motion of the air parcels to follow constant temperature (1-isentropic), constant pressure (2-isobaric), constant density (3-isopycnic), and constant internal sigma coordinates (4-isosigma). It is also possible to use recalculated vertical velocity in the HYSPLIT model based on velocity divergence (5-divergence).

Figure 49 shows a cumulative back-trajectory plot for March 4, 2006 using the default vertical calculation option 0-W_{pred}. The frequency plots sums up individual back trajectories at all monitoring stations and presents them as an episode plot. In this case, the frequency plot shows a 24-hour episode. The starting height on all back trajectories is 10 m. While each monitoring station has 144 points for the trajectory episode, the plots have been scaled down to a lower value to properly show the transport path of SO_2 across the MCMA.

As mentioned earlier during the discussion of time series plot of SO_2, the March 4 episode is important because of the observed peaks on that day which were not appropriately captured by either the base case or the GEOS-Chem case. The back-trajectory plot shows that most of the pollutant plume had to be transported into the MCMA from the north and northeast. Another portion of the plume had to be carried to

the MCMA from the southeast. Some of the trajectories are shown to pass through the TUL area confirming the effects of their emissions on MCMA SO_2 concentration levels.

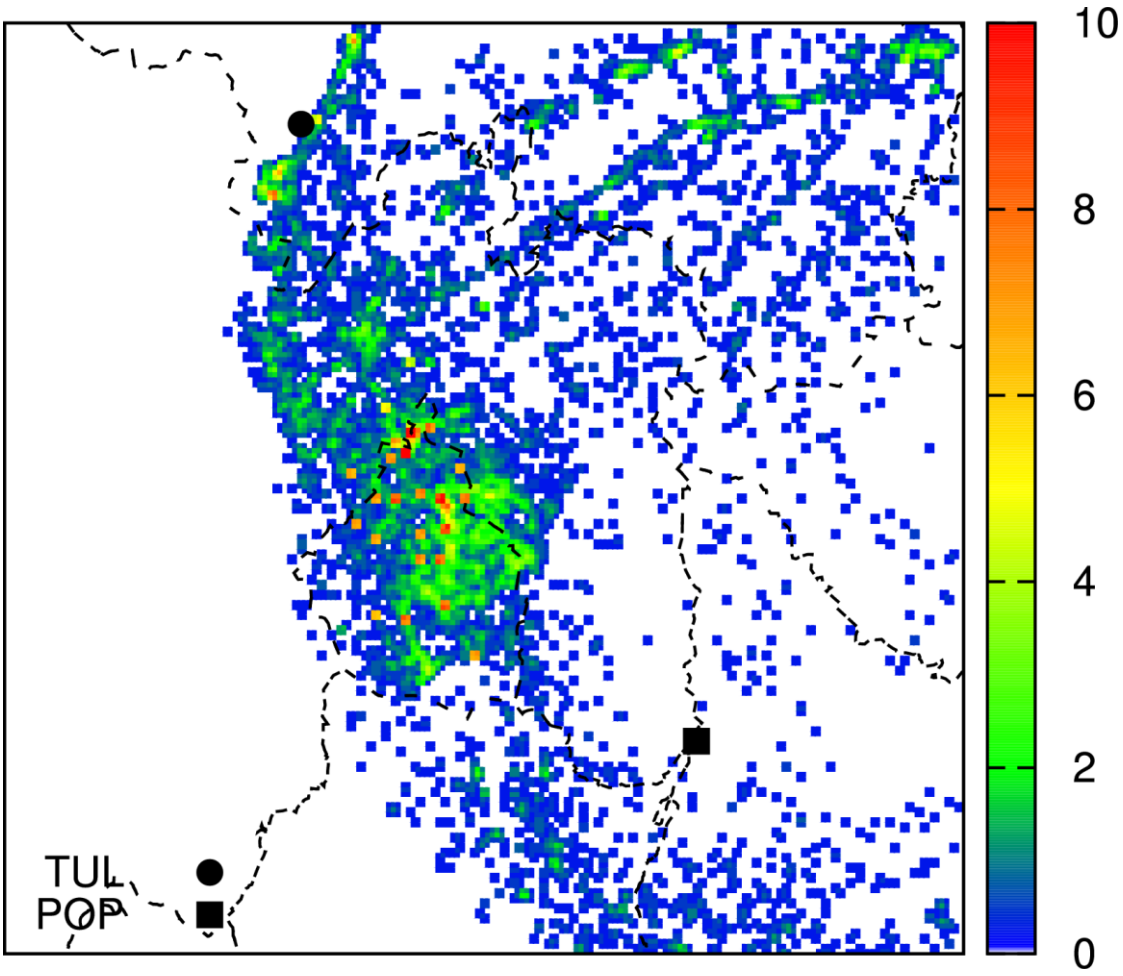

Figure 49 Frequency of all back trajectories in the MCMA for March 4, 2006. The range has been scaled to appropriately show the transport of the pollutant. Individual markers represent TUL (round) and POP (square).

Figure 50 shows the back trajectory plots using the six different vertical calculation methods. All back trajectories show a general transport of the particle from the northeastern direction towards the MCMA. A few trajectories are also shown to pass through TUL. Some trajectory transport is also shown to occur from the southeastern

gap close to POP where some trajectory points are located. Based on the method of vertical calculation, the spread of the trajectories across the MCMA are also affected.

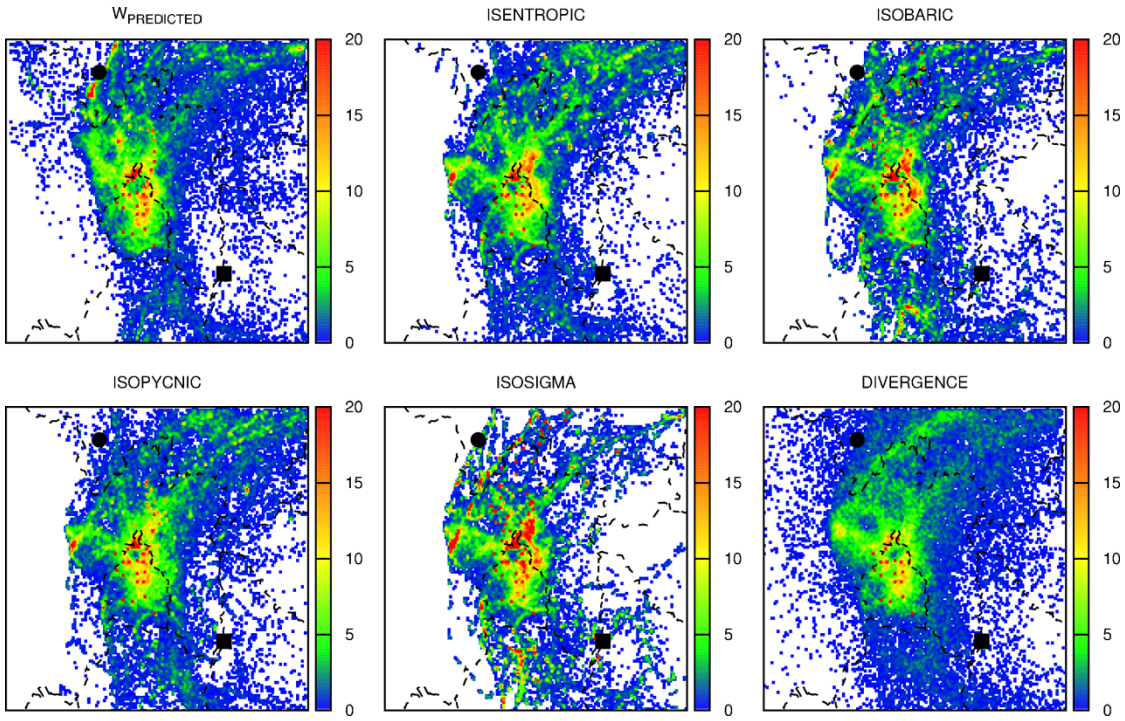

Figure 50 Frequency of all back trajectories in the MCMA for the period of March 2-7, 2006. The range has been scaled to appropriately show the transport of the pollutant. Individual markers represent TUL (round) and POP (square).

The HYSPLIT model, which is given the WRF-generated meteorology used in CMAQ, has reasonably shown where the SO_2 sources are located and the corridors where the air masses pass though and reach urban receptor locations in the MCMA. The spatial distributions of the trajectories indicate that the contributions from POP and TUL on the SO_2 concentrations in the MCMA should be considered. However, trajectory analysis for a longer period over a larger domain calculating shorter intervals (every 10 to 15 minutes) should provide more confidence in the performance of HYSPLIT.

4. CONCLUSIONS

CMAQ was used to predict air pollutant concentrations in the MCMA during March 2-7, 2006. The base case run was compared with a special case run using GEOS-Chem derived BCON. The GEOS-Chem case generally performs better than the base case in predicting most of the gaseous and particulate pollutants which is due to GEOS-Chem incorporating more regional sources of emissions than the CMAQ base case. SOA precursor levels were lower for the GEOS-Chem case due to the BCON having no set concentration for some of the precursor species. Overall, the GEOS-Chem BCON is very effective and should be utilized more frequently in future studies. Particle trajectory analysis in HYSPLIT shows the importance of the POP and TUL sources and how their emissions can have a significant impact on the MCMA air quality.

REFERENCES

Aiken, A., Salcedo, D., Cubison, M.J., Huffman, J., DeCarlo, P., Ulbrich, I.M., Docherty, K.S., Sueper, D.T., Kimmel, J., Worsnop, D.R., Trimborn, A., Northway, M., Stone, E.A., Schauer, J.J., Volkamer, R.M., Fortner, E., de Foy, B., Wang, J., Laskin, A., Shutthanandan, V., Zheng, J., Zhang, R., Gaffney, J.S., Marley, N.A., Paredes-Miranda, G.L., Arnott, W.P., Molina, L.T., Sosa, G., Jimenez, J.L., 2009. Mexico City aerosol analysis during MILAGRO using high resolution aerosol mass spectrometry at the urban supersite (T0) - Part 1: Fine particle composition and organic source apportionment. Atmos Chem Phys 9, 6633-6653.

Ali, S., Chen, G., Zhang, H., Ying, Q., Cureño, I.V., Marín, A., Bravo, A.H., Sosa, R., 2010. High resolution air quality modeling for the Mexico City Metropolitan Zone using a source-oriented CMAQ model – Part I: Emission inventory and base case model results, 9th Annual CMAS Conference, Chapel Hill, NC.

Bey, I., Jacob, D.J., Yantosca, R.M., Logan, J.A., Field, B.D., Fiore, A.M., Li, Q.B., Liu, H.G.Y., Mickley, L.J., Schultz, M.G., 2001. Global modeling of tropospheric chemistry with assimilated meteorology: Model description and evaluation. J Geophys Res-Atmos 106, 23073-23095.

Bossert, J.E., 1997. An investigation of flow regimes affecting the Mexico City region. Journal of Applied Meteorology 36, 119-140.

Bravo, A.H., Sosa, E.R., Sanchez, A.P., Jaimes, P.M., Saavedra, R.M.I., 2002. Impact of wildfires on the air quality of Mexico City, 1992-1999. Environmental Pollution 117, 243-253.

Byun, D., Schere, K.L., 2006. Review of the governing equations, computational algorithms, and other components of the models-3 Community Multiscale Air Quality (CMAQ) modeling system. Appl. Mech. Rev. 59, 51-77.

Byun, D.W., Ching, J.K.S., eds., 1999. Science Algorithms of the EPA Models-3 Community Multiscale Air Quality (CMAQ) Modeling System. National Exposure Research Laboratory, US EPA, Research Triangle Park, NC.

Chow, J.C., Watson, J.G., Edgerton, S.A., Vega, E., 2002. Chemical composition of PM2.5 and PM10 in Mexico City during winter 1997. Science of the Total Environment 287, 177-201.

Cooke, W.F., Liousse, C., Cachier, H., Feichter, J., 1999. Construction of a 1 degrees x 1 degrees fossil fuel emission data set for carbonaceous aerosol and

implementation and radiative impact in the ECHAM4 model. J Geophys Res-Atmos 104, 22137-22162.

de Foy, B., Fast, J.D., Paech, S.J., Phillips, D., Walters, J.T., Coulter, R.L., Martin, T.J., Pekour, M.S., Shaw, W.J., Kastendeuch, P.P., Marley, N.A., Retama, A., Molina, L.T., 2008. Basin-scale wind transport during the MILAGRO field campaign and comparison to climatology using cluster analysis. Atmos Chem Phys 8, 1209-1224.

de Foy, B., Lei, W., Zavala, M., Volkamer, R., Samuelsson, J., Mellqvist, J., Galle, B., Martinez, A.P., Grutter, M., Retama, A., Molina, L.T., 2007. Modelling constraints on the emission inventory and on vertical dispersion for CO and SO2 in the Mexico City Metropolitan Area using Solar FTIR and zenith sky UV spectroscopy. Atmos Chem Phys 7, 781-801.

Doran, J.C., Abbott, S., Archuleta, J., Bian, X., Chow, J., Coulter, R.L., de Wekker, S.F.J., Edgerton, S., Elliott, S., Fernandez, A., Fast, J.D., Hubbe, J.M., King, C., Langley, D., Leach, J., Lee, J.T., Martin, T.J., Martinez, D., Martinez, J.L., Mercado, G., Mora, V., Mulhearn, M., Pena, J.L., Petty, R., Porch, W., Russell, C., Salas, R., Shannon, J.D., Shaw, W.J., Sosa, G., Tellier, L., Templeman, B., Watson, J.G., White, R., Whiteman, C.D., Wolfe, D., 1998. The IMADA-AVER boundary layer experiment in the Mexico City area. Bulletin of the American Meteorological Society 79, 2497-2508.

Draxler, R.R., Hess, G.D., 1997. Description of the HYSPLIT_4 modeling system. NOAA Air Resources Laboratory, Silver Spring, MD.

Draxler, R.R., Hess, G.D., 1998. An overview of the HYSPLIT_4 modelling system for trajectories, dispersion and deposition. Australian Meteorological Magazine 47, 295-308.

Duncan Fairlie, T., Jacob, D.J., Park, R.J., 2007. The impact of transpacific transport of mineral dust in the United States. Atmos Environ 41, 1251-1266.

Dzepina, K., Volkamer, R.M., Madronich, S., Tulet, P., Ulbrich, I.M., Zhang, Q., Cappa, C.D., Ziemann, P.J., Jimenez, J.L., 2009. Evaluation of recently-proposed secondary organic aerosol models for a case study in Mexico City. Atmos Chem Phys 9, 5681-5709.

Edgerton, S.A., Bian, X., Doran, J.C., Fast, J.D., Hubbe, J.M., Malone, E.L., Shaw, W.J., Whiteman, C.D., Zhong, S., Arriaga, J.L., Ortiz, E., Ruiz, M., Sosa, G., Vega, E., Limon, T., Guzman, F., Archuleta, J., Bossert, J.E., Elliot, S.M., Lee, J.T., McNair, L.A., Chow, J.C., Watson, J.G., Coulter, R.L., Doskey, P.V., Gaffney, J.S., Marley, N.A., Neff, W., Petty, R., 1999. Particulate air pollution in Mexico City: A collaborative research project. J Air Waste Manage 49, 1221-1229.

Fast, J.D., Zhong, S.Y., 1998. Meteorological factors associated with inhomogeneous ozone concentrations within the Mexico City basin. J Geophys Res-Atmos 103, 18927-18946.

Jaimes, L., Sandoval, J., 2002. Propane and butane emission sources to ambient air of Mexico City metropolitan area. Science of the Total Environment 289, 243-247.

Jazcilevich, A.D., Garcia, A.R., Ruiz-Suarez, L.G., 2003. A study of air flow patterns affecting pollutant concentrations in the Central Region of Mexico. Atmos Environ 37, 183-193.

Lei, W., Zavala, M., de Foy, B., Volkamer, R., Molina, L.T., 2008. Characterizing ozone production and response under different meteorological conditions in Mexico City. Atmos Chem Phys 8, 7571-7581.

Mena-Carrasco, M., Carmichael, G.R., Campbell, J.E., Zimmerman, D., Tang, Y., Adhikary, B., D'Allura, A., Molina, L.T., Zavala, M., Garcia, A., Flocke, F., Campos, T., Weinheimer, A.J., Shetter, R., Apel, E., Montzka, D.D., Knapp, D.J., Zheng, W., 2009. Assessing the regional impacts of Mexico City emissions on air quality and chemistry. Atmos Chem Phys 9, 3731-3743.

Molina, L.T., Kolb, C.E., de Foy, B., Lamb, B.K., Brune, W.H., Jimenez, J.L., Ramos-Villegas, R., Sarmiento, J., Paramo-Figueroa, V.H., Cardenas, B., Gutierrez-Avedoy, V., Molina, M.J., 2007. Air quality in North America's most populous city - overview of the MCMA-2003 campaign. Atmos Chem Phys 7, 2447-2473.

Molina, L.T., Madronich, S., Gaffney, J.S., Apel, E., de Foy, B., Fast, J., Ferrare, R., Herndon, S., Jimenez, J.L., Lamb, B., Osornio-Vargas, A.R., Russell, P., Schauer, J.J., Stevens, P.S., Volkamer, R., Zavala, M., 2010. An overview of the MILAGRO 2006 campaign: Mexico City emissions and their transport and transformation. Atmos. Chem. Phys. 10, 8697-8760.

Molina, L.T., Molina, M.J., 2002. Air Quality in the Mexico Megacity: An Integrated Assessment. Kluwer Academic Publishers, Norwell, MA.

Molina, M.J., Molina, L.T., 2004. Megacities and atmospheric pollution. J Air Waste Manage 54, 644-680.

Mugica, V., Ortiz, E., Molina, L., De Vizcaya-Ruiz, A., Nebot, A., Quintana, R., Aguilar, J., Alcantara, E., 2009. PM composition and source reconciliation in Mexico City. Atmos Environ 43, 5068-5074.

Song, J., Lei, W., Bei, N., Zavala, M., de Foy, B., Volkamer, R., Cardenas, B., Zheng, J., Zhang, R., Molina, L.T., 2010. Ozone response to emission changes: a modeling

study during the MCMA-2006/MILAGRO campaign. Atmos Chem Phys 10, 3827-3846.

Sosa, E.R., Bravo, A.H., Mugica, A.V., Sanchez, A.P., Bueno, L.E., Krupa, S., 2009. Levels and source apportionment of volatile organic compounds in southwestern area of Mexico City. Environmental Pollution 157, 1038-1044.

Stephens, S., Madronich, S., Wu, F., Olson, J.B., Ramos, R., Retama, A., Munoz, R., 2008. Weekly patterns of Mexico City's surface concentrations of CO, NOx, PM10 and O-3 during 1986-2007. Atmos Chem Phys 8, 5313-5325.

Stone, E.A., Hedman, C.J., Zhou, J.B., Mieritz, M., Schauer, J.J., 2010. Insights into the nature of secondary organic aerosol in Mexico City during the MILAGRO experiment 2006. Atmos Environ 44, 312-319.

Stone, E.A., Snyder, D.C., Sheesley, R.J., Sullivan, A.P., Weber, R.J., Schauer, J.J., 2008. Source apportionment of fine organic aerosol in Mexico City during the MILAGRO experiment 2006. Atmos Chem Phys 8, 1249-1259.

Vega, E., Eidels, S., Ruiz, H., Lopez-Veneroni, D., Sosa, G., Gonzalez, E., Gasca, J., Mora, V., Reyes, E., Sanchez-Reyna, G., Villasenor, R., Chow, J.C., Watson, J.G., Edgerton, S.A., 2010. Particulate air pollution in Mexico City: a detailed view. Aerosol Air Qual. Res. 10, 193-211.

Vega, E., Mugica, V., Reyes, E., Sanchez, G., Chow, J.C., Watson, J.G., 2001. Chemical composition of fugitive dust emitters in Mexico City. Atmos Environ 35, 4033-4039.

Vega, E., Reyes, E., Sanchez, G., Ortiz, E., Ruiz, M., Chow, J., Watson, J., Edgerton, S., 2002. Basic statistics of PM2.5 and PM10 in the atmosphere of Mexico City. Science of the Total Environment 287, 167-176.

Villasenor, R., Lopez-Villegas, M.T., Eidels-Dubovoi, S., Quintanar, A., Gallardo, J.C., 2003. A mesoscale modeling study of wind blown dust on the Mexico City Basin. Atmos Environ 37, 2451-2462.

Ying, Q., Fraser, M.P., Griffin, R.J., Chen, J., Kleeman, M.J., 2007. Verification of a source-oriented externally mixed air quality model during a severe photochemical smog episode. Atmos Environ 41, 1521-1538.

Zhang, Y., Dubey, M.K., Olsen, S.C., Zheng, J., Zhang, R., 2009. Comparisons of WRF/Chem simulations in Mexico City with ground-based RAMA measurements during the 2006-MILAGRO. Atmos Chem Phys 9, 3777-3798.

APPENDIX A

CODE FOR READING A GEOS-CHEM OUTPUT FILE

```
      program readbpf

! code to read the binary punch format of the GEOS-Chem file

      character*80 toptitle   ! title line
      character*40 ftype      ! file identifier string

      character*20 modelname              ! name of the model
      real*4 modelres_lat, modelres_lon   ! model resolution
      integer*4 halfpolar     ! half-sized boxes at poles [1/0]
      integer*4 center180     ! first lon centered on 180 [1/0]

      character*40 category         ! diagnostic category name
      integer*4 tracer              ! tracer number
      character*40 unit_string      ! unit of tracer
      real*8 tau0, tau1        ! time in hours since 00:00 GMT 1/1/1985
      character*40 reserved         ! extra
      integer*4 dim_ni, dim_nj, dim_nl    ! dimensions of data block
      integer*4 dim_io, dim_jo, dim_lo    ! starting box
      integer*4 skip                ! length of data block in bytes

      real*4, allocatable :: array(:,:,:)       ! data block
      integer i, j, l

      character*256 sfile     ! input geos chem file

      read (*,'(a)') sfile
      open (unit = 1, file = sfile, form = 'unformatted',
     +      access = 'sequential', status = 'unknown')
! read the general header
      read (1) ftype
      read (1) toptitle

! begin reading data block one at a time
      do
! first line of data block header
         read (1,iostat = ierr) modelname, modelres_lat, modelres_lon,
     +      halfpolar, center180
         if (ierr /= 0) then
            print *, 'iostat=', ierr, 'in title header'
            goto 1
         endif
! second line of data block header
         read (1,iostat = ierr) category, tracer, unit_string,
     +      tau0, tau1, reserved,
```

```
     +       dim_ni, dim_nj, dim_nl, dim_io, dim_jo, dim_lo, skip
             if (ierr /= 0) then
                print *, 'iostat=', ierr, 'in data block header'
                goto 1
             endif
             allocate (array(dim_ni,dim_nj,dim_nl))

! read data block
             read (1,iostat = ierr)(((array(i,j,l),i=1,dim_ni),j=1,dim_nj),
     +       l=1,dim_nl)
             if (ierr /= 0) then
                print *, 'iostat=', ierr, 'in data block'
                goto 1
             endif

             deallocate(array)

          enddo

1         close (1)

          end
```

APPENDIX B

CHEMICAL MAPPING IN GEOS2CMAQ USING THE SAPRC-99 SCHEME AND A COMPARISON OF VERTICAL LAYERS IN GEOS-CHEM AND CMAQ

Table 11 List of species mapped from GEOS-Chem to CMAQ.

CMAQ SAPRC-99 SPECIES	GEOS-CHEM SPECIES
[NO2]	[NOx]
[O3]	[Ox] – [NOx]
[PAN]	[PAN]
[CO]	[CO]
[ALK3] = [ALK4] = [ALK5]	0.083 [ALK4]
[ISOPRENE]	0.200 [ISOP]
[HNO3]	[HNO3]
[HO2H]	[H2O2]
[ACET]	0.333 [ACET]
[MEK]	0.250 [MEK]
[CCHO]	0.500 [ALD2]
[RCHO]	[RCHO]
[MVK]	[MVK]
[METHACRO]	[MACR]
[MA_PAN]	[PMN]
[PAN2]	[PPN]
[RNO3]	[R4N2]
[OLE1]	0.333 [PRPE]
[ALK2]	0.333 [C3H8]
[HCHO]	[CH2O]
[ALK1]	0.500 [C2H6]
[N2O5]	[N2O5]
[HNO4]	[HNO4]
[COOH]	[MP]
[SO2]	[SO2]
[NH3]	[NH3]
[ASO4J]	[SO4] + [MSA]
[ANO3J]	[NIT]
[ANH4J]	[NH4]
[AORGPAJ]	0.055 [OCPI] + 0.055 [OCPO]
[AECJ]	[BCPI] + [BCPO]
[A25J]	0.145 [DST1] + 0.145 [DST2]
[ANAJ] = [ACLJ]	1.030 [SALA]
[ANAK] = [ACLK]	1.030 [SALC]
[ASOIL]	0.290 [DST3] + 0.290 [DST4]

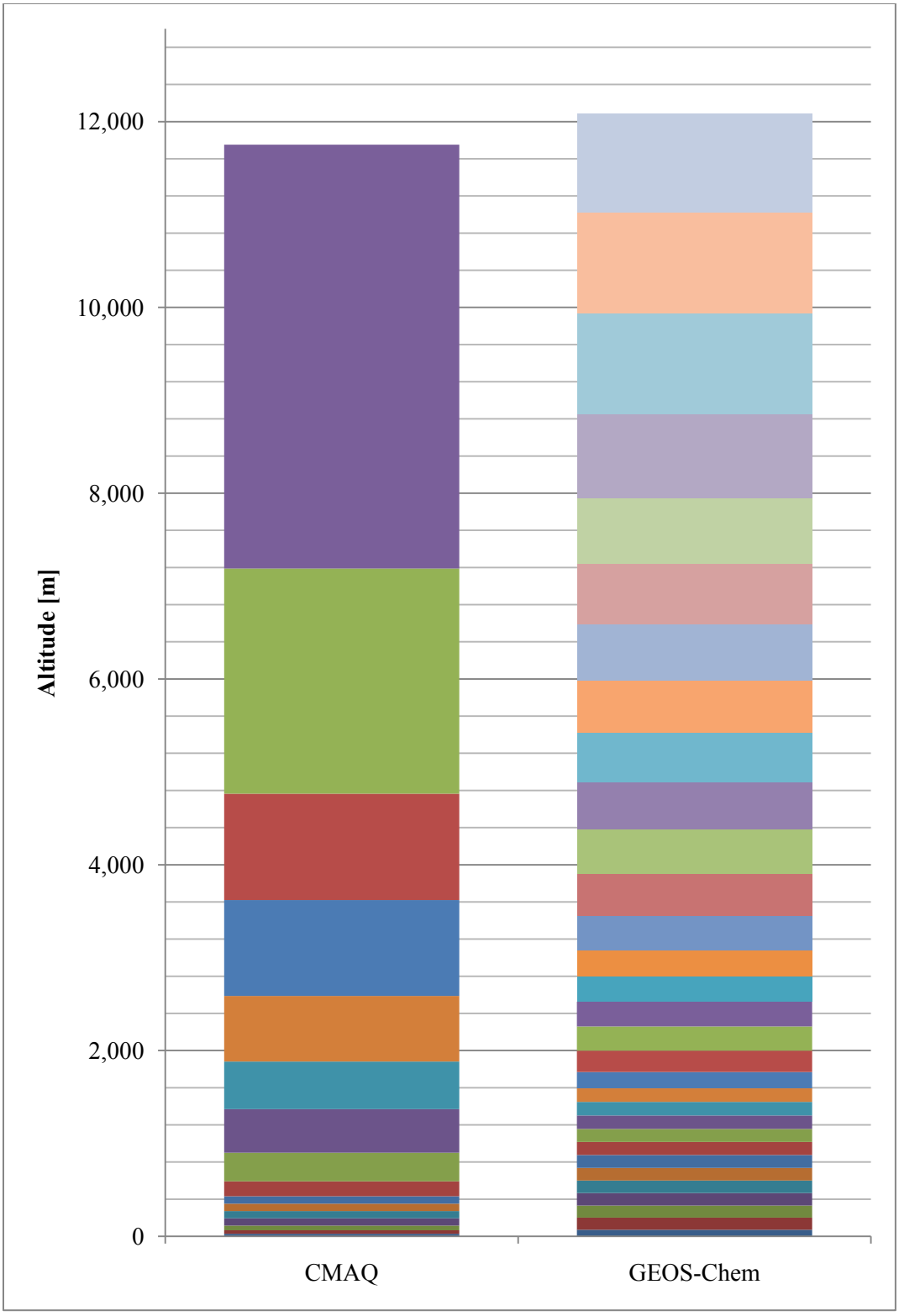

Figure 51 Comparison of vertical layers in GEOS-Chem and CMAQ

APPENDIX C

LIST OF MONITORING STATIONS IN THE MCMA

Table 12 Location of the monitoring stations saving species concentrations.

STN	LAT	LON	LAMBERT		CMAQ DOMAIN	
			x	y	COL	ROW
ARA	19.47	-99.07	4654.9	-58295.6	91	96
ATI	19.58	-99.25	-14100.7	-46710.6	71	108
CAM	19.47	-99.17	-5271.9	-58725.4	80	95
CES	19.34	-99.07	4638.1	-73239.2	91	80
CHA	19.46	-98.90	22490.6	-59241.2	110	95
COY	19.35	-99.16	-3935.7	-71739.3	82	81
CUA	19.36	-99.29	-18054.8	-70054.1	67	83
EAC	19.48	-99.24	-12990.3	-57133.4	72	97
HAN	19.42	-99.08	3704.0	-63776.9	90	90
LAG	19.44	-99.14	-1694.5	-61362.0	84	92
LLA	19.58	-99.04	8331.4	-46515.9	95	108
LPR	19.53	-99.12	167.5	-51381.4	86	103
LVI	19.47	-99.12	126.1	-58549.7	86	95
MER	19.42	-99.12	-31.1	-63479.5	86	90
MIN	19.42	-99.16	-4593.3	-63677.4	81	90
PED	19.32	-99.20	-8867.1	-74472.7	76	78
PER	19.38	-98.99	13302.5	-67929.8	100	85
PLA	19.37	-99.20	-8488.7	-69807.7	77	83
SAG	19.53	-99.03	9316.6	-51577.3	96	103
SJA	19.45	-99.09	3473.5	-60446.3	89	93
SUR	19.31	-99.15	-3213.7	-75687.8	82	77
TAC	19.46	-99.20	-8734.6	-60091.7	76	94
TAH	19.25	-99.01	11396.9	-83183.7	98	69
TAX	19.34	-99.12	-439.3	-73140.5	85	80
TLA	19.53	-99.20	-8960.2	-51952.5	76	102
TLI	19.60	-99.18	-6040.9	-43892.1	79	111
TPN	19.26	-99.18	-6797.3	-82017.1	79	70
UIZ	19.36	-99.07	5003.9	-70316.4	91	83
VAL	19.52	-99.17	-4883.1	-52538.7	81	102
VIF	19.66	-99.10	2372.2	-37750.2	88	118
XAL	19.53	-99.08	4454.6	-52086.5	91	102

Table 13 List of monitoring stations and species monitored.

STN	O_3	NO_x	CO	SO_2	PM_{10}	$PM_{2.5}$
ARA			x	x		
ATI		x	x	x		
CAM						x
CES	x	x	x	x	x	
CHA	x		x			
COY	x					x
CUA	x					
EAC	x	x	x	x	x	
HAN	x	x	x	x	x	
LAG	x	x	x	x		
LLA				x		
LPR				x		
LVI				x	x	
MER	x	x	x	x	x	x
MIN			x			
PED	x	x	x	x	x	
PER						x
PLA	x	x	x	x	x	
SAG	x	x	x	x	x	x
SJA						x
SUR	x	x	x	x	x	
TAC	x	x	x	x		
TAH	x	x	x	x	x	
TAX	x	x	x	x	x	
TLA	x	x	x	x	x	x
TLI		x	x	x	x	
TPN	x					
UIZ	x	x	x	x		x
VAL			x	x		
VIF		x	x	x	x	
XAL	x	x	x	x	x	

Table 14 Location of the monitoring stations saving meteorological data.

STN	LAT	LON	LAMBERT		CMAQ DOMAIN	
			x	y	COL	ROW
ENP1	19.27	-99.12	-177.4	-80275.9	85	63
ENP2	19.38	-99.10	2040.9	-67912.9	87	75
ENP5	19.31	-99.13	-1528.2	-76415.8	83	67
ENP6	19.35	-99.19	-7055.1	-71396.5	78	72
ENP7	19.41	-99.13	-815.9	-64604.4	84	79
ENP8	19.37	-99.20	-7975.2	-69852.1	77	73
ENP9	19.48	-99.13	-1003.8	-56928.5	84	86
CCHA	19.50	-99.20	-8983.4	-55150.6	76	88
CCHV	19.48	-99.14	-2331.7	-56829.3	83	86
CCHN	19.47	-99.24	-13042.8	-57927.2	72	85
CCHO	19.38	-99.06	6321.5	-67933.8	91	75
CCHS	19.31	-99.20	-8428.5	-75851.4	77	67
AIPT	19.43	-99.13	-1150.3	-62861.8	84	80

VITA

Name: Sajjad Ghulam Ali

Address: Zachry Department of Civil Engineering
c/o Dr. Qi Ying
Texas A&M University
College Station, TX 77843-3136

Education: B.S., Civil Engineering, Texas A&M University, 2008
M.S., Civil Engineering, Texas A&M University, 2010